On gravity-driven flow

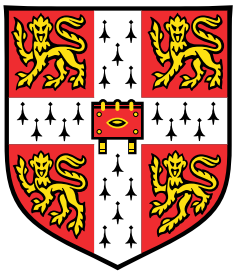

Marcus C. Horsley

Department of Earth Science

University of Cambridge

This dissertation is submitted for the degree of

Doctor of Philosophy

Wolfson College

July 2018

Given enough time, these are some of the things that hydrogen atoms do.

Declaration

I hereby declare that except where specific reference is made to the work of others, the contents of this dissertation are original and have not been submitted in whole or in part for consideration for any other degree or qualification in this, or any other university. This dissertation is my own work and contains nothing which is the outcome of work done in collaboration with others, except as specified in the text and Acknowledgements. In particular, although Professor Colm-cille P. Caulfield is registered as my principal supervisor, my research has been exclusively supervised by Professor Andrew W. Woods. This dissertation contains fewer than 275 numbered pages of which not more than 225 pages are text, appendices, illustrations and bibliography.

Marcus C. Horsley

July 2018

Acknowledgements

Now I come to write this part, it's harder than I thought.

To list the number of people who have made this possible would take me longer than the four years I have given to write it. However, I will try and name at least a few. If your name is not here and you expected it to be, I am sorry, but I am sure your contribution was appreciated in the moment.

First and foremost, I would like to thank Professor Andrew W. Woods for everything. If it were not for his ferocious intelligence, his enthusiasm, and his passion, none of this would have come to be. He has imparted to me a lifetime's worth of wisdom, but in particular the philosophy of problem solving and the art of the understatement.

It would also be unjust for me not to acknowledge Professor Colm-cille P. Caulfield for being instrumental in my decision to embark on this journey. I have greatly enjoyed all of our discussions, from fundamental science to the wider world at large. Thank you.

This brings me to all of my colleagues at the BP Institute. You have all been fantastic in making this a once-in-a-lifetime experience. I must give particular thanks to Dr Chris N. Richardson, not just for his invaluable knowledge of computing, which has helped so deeply, but also for his insights into the nuances of language, which has kept me thoroughly entertained throughout the years. I must also give a special mention to doctors Richard Alloway, Tim Beeson-Jones, Peter Dudfield, Stefano Rocco,

and Chris Truscott. You have made coming to work enjoyable, going to the pub even more so, and I will miss our office dearly.

Of course I must give a special thank you to my family. One to Mum, Dad, Megan, Nan and Grandad, for being there and supporting me, and one to Kevin for being my best friend.

For the rest, I leave you a quote from one of my favourites. "For those I have loved, or who have been so lenient and gracious as to have loved me, I have not words enough here, and I remember with gratitude how they have made me speechless in return."

Abstract

This thesis investigates three areas of scientific interest under the umbrella of gravity-driven flow. In the first problem we analyse the effect of curved boundaries on the evolution of finite-release low-Reynolds-number exchange flow. From the equations of motion in an annular geometry we derive the governing nonlinear PDE for the evolution of the density interface. Systematically varying the initial conditions leads to the recognition that there are different routes to equilibrium. Asymptotic analysis of squeezing and draining limits allows us to find analytical solutions with good agreement to the numerical solutions. Finally, we show the time taken to reach equilibrium can vary by two orders of magnitude. We relate these time scales to the application of displacing drilling lubricant by cement in a horizontal oil well.

In the second problem we develop a simplified theory relating the downstream structure of horizontally propagating turbulent gravity currents to uniform source conditions. We constrain the downstream solutions by conserving the flux of horizontal buoyancy and momentum. With an experimentally motivated ansatz that the downstream horizontal velocity and buoyancy structure is either i) entirely linearly stratified ii) consists of a well-mixed uniform lower region overlain by a linearly stratified region, we can relate the upstream conditions to the downstream conditions as a function of source Froude number, downstream gradient Richardson number, and a shape factor ϕ. These solutions lead to global constraints on the entrainment flux and energy dissipation of transitioning currents.

In the third problem, we present a series of new numerical simulations on two-dimensional gravity currents propagating down a rigid inclined boundary. From the data generated by the simulations we can estimate the rate of entrainment E of these currents, and present this data over a range of angles θ. Furthermore, we show that around 10% of the buoyancy, and 15% of the momentum flux, is transported by turbulent fluctuations. We also show that the Richardson number Ri of these currents remains marginally stable $Ri \approx 0.25$ and is independent of angle. Finally we show that the coefficient of drag c_d experienced by these currents is constant and approximately $c_d \approx 0.01$.

Publications

This thesis contains two chapters which have been published in peer-reviewed journals prior to the thesis submission date. The papers are as follows:

- Chapter Two - Horsley, Marcus C., and Andrew W. Woods. "Gravity-driven flow in a horizontal annulus." *Journal of Fluid Mechanics* 830 (2017): 479-493.
- Chapter Three - Horsley, Marcus C., and Andrew W. Woods. "A note on analytic solutions for entraining stratified gravity currents." *Journal of Fluid Mechanics* 836 (2018): 260-276.

This thesis also contains one study under review:

- Chapter Four - Horsley, Marcus C., and Andrew W. Woods. "Entrainment in two-dimensional inclined gravity currents." *Journal of Fluid Mechanics*.

Table of contents

List of figures

Chapter 1

Introduction

This thesis considers a number of problems relating to gravity-driven flow. Section 1.1 outlines the nature of gravity currents and gives an overview of the field. In §1.2 we discuss previous work in the low-Reynolds-number limit and outline the content of **Chapter Two** of this thesis, which focuses on a novel problem related to thin films under gravitational adjustment. In §1.3 we examine the corpus of literature in the high-Reynolds-number limit, and motivate **Chapters Three** and **Four** of this thesis. These chapters analyse turbulent entrainment in horizontal and inclined currents, presenting both new numerical simulations and simplified theory to obtain constraints on the mixing and entrainment rate.

1.1 Motivation

Gravity-driven flow, alternatively called a gravity current, a density current, or a buoyancy current, is the flow of one fluid within another, primarily horizontally, due to a density difference between them (Simpson, 1982). If the flow were predominantly vertical it would be referred to as a plume and follow different dynamical principles (Turner,

1979). Gravity-driven flows are ubiquitous in nature and industry, so understanding the dynamics and flow properties has many wide-ranging applications.

Before we begin to give further detail on gravity currents, it is important to introduce a dimensionless property of fluid flow known as the Reynolds number. The Reynolds number is the ratio of the inertial forces to viscous forces inside a fluid, and is usually written

$$Re = \frac{\text{inertial forces}}{\text{viscous forces}} = \frac{UL}{\nu}, \tag{1.1}$$

where U, L are the characteristic velocity and length scales of the flow, and ν the kinematic viscosity. The Reynolds number can be used to categorise and correlate different fluid flow regimes. At low-Reynolds-number ($Re \lessapprox 1$), viscous forces dominate and the flow is characterised by smooth constant fluid motion, sometimes called a creeping or laminar flow. By contrast, at large Reynolds numbers ($Re \gtrapprox 3000$), the inertial forces dominate and the flow can be characterised by chaotic turbulent motions of eddies, vortices, and fluid instabilities. A regime exists between the two limits and is known as transitional flow, which is of interest to many fields; however it is not studied in this thesis.

A classic example of a gravity current in the low-Reynolds-number viscous limit would be honey flowing over a table, as shown in figure 1.1*a*. We note that the flow is characterised by smooth motion. Other occurrences of such flows are oil flowing through a thin pipe, the motion of hot glass being blown over a sheet, and the flow of viscous magma in the Earth's crust.

In the high-Reynolds-number inertial limit, examples are also wide-ranging. In figure 1.1*b* we show an example of a high-Reynolds-number density current propagating through New York City on September 11th 2001. In this case the buoyancy force is derived from the presence of fine suspended particulate matter. As well as dusty flows, particle laden density currents often develop during explosive volcanic eruptions and

a)  b) 

Fig. 1.1 (*a*) Honey flowing over a smooth table is an example of a low-Reynolds-number gravity-driven flow. Image from www.shutterstock.com (*b*) An example of a high-Reynolds-number pyroclastic density current flowing over complex topography of New York City on September 11th 2001. Photo by Det. Greg Semendinger. From Reuters/NYPD via ABC News.

the resulting flows are called pyroclastic flows. We note that the motion of the fluid is chaotic with a visible local turbulent structures. Other examples are the migration of smoke underneath a roof during a fire, the intrusion of fresh water into salt water at an estuary, and the flow of gas released after an industrial accident.

Given the numerous cases in which these types of flow can arise, understanding their behaviour has been the subject of considerable interest and research. Particularly for high-Reynolds-number currents, it is important to quantify and characterise the mechanism by which they entrain and mix with the ambient fluid in which they intrude. This understanding has an economic impact: for example, predicting the development of a liquefied natural gas spill informs the design of barriers and other safety features for such industrial accidents. Similarly for low-Reynolds-number flows the location and evolution of the free-surface, and its dependency on inflow and boundary conditions, is also of significant interest and use, for example with lava flows advancing towards habitations as sometimes occurs at Mount Etna and has recently occurred in Hawaii.

1.2 Low-Reynolds-number flow

The research into creeping flows is deep and extensive, with analysis into the effects of flow rheology (Balmforth et al., 2001; Hogg and Matson, 2009; Longo et al., 2016), how flow develops within porous media (Huppert and Woods, 1995; Lyle et al., 2005; Vella and Huppert, 2006), and the consequences of draining boundaries (Acton et al., 2001; Pritchard et al., 2001; Spannuth et al., 2009) to give a non-exhaustive list. The canonical example of a low-Reynolds-number gravity current concerns the propagation of a relatively dense fluid over a rigid horizontal boundary into a deep ambient environment (such as shown in figure 1.1). Huppert (1982b) gives the authoritative treatment of this situation. Using a lubrication-theory approximation, that - after some transition from initial conditions - the depth of the flow is much smaller than its lateral extent, a simplification of the governing Navier-Stokes equations can be made. This approximation gives a force balance between viscous forces and pressure gradient, which, along with global conservation of mass, leads to a nonlinear PDE governing the spatio-temporal evolution of the free-surface. In some cases similarity solutions for the governing PDE can be found, and in others it is solved numerically, to give good agreement between the theory and experimental data. Solutions are obtained for both the finite release and continuous flux cases. Huppert (1982a) and Lister (1992) extend this work by considering the rigid boundary to be a fixed inclined plane, such that there is a component of gravity in the direction of the flow which alters the dynamics. Analysing the idealised problem and using the lubrication assumptions, Lister (1992) finds new similarity solutions for the creeping flow. He notes that at late times in experiments a capillary instability begins to form, which demonstrates some of the limitations of neglecting the surface tension.

A problem related to the low-Reynolds-number gravity current is that of a viscous exchange flow. A viscous exchange flow occurs when fluids of different densities

counterflow along a horizontal channel. Understanding exchange flows also has practical application in geophysical and industrial settings, such as modelling the displacement of miscible fluids in pipes. Matson and Hogg (2012) analyse a viscous exchange flow within a horizontal channel. They find similarity solutions that depend on the ratio of viscosities between the exchanging fluids, and utilise asymptotic techniques to determine the shape of the miscible interface.

Motivated by the practical application of understanding miscible exchange flow, in §2 we introduce a novel problem in this field. The flow described and studied in §2 is an idealised two-dimensional model for the problem of displacing drilling lubricant with cement inside a horizontal oil well. §2 takes ideas from the aforementioned papers and extends the analysis of a finite-release exchange flow inside a two-dimensional annulus which lies in a vertical plane. The analysis of creeping flow inside a domain with curved boundaries extends the understanding of exchange flow, and also leads to the recognition of different flow regimes which depend on the initial conditions. Utilising numerical and asymptotic techniques these different flow regimes are studied. Different initial conditions can drastically alter the time taken for the cement to reach an equilibrium state, which has consequences for oil well integrity.

1.3 High-Reynolds-number flow

An extensive body of research on high-Reynolds-number gravity currents has also developed in recent history. Early work on gravity currents usually focused on the high-Reynolds-number inertial limit due to the ready availability of environmental examples such as turbidity currents (Kuenen, 1950) or the advancement of cold fronts (Clarke, 1961). An important concept in high-Reynolds-number flows is a dimensionless

quantity called the Froude number

$$Fr = \frac{u}{\sqrt{g'h}}, \tag{1.2}$$

where u is the fluid velocity, h the layer depth, and $g' = g(\rho - \rho_0)/\rho_0$ is the acceleration due to gravity. The Froude number is analogous to the Mach number in that it is the ratio of the fluid velocity to the local speed of waves (ie. sound). For $Fr < 1$ we have subcritical (or slow/tranquil) flow with small surface water waves able to move upstream. For $Fr > 1$ the flow is supercritical and so surface water waves can only move downstream. The Froude number Fr is used in conjunction with the Reynolds number Re to delineate the boundary between laminar and turbulent flow.

Early work by von Kármán (1940), at the behest of the military who wished to understand the motion of toxic gas and how not to poison their own troops, attempted to use Bernoulli's theorem to argue that $Fr = \sqrt{2}$ for a turbulent gravity current in an infinitely deep ambient fluid. Further pioneering work by Benjamin (1968) argued that von Kármán had misapplied Bernoulli's theorem, by taking a contour through a turbulent region, and presented an alternative conservation of momentum flux argument to reach the same conclusion for infinite depth flows (namely that $Fr = \sqrt{2}$). Given both authors were solving integrated versions of the Euler equations, we can see how they must necessarily reach the same result. Benjamin (1968) also considered a finite depth channel, and used a conservation of energy flux argument to show that energy conserving currents occupy one-half the depth of the channel. Gardner and Crow (1970) corroborate this theory with experimental work.

Whilst the shallow water model developed by Benjamin (1968) is useful, a key assumption made is that there is no mixing between the ambient fluid and the gravity current. This no-mixing (ie. constant volume flux) assumption has been used in many modelling methodologies, such as box models (Huppert and Simpson, 1980) and

other shallow water theories (Bonnecaze et al., 1993; Hoult, 1972), with some success. However, it was suggested by Prandtl (1953) that there is mixing between gravity current and the ambient fluid. This has been corroborated by many experiments since (Hacker et al., 1996; Hallworth et al., 1993; Sher and Woods, 2015). As the dynamics of gravity currents are governed by density differences, any mixing and entrainment of the ambient into the current significantly alters its density and increases the volume flux. It is then clear that entrainment will have an effect on the overall dynamics of such flows, and hence developing our understanding of the mechanism is important.

For a two-dimensional current, the notion of an entrainment coefficient was first introduced by Morton et al. (1956) within the context of plumes. This idea is easily ported over to gravity currents advancing along sloped boundaries, with the rate at which fluid is entrained from the ambient E assumed to be proportional to a characteristic velocity scale u such that

$$\frac{dQ}{dx} = Eu, \tag{1.3}$$

where Q is the volume flux and x is an along-current co-ordinate. An early paper by Ellison and Turner (1959) presents a series of experiments on continuous flux gravity currents on inclined boundaries with the aim of measuring the entrainment as a function of the inclination angle. There have been further field work, experimental, and numerical studies since Ellison and Turner (1959) to quantify the entrainment across the upper surface of gravity currents in horizontal and inclined settings (Britter and Simpson, 1978; Johnson and Hogg, 2013; Princevac et al., 2005).

Another important dimensionless quantity to introduce is the Richardson number. The Richardson number can be interpreted as the ratio of the kinetic to potential

energy in the flow, or equivalently as the buoyancy term to the flow shear term

$$Ri = \frac{\text{potential energy}}{\text{kinetic energy}} = \frac{\text{buoyancy term}}{\text{flow shear term}} = \frac{g'h}{u^2}. \tag{1.4}$$

The Richardson number is another tool to help us characterise flow behaviour. If the Richardson number is large $Ri > 1$ the buoyancy forces are dominant and there is insufficient kinetic energy to mix and homogenise the fluid. In this case the fluid is said to be stable. Conversely, if the Richardson number is small the buoyancy is unimportant and the fluid can be easily overturned and mixed - the flow is said to be unstable. There has been much researching into determining, and understanding, the critical Richardson number which demarcates the boundary between these stable and unstable cases. The canonical theorem of Howard (1961) and Miles (1961) shows that steady unidirectional shear flows $u(z)$ in an inviscid stably stratified fluid, bounded between two horizontal walls at z_1, z_2 and either i) extending infinitely in the horiztonal x direction or ii) having periodic disturbances in x, are linearly stable to all perturbations if the local Richardson number $R > 1/4$, where in this case the local Richardson number takes an alternative (but equivalent) definition $R = N(z)^2/u_z^2$, with N the buoyancy frequency and u_z the shear.

It is clear that the Richardson number, the measure of the relationship between the stabilising buoyancy forces and destabilising shear forces, of a given flow will have a role in determining the amount of mixing and the rate at which it occurs. After the early work of Ellison and Turner (1959) several studies have attempted to parametrise the relationship between E and Ri using field and experimental data (Cenedese and Adduce, 2008, 2010; Odier et al., 2014); however, there is still some uncertainty regarding the accuracy and validity of such parametrisations.

Several numerical and experimental studies have found that the velocity and buoyancy profiles of steady-state gravity currents can be accurately approximated by

linear profiles, or by a hybrid piecewise profile that is linear in the upper region and uniform in the lower region (Kneller et al., 2016; Sher and Woods, 2017; van Reeuwijk et al., 2018). Motivated by these experimental data, in §3 we form an ansatz that the downstream velocity and buoyancy profiles are of the simplified form described. Furthermore, we use this ansatz with the conservation of downstream buoyancy and momentum flux to obtain a simplified theory on the entrainment flux of such currents. We find that the entrainment flux is a function of the source Froude number and the downstream gradient Richardson number of the flow profiles. We can obtain estimates and constraints of the mixing based on the downstream Richardson number. Our theory is successfully compared to the numerical data presented by Kneller et al. (2016).

In §4 we present new numerical simulations of two-dimensional continuous flux gravity currents flowing down fixed rigid inclined boundaries at a series of angles θ. We find that after an adjustment period the flow reaches a self-similar state where the velocity and buoyancy profiles are approximately linear consistent with the findings of van Reeuwijk et al. (2018). From the data generated by these simulations we can calculate the entrainment coefficient E for each angle and also the corresponding Richardson number Ri. We find E grows approximately linearly with θ and the Richardson numbers have value $Ri \approx 0.25$ for all angles suggesting the flow is approximately marginally stable and independent of θ. This is consistent with the description by Turner (1979), in which he suggests that the mixing in the flow controls the flow to be marginally state: "While turbulence is present the drag on the layers increases and the velocity falls, but when it is suppressed the flow is accelerated again by gravity". Furthermore, by appropriately time-averaging and utilising a Reynolds decomposition, we can quantify the proportion of the buoyancy and momentum flux which is carried by the mean and turbulent components of the flow. We find turbulent fluctuations correspond to around 10% of the buoyancy flux transport and $\sim$15% of the momentum

flux transport. Finally, by using the conservation of momentum flux and an appropriate parametrisation based on the mean velocity, we can derive estimates for the coefficient of friction c_d experienced by the current.

Chapter 2

Gravity-driven flow in a horizontal annulus

2.1 Abstract

A theory for the low-Reynolds-number gravity-driven flow of two Newtonian fluids separated by a density interface in a two-dimensional annular geometry is developed. Solutions for the governing time-dependent equations of motion, in the limit that the radius of the inner and outer boundaries are similar, and in the case that the interface is initially inclined to the horizontal, are analysed numerically. We focus on the case in which the fluid is arranged symmetrically about a vertical line through the centre of the annulus. These solutions are successfully compared with asymptotic solutions in the regimes that i) a thin film of dense fluid drains down the outer boundary of the annulus, and ii) a thin layer of less dense fluid is squeezed out of the narrow gap between the base of the inner annulus and dense fluid. Application of the results to the problem of mud displacement by cement in a horizontal well is briefly discussed.

2.2 Introduction

Directional drilling, and in particular horizontal drilling, has been an important technique in oil and gas extraction since the early twentieth century. During the drilling process, an annular void between the casing string and the drilled hole is created. This void is initially full of a drilling fluid commonly referred to as mud, which is used to cool the drill bit and lubricate the drilling process. Once drilling has been completed, the annulus is filled with cement, which upon curing, will add stability and integrity to the wellbore (Sauer et al., 1987). The time-dependent interaction of the interface between the cement and mud - during the displacement procedure - is crucial in determining the effectiveness of the mud displacement (Eduardo et al., 2004), and thus the quality of the seal in the well.

Models of the motion of the cement-mud interface typically describe the flow along the well, and often the focus is on the non-uniform gap width, which leads to channelling of the cement along the wider part of the annulus. Typically the annular gap is only 1-3 cm thick, while the radius is 10-15cm. Furthermore, in many cases the cement is injected for hundreds of metres along the well, so that the interface between the cement and the mud tends to be parallel to the axis of the well, with its position varying slowly along the well. As well as the process of injection of the cement into the well, the late-time adjustment of the cement interface associated with the density differences between the phases is of interest. Given the aspect ratio of the well, an azimuthal gravity-driven flow may develop if the interface between the mud and cement is not horizontal in the cross-annulus plane. There may also be a long-time along-axis flow owing to variations in the depth of the flow along the well. Since the gradient of the interface in the along-axis direction will be small, owing to the long distances travelled by the cement along the well, the slope of the interface in the cross-annulus direction, which arises from the detailed pattern of flow along the annulus, may be dominant,

and hence we focus on the gravity-driven flow around the annulus (figure 2.1). In order to understand the fluid mechanics of such an adjustment flow, we consider the idealised problem in which we neglect the along-axis flow, and explore how the adjustment around the annulus occurs for a range of initial conditions. This class of problem is of interest in itself as it is different from the classical viscous gravity current (Huppert, 1982b) or viscous exchange flow problems (Matson and Hogg, 2012), as we emphasise in our analysis. While the range of initial conditions we cover may exceed those likely to arise in the drilling problem, the more extensive analysis reported herein leads to insight into the controls on this general class of flows.

In this chapter we study this late-time azimuthal adjustment of the cement-mud interface, focusing on the time scale for the flow to relax to a vertically stratified stable regime when initially the interface is inclined. In §2.3 we develop the theory, neglecting surface tension effects, such that the contact between the fluid-fluid interface and the annulus walls does not play a role in limiting the current propagation rate (Takagi and Huppert, 2007). In §2.4 several flow regimes are identified and a critical mass condition derived. In §2.5 and §2.6 we present numerical and asymptotic solutions to describe the different flow regimes. Finally, we end with a discussion of how the initial cross-sectional distribution of the cement will play an integral role in the quality of the cementing process.

2.3 Theory

Consider two viscous incompressible fluids of viscosity μ and densities ρ_I, ρ_O. The fluids are stably stratified in density such that $\rho_I < \rho_O$, and are separated by a sharp density interface $h(\theta, t)$. The velocity of each fluid in the azimuthal direction is denoted u_I and u_O. As shown schematically (figure 2.1) the domain of interest is a thin annulus of inner radius R and gap width $H \ll R$. We define r to be the radial coordinate, as

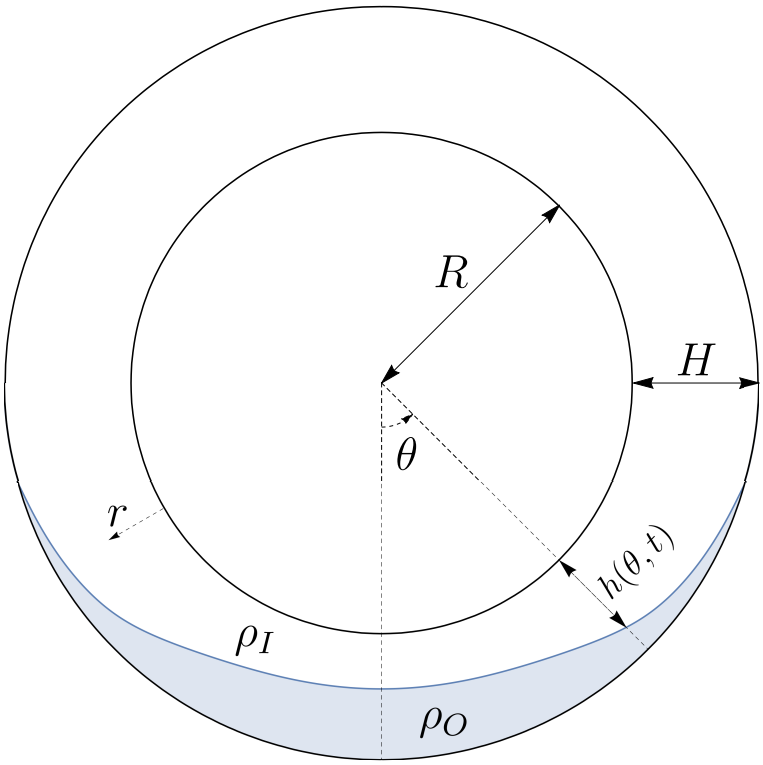

Fig. 2.1 A schematic of the system under consideration

measured from the inner wall, and θ to be the azimuthal coordinate, as measured from the base of the annulus.

Given such a geometry, we can write in generic terms the incompressible continuity equation (2.1) and the two-dimensional polar Navier-Stokes equations in radial (2.2) and azimuthal (2.3) components as follows:

$$\frac{1}{R+r}\frac{\partial((R+r)u_r)}{\partial r} + \frac{1}{R+r}\frac{\partial u_\theta}{\partial \theta} = 0 \tag{2.1}$$

$$\begin{aligned}\rho\left(u_r\frac{\partial u_r}{\partial r} + \frac{u_\theta}{R+r}\frac{\partial u_r}{\partial \theta} - \frac{u_\theta^2}{R+r}\right) = -\frac{\partial p}{\partial r} + \rho g\cos\theta + \\ \mu\left(\frac{1}{(R+r)}\frac{\partial}{\partial r}\left((R+r)\frac{\partial u_r}{\partial r}\right) - \frac{u_r}{(R+r)^2} + \frac{1}{(R+r)^2}\frac{\partial^2 u_r}{\partial \theta^2} - \frac{2}{(R+r)^2}\frac{\partial u_\theta}{\partial \theta}\right)\end{aligned} \tag{2.2}$$

$$\rho\left(u_r\frac{\partial u_\theta}{\partial r}+\frac{u_\theta}{R+r}\frac{\partial u_\theta}{\partial\theta}+\frac{u_r u_\theta}{R+r}\right)=-\frac{1}{R+r}\frac{\partial p}{\partial\theta}-\rho g\sin\theta+ \\ \mu\left(\frac{1}{(R+r)}\frac{\partial}{\partial r}\left((R+r)\frac{\partial u_\theta}{\partial r}\right)-\frac{u_\theta}{(R+r)^2}+\frac{1}{(R+r)^2}\frac{\partial^2 u_\theta}{\partial\theta^2}+\frac{2}{(R+r)^2}\frac{\partial u_r}{\partial\theta}\right) \tag{2.3}$$

As we are making a thin-gap approximation progress can be made by reducing the governing equations to leading order terms. This is done by considering the relative sizes of each term, equivalent in method to classical lubrication theory. We introduce the following scales for the radial velocity $u_r \sim U_r$, azimuthal velocity $u_\theta \sim U_\theta$, radial co-ordinate $r \sim H$ and pressure $p \sim P$. Considering just the sizes of each term, and recalling $H \ll R$, from the continuity equation 2.1 we have

$$U_r \sim \frac{H}{R}U_\theta, \tag{2.4}$$

which is consistent with our expectation that in a thin gap the azimuthal velocity will the dominate radial velocity. Substituting this scaling into the azimuthal momentum equation (2.3) and again considering only the sizes of terms we have

$$\rho\left(\frac{U_\theta^2}{R}+\frac{U_\theta^2}{R}+\frac{HU_\theta^2}{R^2}\right)=-\frac{P}{R}-\rho g\sin\theta+\mu\left(\frac{U_\theta}{H^2}+\frac{U_\theta}{RH}-\frac{U_\theta}{R^2}+\frac{HU_\theta}{R^3}-\frac{U_\theta}{R^2}\right) \tag{2.5a}$$

$$\rho\frac{U_\theta^2}{R}\left(1+1+\frac{H}{R}\right)=-\frac{P}{R}-\rho g\sin\theta+\frac{\mu U_\theta}{H^2}\left(1+\frac{H}{R}-\frac{H^2}{R^2}+\frac{H^3}{R^3}-\frac{H^2}{R^2}\right) \tag{2.5b}$$

$$\frac{H}{R}\frac{\rho U_\theta H}{\mu}\left(1+1+\frac{H}{R}\right)=-\frac{PH^2}{\mu UR}-\frac{\rho g\sin\theta H^2}{\mu U_\theta}+1+\frac{H}{R}-\frac{H^2}{R^2}+\frac{H^3}{R^3}-\frac{H^2}{R^2}. \tag{2.5c}$$

Assuming $\rho UH/\mu = O(1)$ and discarding terms $O(H/R)$ and smaller, we can see the remaining leading order terms give a balance between pressure gradient, body force, and viscous stresses. Hence, the leading order governing equation of motion in the azimuthal direction can be written

$$\frac{1}{R}\frac{\partial p}{\partial\theta}=\mu\frac{\partial^2 u_\theta}{\partial r^2}-\rho g\sin\theta \tag{2.6}$$

A similar approach can be taken with the radial momentum equation (2.2):

$$\rho\left(\frac{HU_\theta^2}{R^2}+\frac{HU_\theta^2}{R^2}-\frac{U_\theta^2}{R}\right)=-\frac{P}{H}+\rho g\cos\theta+\mu\left(\frac{U_\theta}{RH}+\frac{U_\theta}{R^2}-\frac{U_\theta}{R^2}+\frac{HU_\theta}{R^3}-\frac{U_\theta}{R^2}\right) \tag{2.7a}$$

$$\frac{H}{R}\rho U_\theta^2\left(\frac{H}{R}+\frac{H}{R}-1\right)=-P+\rho gH\cos\theta+\frac{\mu U_\theta}{H}\frac{H}{R}\left(1+\frac{H}{R}-\frac{H}{R}+\frac{H^2}{R^2}-\frac{H}{R}\right) \tag{2.7b}$$

$$\frac{H}{R}\frac{\rho U_\theta H}{\mu}\left(\frac{H}{R}+\frac{H}{R}-1\right)=-\frac{PH}{\mu U_\theta}+\frac{\rho gH^2\cos\theta}{\mu U_\theta}+\frac{H}{R}\left(1+\frac{H}{R}-\frac{H}{R}+\frac{H^2}{R^2}-\frac{H}{R}\right) \tag{2.7c}$$

Again omitting terms of size H/R and smaller, we are left with only pressure gradient and body force terms at leading order. That is, the governing equation of motion in the radial direction can be reduced to

$$\frac{\partial p}{\partial r}=\rho g\cos\theta. \tag{2.8}$$

Equation 2.8 represents the approximation that the pressure p in the radial direction varies hydrostatically, with

$$p(r,\theta)=\begin{cases} p_0(\theta)+\rho_I gr\cos\theta \quad \text{if} \quad 0\le r\le h, \\ \\ p_0(\theta)+\rho_I gh\cos\theta+\rho_O g\left(r-h\right)\cos\theta \quad \text{if} \quad h\le r\le H, \end{cases} \tag{2.9}$$

and where $p_0(\theta)$ is the unknown pressure on the inner wall. We can substitute equation 2.9 into equation 2.6 to obtain a pair of equations for the inner and outer layer respectively:

$$\frac{1}{R}\left(\frac{dp_0}{d\theta}-\rho_I gr\sin\theta\right)=\mu\frac{d^2u_I}{dr^2}-\rho_I g\sin\theta, \tag{2.10a}$$

$$\frac{1}{R}\left(\frac{dp_0}{d\theta}-\rho_O gr\sin\theta-\Delta\rho gh\sin\theta+\Delta\rho g\frac{dh}{d\theta}\cos\theta\right)=\mu\frac{d^2u_O}{dr^2}-\rho_O g\sin\theta \tag{2.10b}$$

To write equations 2.10 in dimensionless form it is helpful to introduce the following scalings

$$h = H\hat{h}, \quad r = H\hat{r}, \quad \theta = \sqrt{\frac{2H}{R}}\varphi, \quad p_0 = \rho_0 g H \hat{p}_0, \quad u = \frac{\rho_0 g H^2}{\mu}\sqrt{\frac{2H}{R}}\hat{u} \tag{2.11a, b, c, d}$$

where hat denotes a dimensionless quantity. The scaling for θ is found by considering that

$$\cos\theta = \frac{R}{R+H} \tag{2.12}$$

when a flat interface at steady state just touches the inner annulus wall (defined as the critical volume case in figure 2.2*b*) and then performing a leading order expansion of cosine. The scaling for p_0 is found from equation 2.8 and ρ_0 is a characteristic density. The dimensionless inner and outer layer densities are written $\hat{\rho}_I$ and $\hat{\rho}_O$ respectively. Substituting in the scalings to equations 2.11; additionally, given $\theta \ll 1$ from equation 2.11*c*, making small angle approximations for the trigonometrical functions, and then omitting terms $O(H/R)$ gives us

$$\frac{1}{2}\frac{d\hat{p}_0}{d\varphi} = \frac{d^2\hat{u}_I}{d\hat{r}^2} - \hat{\rho}_I\varphi, \tag{2.13a}$$

$$\frac{1}{2}\left(\frac{d\hat{p}_0}{d\varphi} + \Delta\hat{\rho}\frac{d\hat{h}}{d\varphi}\right) = \frac{d^2\hat{u}_O}{d\hat{r}^2} - \hat{\rho}_O\varphi, \tag{2.13b}$$

where $\Delta\hat{\rho} = \hat{\rho}_O - \hat{\rho}_I$ is the difference between inner and outer layer dimensionless densities. Dropping hats for brevity, we can now integrate equations 2.13 to obtain equations for the velocities u_I and u_O:

$$u_I = \frac{1}{4}\left(\frac{dp_0}{d\varphi} + 2\rho_I\varphi\right)r^2 + C_1 r + C_2, \tag{2.14a}$$

$$u_O = \frac{1}{4}\left(\frac{dp_0}{d\varphi} + 2\rho_O\varphi + \Delta\rho\frac{dh}{d\varphi}\right)r^2 + C_3 r + C_4. \tag{2.14b}$$

The unknown expressions C_1, C_2, C_3 and C_4 can be calculated with the application of four boundary conditions. Firstly, the speed parallel to the annulus walls is zero. Secondly, the velocity is continuous across the density interface, $r = h$. Finally, the viscous shear stress is continuous across the density interface. Thus

$$u_I(0) = u_O(1) = 0, \quad u_I(h) = u_O(h), \quad \frac{\partial u_I}{\partial r}(h) = \frac{\partial u_O}{\partial r}(h). \qquad (2.15a, b, c)$$

Now we have a pair of equations for u_I and u_O in terms of the unknown pressure gradient p_{0_φ} and interfacial functions h and h_φ. To obtain expressions for p_{0_φ} and h_φ, we assume that there is no net flux,

$$\int_0^h u_I \, \mathrm{d}r = -\int_h^1 u_O \, \mathrm{d}r. \qquad (2.16)$$

Finally, we can use the global continuity equation (Acheson, 1990)

$$\frac{H}{T}\frac{\partial h}{\partial t} + \frac{\rho_0 g H^3}{R\mu}\frac{\partial}{\partial \varphi}\left(\int_0^h u_I \, \mathrm{d}r\right) = 0, \qquad (2.17)$$

and a scaling for time $t = 6R\mu T/\rho_0 g H^2 \Delta\hat{\rho}$ to obtain a dimensionless partial differential equation that describes the movement in time and space of the density interface $h(\varphi, t)$:

$$\frac{\partial h}{\partial t} + \frac{\partial}{\partial \varphi}\left[h^3(1-h^3)\left(2\varphi - \frac{\partial h}{\partial \varphi}\right)\right] = 0. \qquad (2.18)$$

We note that in the governing equations 2.10 we have taken the viscosity of each layer to be the same. Data from studies on the rheology of typical drilling lubricant (Kudaikulova, 2015) and oil well cement (Shahriar, 2011) suggest that a viscosity difference between the layers $\Delta\mu \ll 1$ is a good approximation.

Furthermore, we also note that following a similar shallow-water analysis, the effects of surface tension would lead to an additional pressure term of the form

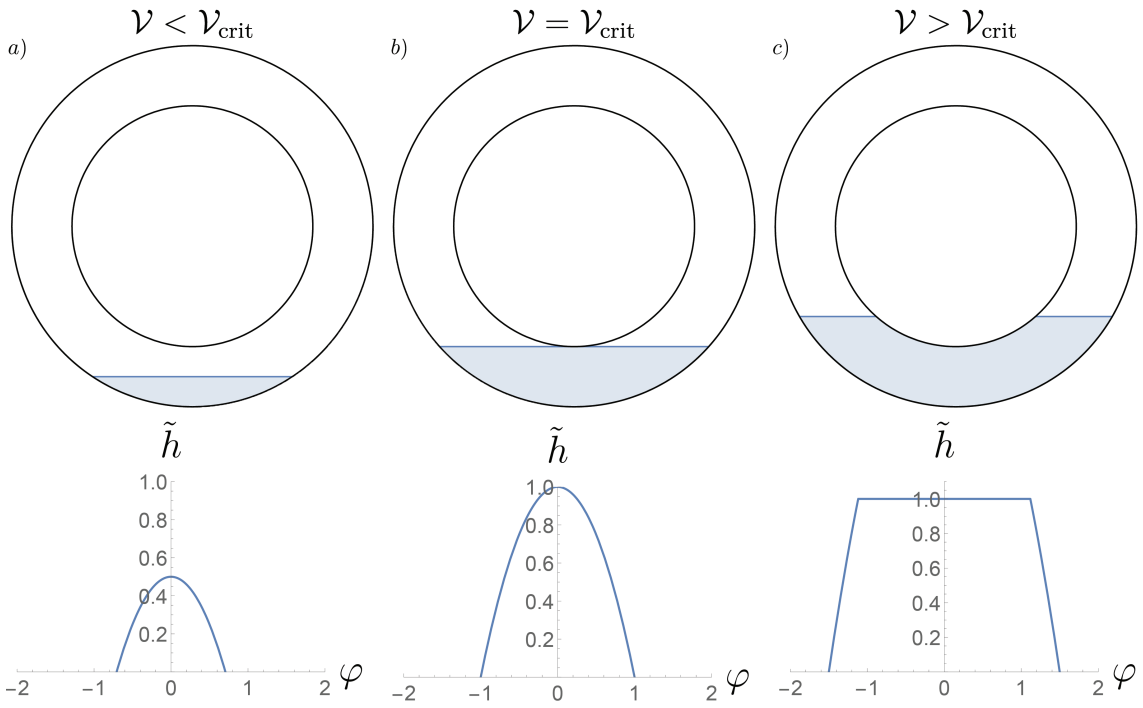

Fig. 2.2 Steady state solutions of a varying initial volumes $\mathcal{V}$ of dense fluid in physical space and $\tilde{h}, \varphi$ space. Figures correspond to (a) the small volume case $\mathcal{V} < \mathcal{V}_{\text{crit}}$, (b) the critical case $\mathcal{V} = \mathcal{V}_{\text{crit}}$ and (c) the large volume case $\mathcal{V} > \mathcal{V}_{\text{crit}}$.

$\sigma h_{\theta\theta\theta}$ (Myers, 1998) in addition to the term $\Delta\rho g h_\theta$ arising from the buoyancy: the surface tension effect only dominates the buoyancy force if the length scale of the flow $L < \sqrt{\sigma/\Delta\rho g} \sim 0.003$m. This is smaller than the typical length scales of 0.1-1.0m of interest in the present problem, and hence we do not include it in the present analysis.

2.4 Regimes

The final steady-state distribution of the cement and mud involves the interface between the relatively dense cement and the mud being horizontal. The geometry of the annulus leads to two different regimes. With a small volume of cement (per unit length along the axis) relative to the volume of the annulus (per unit length along the axis), the interface will be close to the base of the annulus and will not intersect the inner cylinder (figure 2.2a). However, with a larger mass of cement, the interface will intersect the

inner cylinder, leading to two spatially separate interfaces on each side of the annulus (figure 2.2c). To leading order the critical volume of cement at which the interface just touches the inner cylinder (shown in figure 2.2b) can be found. For convenience we define $\tilde{h} = 1 - h$ such that interface is measured from the outer annulus wall and hence the dimensionless volume of cement at steady state is given by

$$\mathcal{V} = \int_{-\varphi_{\text{steady}}}^{\varphi_{\text{steady}}} \tilde{h} \, \mathrm{d}\varphi \tag{2.19}$$

where φ_{steady} is defined as the the angle where the interface meets the outer annulus wall at steady state. Alternatively this can be seen as the values of φ at the point where the curves intersect the φ axis, as shown in the lower panel of figure 2.2.

Analysis of equation 2.18 leads to the recognition that there are three steady state solutions. Two of these solutions are trivial and relate to the cases when $h = 0$ and $h = 1$, which can be understood to mean when the annulus is entirely full of either fluid and the interface sits on the inner or outer annulus wall. The non-trivial solution, corresponding to the physical steady states represented in figure 2.2, is given by

$$\tilde{h} = \varphi_{\text{steady}}^2 - \varphi^2 \tag{2.20}$$

As θ was scaled by considering the geometry of the system at the critical case (equation 2.11c) the gives a value of $\varphi_{\text{steady}} = 1$ for the critical case. Putting this with equation 2.19 allows us to deduce that the critical volume of cement is

$$\mathcal{V}_{\text{crit}} = 4/3. \tag{2.21}$$

In the case when $\mathcal{V} > \mathcal{V}_{\text{crit}}$ we have two spatially separate interfaces, with piecewise steady state solutions given by

$$\tilde{h} = \begin{cases} \varphi^2_{\text{steady}} - \varphi^2 & \text{if} \quad \varphi < -\sqrt{1-\varphi^2_{\text{steady}}} \text{ or } \varphi > \sqrt{1-\varphi^2_{\text{steady}}}, \\ 1 & \text{if} \quad -\sqrt{1-\varphi^2_{\text{steady}}} \leq \varphi \leq \sqrt{1-\varphi^2_{\text{steady}}}. \end{cases} \tag{2.22}$$

Figure 2.3 illustrates how the volume $\mathcal{V}$ varies as a function of φ_{steady}. We note the change of behaviour as the regime changes from the small-volume to large-volume case at $\mathcal{V}_{\text{crit}}$.

We now explore the transition to these steady states, for the cases of $\mathcal{V} < \mathcal{V}_{\text{crit}}$, the small-volume case, and $\mathcal{V} > \mathcal{V}_{\text{crit}}$ the large-volume case. There are many different possible initial conditions, but in order to gain a systematic understanding of the process of adjustment to equilibrium, we have parametrised the initial condition in terms of a series of partial concentric annuli, which we parametrise as $h(\varphi) = h_0$ (const) for $-\varphi_{\text{init}} < \varphi < \varphi_{\text{init}}$. An illustration of φ_{init} and φ_{steady} can be seen in figures 2.4a and 2.4f respectively.

To simulate the evolution of the density interface $h(\varphi, t)$, we have solved equation 2.18 using the numerical method of lines (Schiesser, 2012). First we discretise the spatial derivative φ in equation 2.18 such that we are left with n ODEs. Setting the range over which we wish to integrate in φ as $[L, R]$ we have spatial step-size as $d = (L - R)/n$. From this we can discretise φ as follows, exploiting the the symmetry

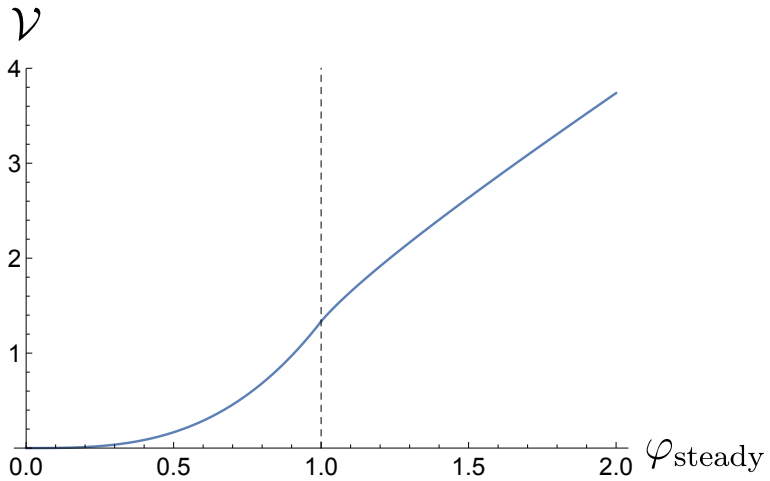

Fig. 2.3 illustrates how dimensionless mass $\mathcal{V}$ varies as a function of φ_{steady} the angle steady state which the interface meets the outer annulus wall. The dashed line at $\varphi_{\text{steady}} = 1$ separates the two small volume and large volume regimes. In the small volume regime there is a single steady state interface. In the large volume regime we have a piecewise interface which intersects the inner cylinder.

of PDE:

$$h_p = \frac{h(i+1,t) + h(i,t)}{2}, \tag{2.23a}$$

$$dh_p = \frac{h(i+1,t) - h(i,t)}{d}, \tag{2.23b}$$

$$h_m = \frac{h(i,t) + h(i-1,t)}{2} \tag{2.23c}$$

$$dh_m = \frac{h(i,t) - h(i-1,t)}{d}. \tag{2.23d}$$

Substituting these equations into equation 2.18, indexed over i, gives n ODEs of the form

$$\frac{dh(i,t)}{dt} = \frac{1}{d}\left(h_p^3(1-h_p)^3(dh_p - 2L + d(2i-1)) - h_m^3(1-h_m)^3(dh_m - 2L + d(2i-3))\right). \tag{2.24}$$

We then solve these coupled ODEs via adaptive switching between backward differentiation formulae, first introduced by Curtiss and Hirschfelder (1952). This is a well known and widely implemented ODE solving method, which is particularly suited

to stiff differential equations since the adaptive behaviour can vary which difference formula is used to ensure stability and accuracy around stiff regions. This is suited to our problem around the region of large gradient where the interface meets the outer annulus wall. We use the Wolfram Mathematica implementation of the backward differentiation method.

To ensure the accuracy of the numerical solutions, we tested a number of ODEs $n = 200, 500, 1000$ and 2000. We found that, as we increased the number of points, the adjustment time required to reach equilibrium converged to constant values, with the difference in this adjustment time between a grid with $n = 1000$ spatial points and $n = 2000$ points being less than 0.1% in all simulations. Furthermore, to check the validity of our numerical scheme, we checked for conservation of volume at each time step. For each simulation, the difference between the initial and final volumes was smaller than 0.1%.

2.5 Small volume ($\mathcal{V} < \mathcal{V}_{\text{crit}}$)

To analyse the small-volume case suppose, at steady state, we wish the fluid to fill half the gap width at $\varphi = 0$. From equations 2.19 and 2.20 we have $\mathcal{V} = \sqrt{2}/3 < \mathcal{V}_{\text{crit}}$ and $\varphi_{\text{steady}} = \sqrt{2}/2$. We will now vary the initial conditions $h(\varphi, 0) = h_0$ between $-\varphi_{\text{init}} < \varphi < \varphi_{\text{init}}$, whilst maintaining the same mass (per unit length along the axis) $\mathcal{V} = \sqrt{2}/3$.

2.5.1 Exchange flow

The first partial concentric annulus we select as an initial condition is $h_0 = 0$ (equivalently $\tilde{h} = 1$). This gives us an initial distribution of fluid that is in contact with the upper boundary of the annulus. For our choice of $\mathcal{V}$ we arrive at $\varphi_{\text{init}} = \sqrt{2}/6 < \varphi_{\text{steady}}$.

A time series of the interface shape as predicted by the numerical solutions is shown in figure 2.4. There are three distinct periods of adjustment from the initial condition to the steady state. Firstly, there is an exchange flow occurring between the dense fluid ρ_O and light fluid ρ_I (figures 2.4a and 2.4b). A short time later the interface pinches from the inner annulus wall (figure 2.4c) and relaxes. The final period of flow is an equilibration to the steady state (figures 2.4d, 2.4e and 2.4f).

We note that the detailed process of pinch-off leads to a short period of time during which the radius of curvature of the interface decreases to very small values, although before and after this short interval, the radius of curvature has much larger values (figure 2.4$a - c$). During the pinch-off, the effects of surface tension may therefore become important, limiting the decrease in the radius of curvature at the point at which the interface detaches from the upper boundary. However, this does not have a significant influence on the overall time of relaxation of the interface towards the final steady state. This may be understood by observing that the pinch-off time in the present calculations represents a negligible fraction of the total relaxation time (figure 2.4c, d), and the effect of surface tension will be to accelerate the pinch-off, and so we have not included the detail of this in the present calculation.

In order to illustrate the key impact of the curvature of the boundary on the flow, and the establishment of a steady state, we have compared the numerical solution for annular exchange flow with the case of two fluids of differing density exchanging in a purely horizontal channel, with the same initial conditions. In this case, φ represents the along-channel coordinate. In figure 2.5a profiles of the interface are shown at three times with solid black lines for the annulus and dashed lines for the flat channel. It is seen that, during the initial phase of the flow, while the dense fluid remains attached to the upper boundary of the domain, the flow resembles a classical exchange flow, and the effect of the curvature marginally slows the rate of exchange between the two fluids.

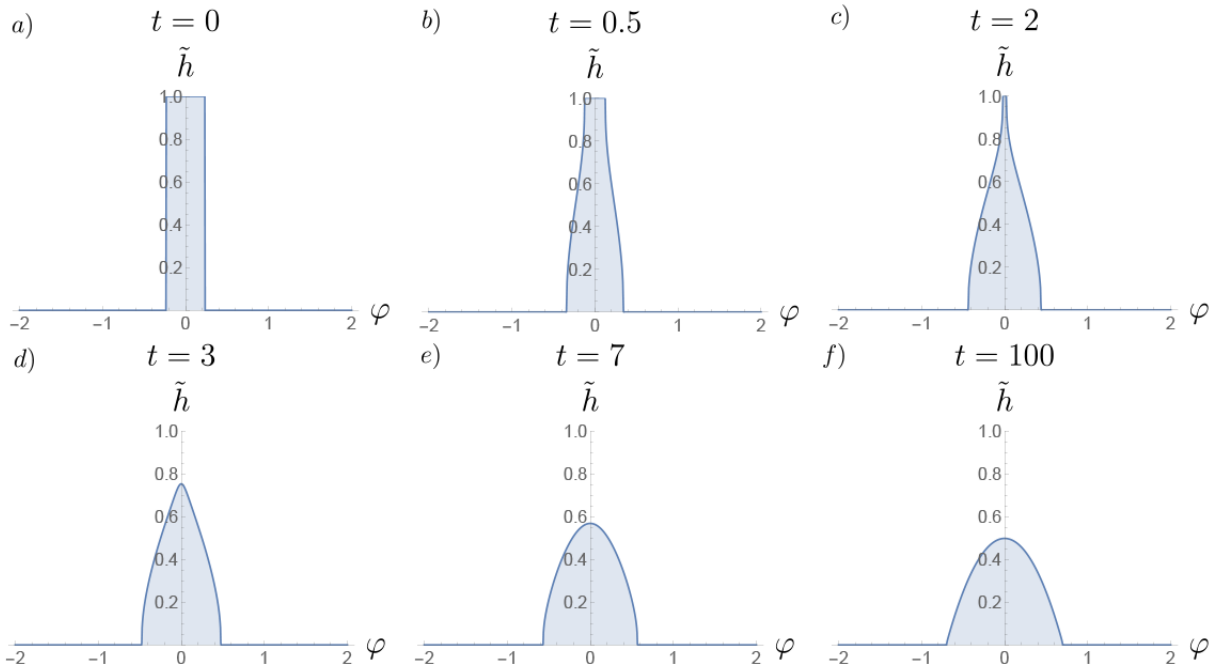

Fig. 2.4 $\varphi_{\text{init}} = \sqrt{2}/6$. Each figure corresponds to different parts of the flow evolution at various times t. (a) The initial state $t = 0$, (b) dense and light fluids exchanging $t = 0.5$, (c) pinch-off of the interface $t = 2$, (d) relaxation $t = 3$, (e) equilibration $t = 7$ and (f) steady state $t = 100$.

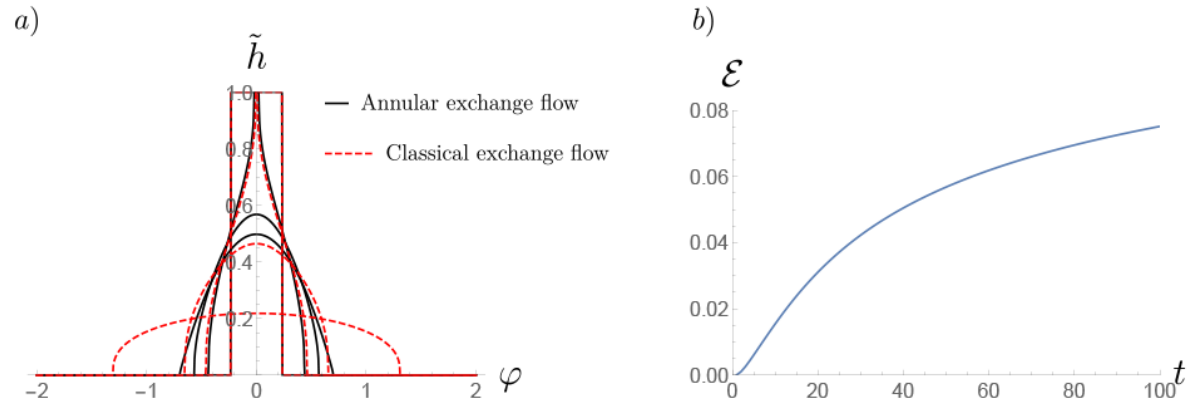

Fig. 2.5 (a) A series of snapshots in time $t = 0, 2, 7, 100$. The two currents start off with the same initial condition, but the curvature can be seen to affect the flow of the annular gravity current, bringing it a stop in finite time with $h(0) \to 0.5$. The classical current flows for an infinite time with $h(0) \to 0$. (b) A demonstration of how the quantity $\mathcal{E}$ changes as a function of t.

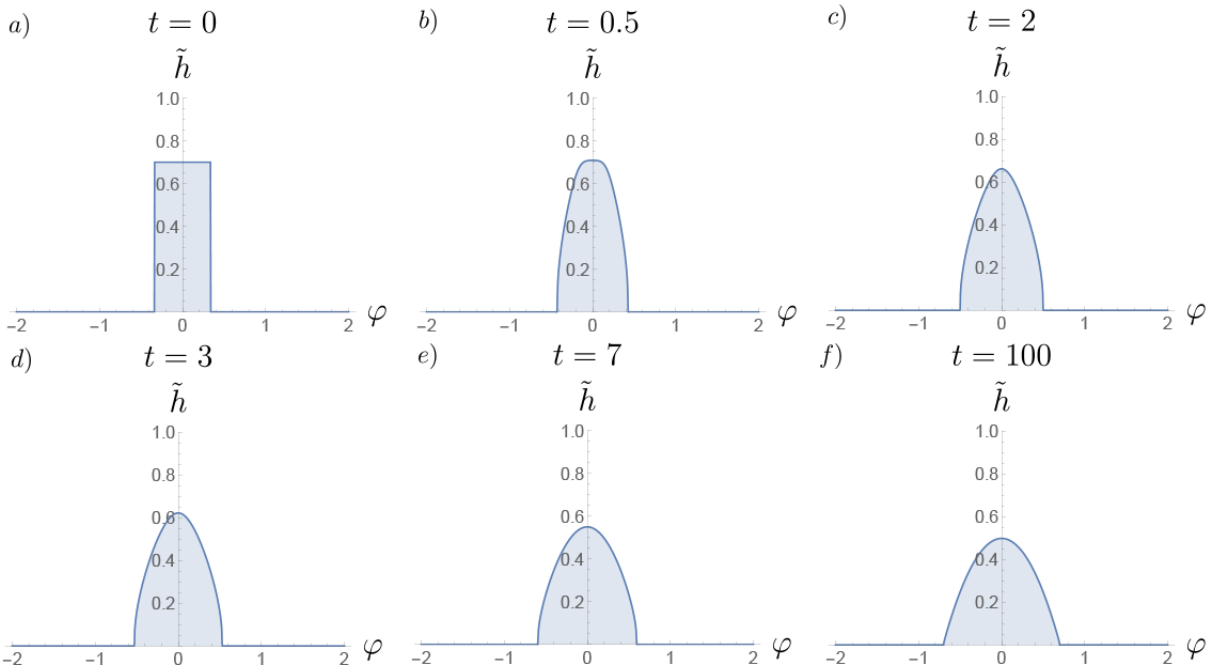

Fig. 2.6 $\varphi_{\text{init}} \approx 0.337$. Each figure corresponds to different parts of the flow evolution at various times t. (a) The initial state, (b,c) the dense fluid begins to slump, (c,d) the fluid spreads and begins to equilibrate and (f) steady state.

However, once the fluid separates from the upper boundary (figure 2.5a, $t = 2$) the difference between the solutions becomes more striking, with the fluid adjusting to the steady solution in the annulus, while the fluid adjusts to a classical gravity current in a confined horizontal channel (Huppert, 1982b; Matson and Hogg, 2012; Zheng et al., 2015). In order to illustrate this difference, it is useful to follow the evolution of the quantity

$$\mathcal{E}(t) = \int \left[h_{\text{classical}}(\varphi, t) - h_{\text{annulus}}(\varphi, t)\right]^2 \, \mathrm{d}\varphi, \tag{2.25}$$

as shown in figure 2.5b.

2.5.2 Gravity-current-like case

We can explore a further initial condition in the $\varphi_{\text{init}} < \varphi_{\text{steady}}$ regime by selecting a partial concentric annulus of $h_0 = 0.3$ ($\tilde{h} = 0.7$), which leads to $\varphi_{\text{init}} \approx 0.337$. This

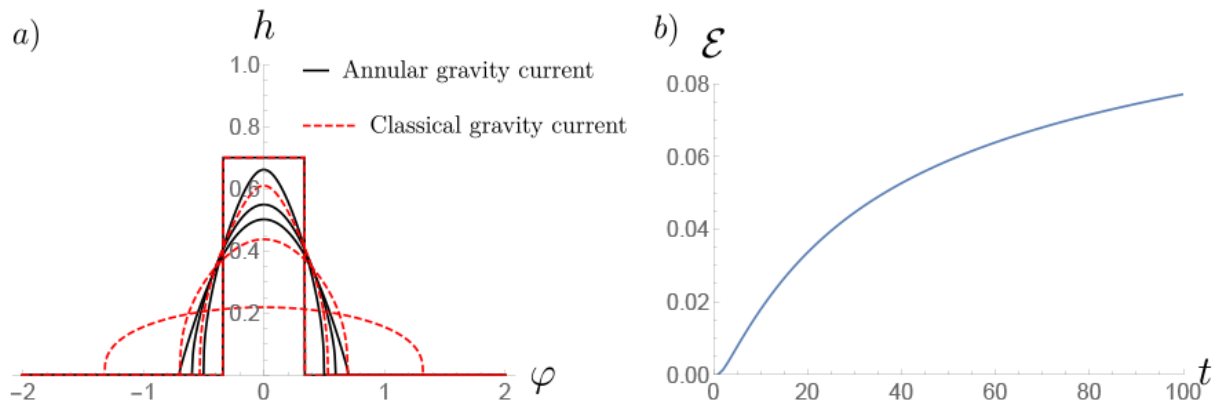

Fig. 2.7 (a) A series of snapshots in time $t = 0, 2, 7, 100$. The two currents start off with the same initial condition, but the curvature can be seen to affect the flow of the annular gravity current, bringing it a stop in finite time with $\tilde{h}(0) \to 0.5$. The classical current flows for an infinite time with $\tilde{h}(0) \to 0$. (b) A demonstration of how the quantity $\mathcal{E}$ changes as a function of t.

condition differs qualitatively from the previous solution shown in §2.5.1, as the dense fluid is not in contact with the inner annulus boundary. A visualisation of the full numerical simulation is seen in figure 2.6. In this case, the flow initially behaves analogously to a classical gravity current. At first there is a slumping regime with the dense fluid running along the lower boundary; however, in the annular case the curvature of the domain begins to restrict the flow (figures 2.6a, b, c), as the along-boundary component of gravity suppresses the flow (figures 2.6d, e, f). Eventually the annular current stops flowing and is brought to a horizontal steady state. The disparity between the classical gravity current and the present annular flow can be seen in figure 2.7a, with φ again representing the along-channel coordinate for the classical case. The difference function $\mathcal{E}$ (equation 2.25) is again calculated for this gravity-current-like case and shown in figure 2.7b.

2.5.3 Draining

By choosing a partial concentric annulus with initial depth $h_0 = 0.8$ ($\tilde{h} = 0.2$), we enter a regime where $\varphi_{\text{init}} \approx 1.179 > \varphi_{\text{steady}}$. In this case the flow exhibits draining-

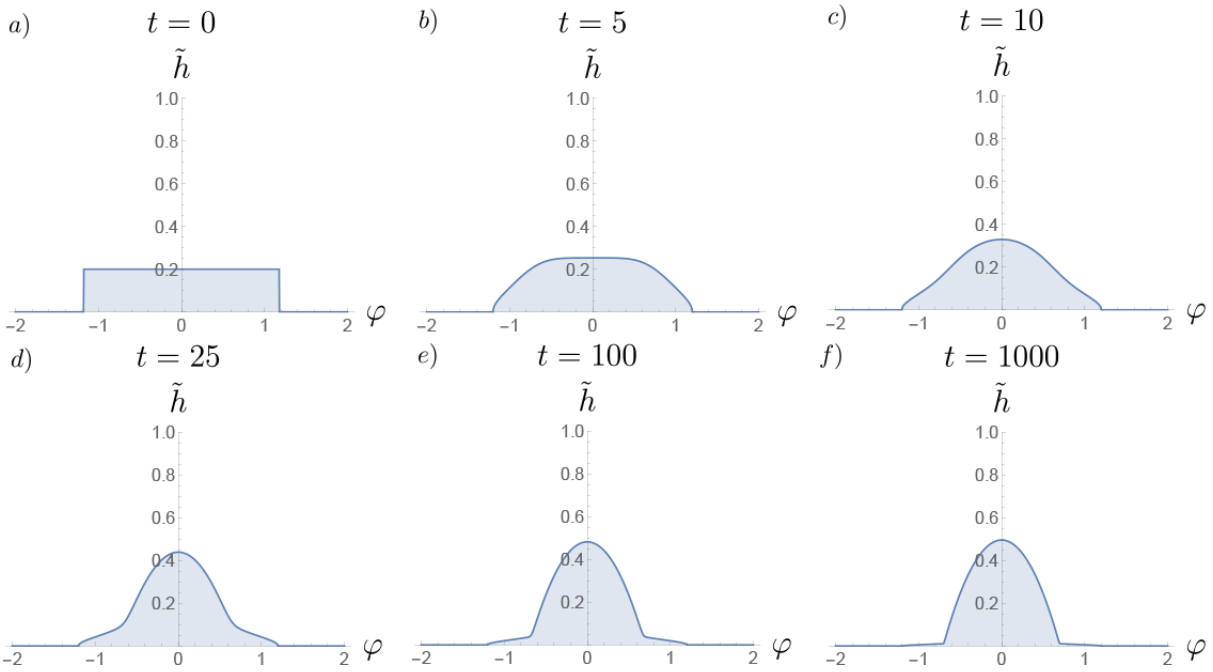

Fig. 2.8 $\varphi_{\text{init}} \approx 1.179$. Each figure corresponds to different parts of the flow evolution at various times t. (a) The initial state, $(b\text{-}c)$ dense fluid ρ_O fluid drains down the outer wall of the annulus, $(d\text{-}e)$ a thin film develops between φ_{steady} and φ_{init} and (f) steady state.

like behaviour. Dense fluid runs down the outer annulus wall, filling from the base. Figure 2.8 shows a visualisation of the numerical simulation. In the simulation a thin film develops between φ_{init} and φ_{steady}. This film gradually drains and tends to zero thickness over time.

Thin-film asymptotics

To analyse the decay of the thin film that develops, we can find a long-time asymptotic solution to equation 2.18. Firstly, we observe that, since $h \to 1$ in the film, the contribution from the h^3 term is approximately 1. Secondly, at long-time in the thin film the gradient h_φ is negligible. This leaves us with a reduced version of equation

2.18:

$$\frac{\partial h}{\partial t} \quad - \quad 6(1-h)^2\varphi\frac{\partial h}{\partial \varphi} = -2(1-h)^3. \tag{2.26}$$

We can solve this using the method of characteristics with initial condition $h(\varphi, 0) = h_0$,

$$\frac{dh}{ds} = 1 - h \Rightarrow h = 1 - e^{-s}\left(1 - h_0\right), \tag{2.27}$$

$$\frac{d\varphi}{ds} = 3\varphi \Rightarrow \varphi = \varphi_0 e^{3s}, \tag{2.28}$$

$$\frac{dt}{ds} = \frac{-1}{2(1-h)^2} = \frac{-e^{2s}}{4(1-h_0)^2}. \tag{2.29}$$

This leads to a solution for $h(\varphi, t)$ in terms of the transformed time s, given implicitly in terms of t according to

$$t = f(\varphi_0) + \frac{e^{2s}}{4(1-h_0)^2}, \tag{2.30}$$

Eliminating s gives us the general solution to equation to 2.26:

$$f\left(\frac{(1-h)^3\varphi}{(1-h_0)^3}\right) = t - \frac{1}{4(1-h)^2}. \tag{2.31}$$

We can use the same initial condition $h_0 = 0.3$ as in the full numerical simulation of §2.5.3 and an angle $\varphi_0 = 1$ within the film to check the convergence of the numerical solutions to this asymptotic approximation at long time. As can be seen in figure 2.9*a*, they are in good agreement.

2.5.4 Time adjustment

One of the key initial questions of this study relates to the time over which the flow adjusts to the equilibrium solution. In order for us to illustrate how this adjustment time varies with the initial distribution of fluid, it is useful to calculate the time at

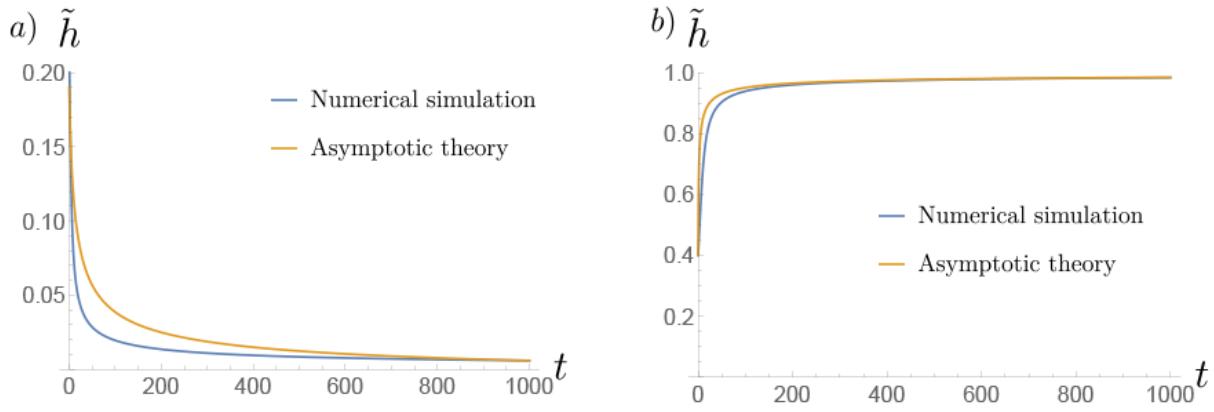

Fig. 2.9 (a) The decay of the outer dense layer ρ_O at angle $\varphi = 1$. The numerical simulation is in good agreement with the analytical solution of the asymptotic approximation. (b) The thinning of the inner light layer ρ_I at angle $\varphi = 0$. The numerical simulation is in good agreement with the analytical solution of the asmyptotic approximation.

which the area enclosed by the difference between the solution $h(\varphi, t)$ and the steady-state solution falls below the fractions 5 %, 10% and 20% of the area of the current. We have calculated this time from our numerical solutions for a continuous range of φ_{init}. We label the time taken for this adjustment process to occur as $t_{\text{adjust}}\,(x\%)$. The dimensionless adjustment time t_{adjust} is scaled as in equation 2.17. For the three individual simulations in §§2.5.1-2.5.3, we have $t_{\text{adjust}}\,(5\%) = 14.4, 16.5$ and 157.9, respectively.

As can be seen in figure 2.10a, the adjustment time t_{adjust} varies as a smooth function of φ_{init}. The qualitative shape of this adjustment function can be explained as follows. At small values of φ_{init} the region occupied by the fluid is at a low aspect ratio when compared to the region occupied at steady state. Thus the difference in volume between the two regions is relatively large and so it takes the fluid a relatively long time to adjust. As the values of φ_{init} are increased, the aspect ratio of the initial and final conditions become similar, reducing the initial difference in volume and hence the adjustment time. As values of φ_{init} are increased further, the initial condition is now of relatively high aspect ratio compared with the steady state, and as such the

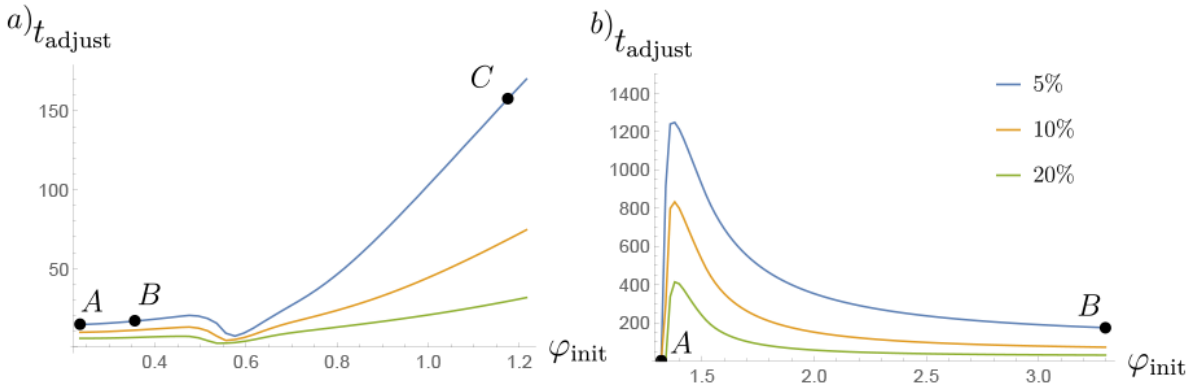

Fig. 2.10 (a) The time taken for an initial mass $\mathcal{V} = \sqrt{2}/3$ to adjust to within 5%, 10%, and 20% of its steady state varying the initial angle φ_{init} of the partial concentric annulus initial condition. The point A represents the exchange flow case demonstrated in §2.5.1, B the gravity current-like case demonstrated in §2.5.2 and C the draining case in §2.5.3. (b) The time taken for an initial mass $\mathcal{V} = 2.637$ to adjust to within 5%, 10%, and 20 % of its steady state varying the initial angle φ_{init} of the partial concentric annulus initial condition. The point A shows the restricted exchange flow case. The point B is the deepening and squeezing example of §2.6.2.

difference in volume is high and the adjustment time long. The process of adjustment through slumping as seen in small-φ_{init} cases is a faster process than that of draining and deepening as seen in large-φ_{init} cases.

2.6 Large volume ($\mathcal{V} > \mathcal{V}_{\text{crit}}$)

To analyse the transient adjustment problem in the case that the cement represents a significant fraction of the volume of the lower half of the annulus we choose $\mathcal{V} = 2.637$ and $\varphi_{\text{steady}} = 1.5$. In contrast to the small-volume regime the large-volume regime has only two distinct flow regimes.

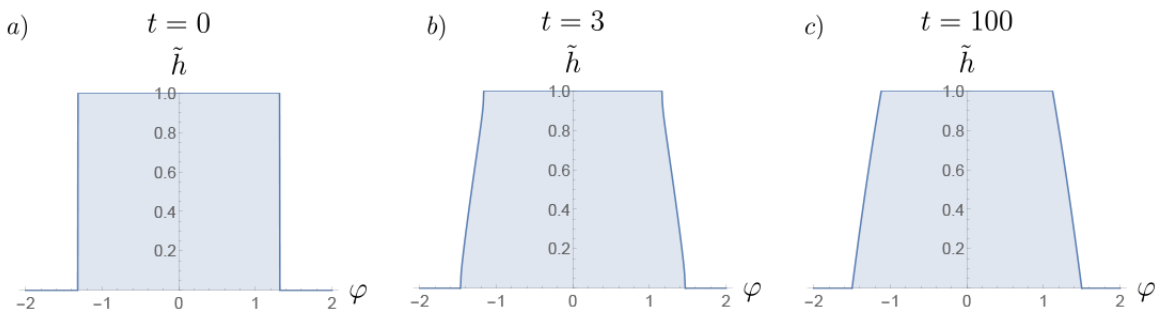

Fig. 2.11 $\varphi_{\text{init}} \approx 1.318$. Each figure corresponds to different parts of the flow evolution at various times t. (a) The initial state, (b) an exchange flow develops but is restricted by the curvature of the annulus and (c) steady state.

2.6.1 Restricted exchange flow

The first initial condition that we select is a partial concentric annulus that is in contact with the inner boundary of the annulus. For our choice of $\mathcal{V}$ we arrive at $\varphi_{\text{init}} \approx 1.318 < \varphi_{\text{steady}}$.

A time series of the evolution of the interface is shown in figure 2.11. The dense fluid and light fluid begin to exchange; however, owing to the curvature of the domain, the current is restricted and comes to rest with a horizontal interface on each side of the annulus, with a conjoining section of fluid in contact with the inner boundary.

A comparison could be drawn between the early-time classical exchange flow, before pinch-off, analogously to that shown in §2.5.1.

2.6.2 Deepening and squeezing

To analyse the case of the draining film flow, $\varphi_{\text{init}} > \varphi_{\text{steady}}$, we keep the parameters the same as in §2.6.1. However, now we select an initial partial concentric annulus $h_0 = 0.6$ $(\tilde{h} = 0.4)$, which requires $\varphi_{\text{init}} \approx 3.3$. A visualisation of the time evolution of the interface in this case can be seen in figure 2.12. The dense fluid at each of the far ends of the annulus develops a travelling front moving azimuthally, due to the advection, but also flattening, due to the diffusion. Movement of dense fluid downslope

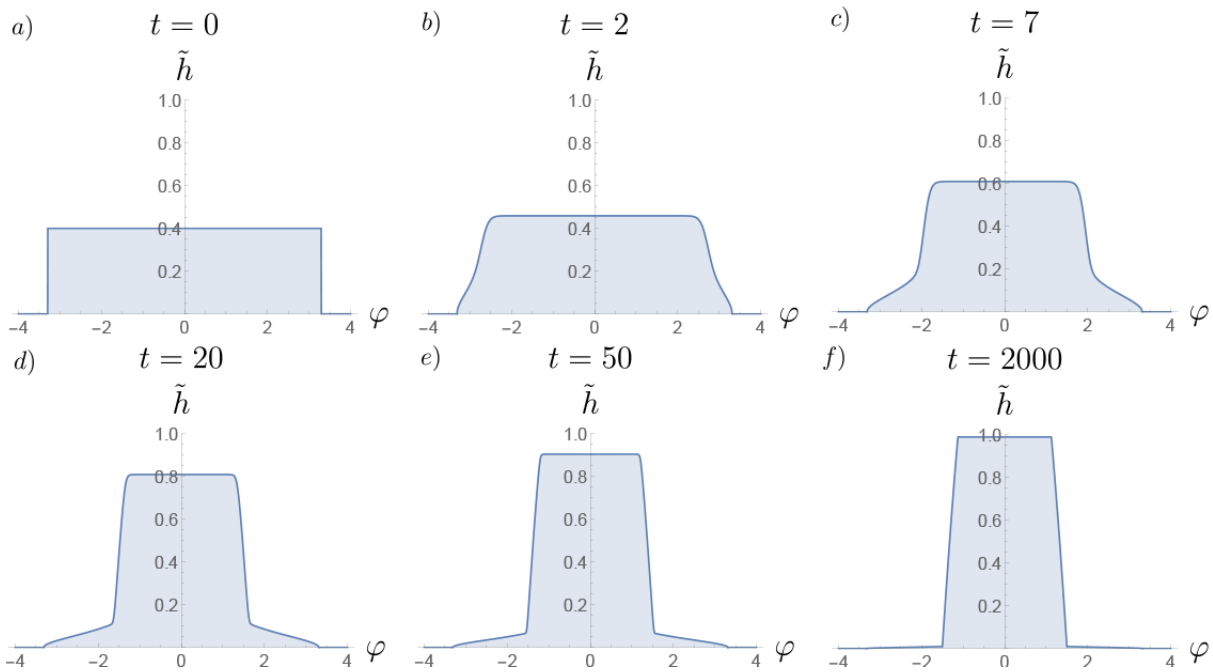

Fig. 2.12 $\varphi_{\text{init}} \approx 3.3$. Each figure corresponds to different parts of the flow evolution at various times t. (a) The initial state, $(b\text{-}c)$ the fluid flows down the outer wall with a shock forming, $(d\text{-}e)$ a thin film of light fluid forms between $\pm\varphi_{\text{steady}}$ which is then squeezed out by the dense fluid ρ_O, and (f) steady state.

causes a deepening of the fluid in the region $-\varphi_{\text{steady}} < \varphi < \varphi_{\text{steady}}$. This deepening of the pool of dense fluid at the base of the annulus leads to formation of a film of light fluid, which is gradually squeezed out from the region between the inner boundary and deepening layer of dense fluid. Eventually the system asymptotes to its final piecewise steady state.

Squeeze film asymptotics

We can analyse the squeezing of the thin film by making an asymptotic approximation to equation 2.18. Firstly, since $h \to 0$ (equivalently $\tilde{h} \to 1$) in the thin film, we can approximate the contribution of the $(1-h)^3$ term as being 1. Furthermore, the

contribution of h_φ in the thin film is negligible. This leads to the simplified equation

$$\frac{\partial h}{\partial t} + 6h^2\varphi\frac{\partial h}{\partial \varphi} = -2h^3. \tag{2.32}$$

We can solve this using the method of characteristics with $h(\varphi, 0) = h_0$ and $\varphi(0) = \varphi_0$,

$$\frac{dh}{ds} = -h \Rightarrow h = h_0 e^{-s}, \tag{2.33}$$

$$\frac{d\varphi}{ds} = 3\varphi \Rightarrow \varphi = \varphi_0 e^{3s}, \tag{2.34}$$

$$\frac{dt}{ds} = \frac{1}{2h^2} = \frac{1}{2h_0^2 e^{-2s}}. \tag{2.35}$$

Again we can find solutions $h(\varphi, t)$ in terms of the time-like parameter s given implicitly in terms of t by the relation

$$t = f(\varphi_0) + \frac{e^{2s}}{4h_0^2}. \tag{2.36}$$

Eliminating s gives us the general solution to equation 2.32

$$f\left(\frac{h^3\varphi}{h_0^3}\right) = t - \frac{1}{4h^2}. \tag{2.37}$$

We can use the same initial condition $\tilde{h} = 0.4$ as in the full numerical simulation of §2.6.2 and an angle $\varphi_0 = 0$ at the centre of the film to check our asymptotic approximation. As can be seen in figure 2.9*b*, the numerical solution is in good agreement with this approximate solution. This asymptotic solution suggests that the system takes an infinite amount of time to adjust to equilibrium.

2.6.3 Time adjustment

As before in §2.5.4, we can take a sweep of the φ_{init} space for a given volume of fluid and calculate the time taken for the difference in area to adjust to within 5%, 10% and

20% of the final steady state. Figure 2.10*b* shows how the adjustment time t_{adjust} varies with the initial angle φ_{init}. The large-volume regime is qualitatively different from the small-volume regime. The two values of dimensionless adjustment time $t_{\text{adjust}}(5\%)$ for the two simulations in §§2.6.1 and 2.6.2 are $t_{\text{adjust}} = 4.79$ and 173.8, respectively. For small values of φ_{init} the difference between the initial area and the steady-state area is small, so the adjustment time is relatively fast. As φ_{init} increases, the difference in volumes increases, so the adjustment time increases.

2.7 Discussion and Summary

We have demonstrated how two fluids confined within an annulus and with different density can adjust to equilibrium from an initial symmetric distribution. The adjustment time to steady state can vary considerably based on the initial mass and distribution of the two fluids within the annulus. As discussed previously, the distribution of cement inside a wellbore is crucial to the stability and integrity of the well and ultimately has important implications for any directional drilling project. The setting time of cement used for the mud displacement process is $\sim O(10^3 - 10^4)$s (Siddiqi, 2012). If we introduce some typical values for the time scaling used in 2.17, i.e. $R = 0.1$m, $H = 0.01$m, $\Delta\rho = 10\text{kg/m}^3$ and $\mu = 1$kg/ms, we find a relationship $t \approx 60\hat{t}$. Looking at the non-dimensional adjustment time to 5% in §§2.5.1-2.5.3, 2.6.1 and 2.6.2, we can see this corresponds to dimensional time adjustments of approximately 864s, 990s, 9474s, 287s and 10428s, respectively. So we can see that the setting time of cement is comparable to the adjustment time of the flow. This demonstrates that the initial distribution of dense fluid is important, as it could have an undesirable distribution around the annulus as it begins to set, perhaps allowing for non-cemented and therefore highly permeable channels around the casing to develop.

Chapter 3

A note on analytic solutions for entraining stratified gravity currents

3.1 Abstract

High-Reynolds-number steady currents of relatively dense fluid propagating along a horizontal boundary become unstable and mix with the overlying fluid if the gradient Richardson number across the interface is less than 1/4. The process of entrainment produces a deepening mixing layer at the interface, which increases the gradient Richardson number of this layer and eventually may suppress further entrainment. The conservation of the vertically averaged buoyancy and momentum flux, as the current advances along the boundary, leads to two integral constraints relating the downstream flow with that upstream of the mixing zone. These constraints are equivalent to imposing a Froude number in the upstream flow. Using the ansatz that the dowstream velocity and buoyancy profiles in the current have a lower well-mixed region overlain by an interfacial layer of constant gradient, we can use these two constraints to quantify

the total entrainment of ambient fluid into the flow as a function of the gradient Richardson number of the downstream flow. This leads to recognition that both subcritical and supercritical currents may develop downstream of the mixing zone. However, as the mixing increases and the interfacial layer gradually deepens, there is a critical point at which these two solution branches coincide. For each upstream Froude number, we can also determine the downstream flow with maximal entrainment. This maximal entrainment solution coincides with the convergence point of the supercritical and subcritical branches. We compare this with the entrainment predicted for those solutions with a gradient Richardson number of 1/4, which corresponds to the marginally stable case. As the upstream Froude number increases, the maximum depth of the interfacial mixing layer gradually increases until eventually, for $Fr_u > 2.921$, the whole current may become modified through entrainment. We discuss the relevance of these results for mixing in gravity-driven flows.

3.2 Introduction

Turbulent density currents are ubiquitous in geophysical, industrial, and environmental settings. Mixing, often driven and dominated by turbulence, plays a crucial role in the dynamics of these currents. Much effort has gone into the study of various examples of these flows. Clarke (1972), along with Garvine and Monk (1974), have studied naturally occurring sea-breeze fronts and saline estuary intrusions, analysing the density and velocity structure of such flows. Fay (1980) quantifies the dilution of dense gas leaks released in accidents. Ivey et al. (2008) reviews measurements of vertical mixing in geophysical environments, and there is a growing literature on mixing in gravity currents (Hallworth et al., 1993; Johnson and Hogg, 2013; Kneller et al., 2016; Liapidevskii, 1994; Samasiri and Woods, 2015; Sher and Woods, 2015, 2017).

The classic work of Ellison and Turner (1959) measured mixing in gravity-driven flows experimentally. Their data was combined with a depth-averaged model to explore the effect of entrainment of ambient fluid into the flow as it migrated downstream. Ellison and Turner (1959) recognised that the flow is in fact stratified with a vertical distribution of horizontal velocity and density as ambient fluid is mixed into the current. In their modelling they assumed that the structure of the stratification, as quantified by shape factors in the depth-averaged equations, is fixed.

Many works subsequent to Ellison and Turner (1959) have explored and refined the parameterisation of the mixing (Cenedese and Adduce, 2010; Strang and Fernando, 2001) and have used the parameterisation to model mixing in environmental and geophysical flows (Bursik and Woods, 1996; Johnson and Hogg, 2013; Xu et al., 2006). For horizontal currents, the depth-averaged model parameterises the mixing in terms of a bulk Richardson number, based on the buoyancy, the depth and the velocity, $Ri_b = \Delta g' h/u^2$. For a horizontal current, models typically assume the mixing reduces to very small values as the bulk Richardson number Ri_b approaches or increases beyond 1/4.

Depth-averaged models are very useful, but most analytical modelling has been developed using the assumption that the shape factors are constant. In this work we take a different approach and examine some global constraints on the evolution of an initially uniform current of one density supplied to the base of a deep well-mixed layer of fluid of lower density. We assume that the flow migrates along a horizontal boundary and we allow for gradual mixing across the interface between the two fluids, which produces an upper interfacial mixing layer which is stratified in velocity and density. The interface, in this case, is defined as the boundary between the region in which the time-averaged velocity and buoyancy have the same values as the background and those in the current. Throughout this chapter we refer to this stratified upper layer as

the interfacial mixing layer. Eventually, if the interfacial mixing layer is able to grow sufficiently, it will spread through the whole depth of the lower layer. We assume that the mixing layer deepens until the gradient Richardson number is larger than 1/4 and calculate the associated entrainment and dilution of the flow as a function of the source Froude number. Motivated by experimental observations (Cenedese et al., 2016; Sher and Woods, 2017) and numerical simulations (Hogg et al., 2016; Kneller et al., 2016), as a simplification we assume that the vertical profiles of horizontal velocity and buoyancy in the downstream flow involve a linearly stratified region overlying a uniform layer below. Later in this chapter figure 3.8 also presents density and velocity data taken from a numerical simulation of a gravity current by Kneller et al. (2016). The profiles presented are consistent with our ansatz of a linearly stratified interfacial mixing layer overlying a uniform lower layer. We explore how the volume flux of the flow changes as a function of the gradient Richardson number of the stratified zone. Our results provide insight into the magnitude of dilution of dense horizontal currents, through mixing with ambient fluid, and provide a framework to help interpret predictions of mixing as derived from local models of entrainment.

In this chapter we restrict our analysis to the idealised situation in which there is a steady transition from uniform inflow to piecewise linear solutions across a finite steady adjustment zone. By assuming the idealised downstream structure of the flow we show a range of solutions that are compatible with such a steady transition; however, we make no assumptions about what form of downstream boundary conditions could have caused such a flow structure to arise. In practice, when a flow comes in from a nozzle and adjusts, there may be a steady or transient adjustment zone. Gratton and Vigo (1994) have looked at how these flows evolve, under assumption of universal structure. It is possible to envisage situations different in nature, where downstream boundary conditions do not allow for a steady finite transition zone (e.g causing a time-dependent

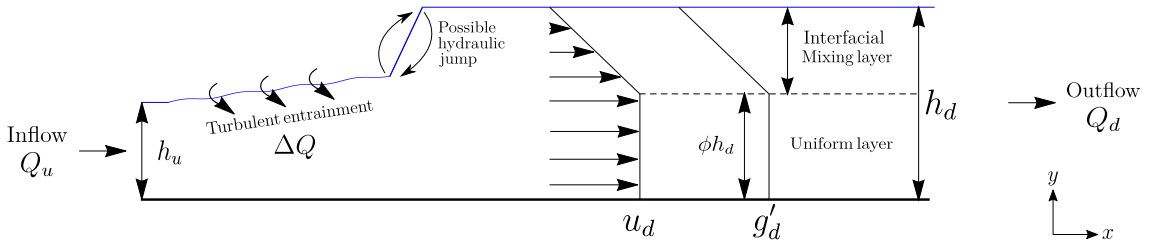

Fig. 3.1 A schematic of the system under consideration. A uniform upstream profile at $x = 0$ evolves to a hybrid uniform-linear downstream profile via turbulent entrainment through the interface and/or possibly through a hydraulic jump. The uniform flow fraction of the velocity and density profiles is given by $\phi \in [0, 1]$. The upstream volume flux is denoted Q_u and the downstream Q_d. In §3.4 we have set $\phi = 1$ such that only a uniform downstream profile is considered.

transition), and this could relate to the 'no-solution' region identified in this chapter. It would be possible, and of interest, to carry out a series of initial value problems to explore any dependency of the transition zone on downstream boundary conditions, but this is beyond the scope of this work.

We first present a general model of the mixing, and then in §3.4 present results for the reference case in which we assume the downstream flow is well-mixed and has uniform velocity and buoyancy (Johnson and Hogg, 2013). This reference case enables comparison of the mixing with that predicted by the new family of flows in which we include a linearly stratified region at the interface between the two fluids (§3.5). Furthermore, in §3.6 we consider the case of more energetic flows in which all the injected fluid becomes modified through mixing and the whole current becomes linearly stratified in buoyancy and velocity. We refer to the layer as being fully modified in this case. We conclude by discussing the implications of these models for gravity currents and other density-stratified flows.

3.3 Model

Consider a quasi-steady turbulent two-dimensional layer of fluid of depth $h(x)$, velocity $u(x, y)$ and buoyancy profile $g'(x, y)$. In this case x is the along-stream direction, and y the vertical cross-stream direction. By considering a control volume and proceeding under the assumption that the pressure in the flow is hydrostatic and constant at some height $H > h$, in the upper static layer, the conservation of vertically integrated mass, momentum, and buoyancy flux requires that

$$\frac{\partial}{\partial x}\left(\int_0^h u \, \mathrm{d}y\right) = \varepsilon u(x,h), \quad \frac{\partial}{\partial x}\left(\int_0^h u^2 + \left(\int_y^h g' \, \mathrm{d}y^*\right) \, \mathrm{d}y\right) = 0, \quad \frac{\partial}{\partial x}\left(\int_0^h u g' \, \mathrm{d}y\right) = 0. \tag{3.1a, b, c}$$

where ε is an entrainment parameter. We assume that there is a separation of scales between the horizontal distance over which the flow dissipates momentum flux through boundary friction and the horizontal distance over which the current entrains ambient fluid and distributes this through turbulent eddies. With this assumption we assume momentum flux is conserved, and that the current evolves redistributing the momentum and buoyancy as described in Turner (1979), and hence equations 3.1 provide a good description of the flow.

A generalised schematic of the system under consideration can be seen in figure 3.1. Throughout this chapter we assume the upstream flow profile is uniform in velocity and buoyancy. Although we could generalise this initial condition, it corresponds to the mixing produced in the initial phases of a flow from a uniform source and represents a simple illustration of the approach. Downstream, we allow the flow to become stratified and we assume that the buoyancy and momentum mix at the same rate, such that the depth of the velocity-stratified and buoyancy-stratified zones are the same. We assume that the fluid transitions between the upstream and downstream state via turbulent entrainment and mixing through the interface, or possibly through a hydraulic jump

from a supercritical to subcritical flow, or a combination of both. In the schematic we show an example downstream flow with a hybrid linear-uniform density and velocity structure. The parameter ϕ describes the fraction of the downstream velocity and density profile that is uniform. We define the averaged quantities

$$S_1\bar{u}h = \int_0^h u \, \mathrm{d}y, \quad S_2\bar{u}^2h + S_3\bar{g}'h^2 = \int_0^h u^2 + \left(\int_y^h g' \, \mathrm{d}y^*\right) \, \mathrm{d}y, \quad S_4\bar{u}\bar{g}'h = \int_0^h ug' \, \mathrm{d}y \tag{3.2a, b, c}$$

where $\bar{u}(x)$ and $\bar{g}'(x)$ are the depth-averaged velocity and buoyancy profiles and $h(x)$ is the depth of the current. The shape factors S_1, S_2, S_3, S_4 are defined in terms of the particular structure of the velocity and buoyancy profiles $u(x, y)$, $g'(x, y)$. From these depth-averaged quantities and the conservation laws (equations 3.1) we find that the transition from a uniform source at $x = 0$ to the flow at a downstream location $x = x_d$ can be written in terms of the shape factors at $x = x_d$ in the form

$$S_1u_dh_d - u_uh_u = \int_0^{x_d} \varepsilon u(x, h) \, \mathrm{d}x, \quad u_u^2h_u + \frac{g'_uh_u^2}{2} = S_2u_d^2h_d + S_3g'_dh_d^2, \quad u_ug'_uh_u = S_4u_dg'_dh_d, \tag{3.3a, b, c}$$

where $u_u = \bar{u}(0)$, $u_d = \bar{u}(x_d)$, $g'_u = \bar{g}'(0)$, $g'_d = \bar{g}'(x_d)$, $h_u = h(0)$, $h_d = h(x_d)$ denote the upstream and downstream velocities, buoyancies, and heights of the flow, respectively.

We now investigate the possible flow solutions given a series of simplified vertical velocity and density profiles in the downstream flow. We start with a reference model in which we assume the downstream flow is well-mixed and vertically uniform, although noting that this flow structure is unstable. Then we consider the case in which the mixing leads to a linearly stratified interfacial mixing layer above a well-mixed uniform region at the base of the flow in which buoyancy is assumed to be equal to that of the upstream flow, as shown in figure 3.1. We note that, for completeness, we have included the conservation of mass equation (3.1a leading to 3.3a) in the above model; however, the following analysis only relies on the conservation of momentum and buoyancy

equations (3.3b, c). A discussion on how the conservation of mass equation could be used to estimate an entrainment parameter is discussed in §3.7.

3.4 Uniform flow

Although Ellison and Turner (1959) originally included shape factors in their model, many subsequent models of gravity currents have assumed the current has a uniform flow profile, even when accounting for entrainment (Johnson and Hogg, 2013) or hydraulic jumps (Holland et al., 2002). For reference, we therefore derive results for a current which has a uniform flow downstream. For a uniform downstream flow the shape factors are given by $S_1 = 1$, $S_2 = 1, S_3 = 1/2$, $S_4 = 1$ (equation 3.3). However, such flows are unstable for all Froude numbers owing to the discontinuity in velocity at the interface. In §3.5, we compare these solutions with a new class of profiles in which we assume there is a mixing layer at the interface which can lead to a stable flow downstream. In reference to the schematic in figure 3.1, these uniform downstream flow solutions have $\phi = 1$. As the upstream and downstream flows are uniform the notion of upstream and downstream Froude numbers are well defined by

$$Fr_u = \frac{u_u}{\sqrt{g'_u h_u}}, \quad Fr_d = \frac{u_d}{\sqrt{g'_d h_d}}. \tag{3.4a, b}$$

We can introduce the dimensionless parameters $\hat{h} = h_d/h_u$, $\hat{g}' = g'_d/g'_u$, $\hat{u} = u_d/u_u$ and rewrite equations 3.3b, c in terms of the upstream and downstream Froude numbers

$$Fr_u = Fr_d \left(\hat{g}'\hat{h}\right)^{3/2}, \tag{3.5a}$$

$$Fr_u^2 + \frac{1}{2} = \left(Fr_d^2 + \frac{1}{2}\right)\left(\frac{Fr_u}{Fr_d}\right)^{2/3}\hat{h}. \tag{3.5b}$$

The dimensionless parameters are given explicitly by the relations

$$\hat{u} = \left(\frac{Fr_d}{Fr_u}\right)^{2/3}, \quad \hat{g}' = \frac{1+2Fr_d^2}{1+2Fr_u^2}\left(\frac{Fr_u}{Fr_d}\right)^{4/3}, \quad \hat{h} = \frac{1+2Fr_u^2}{1+2Fr_d^2}\left(\frac{Fr_d}{Fr_u}\right)^{2/3}. \quad (3.6a, b, c)$$

The dimensionless flux of entrained fluid associated with the transition from source, $x = 0$, to downstream, $x = x_d$, is the difference between the dimensionless inflow volume flux Q_u and outflow volume flux Q_d and may be expressed in the form

$$\Delta Q = \frac{Q_d - Q_u}{Q_u} = \hat{u}\hat{h} - 1. \quad (3.7)$$

Combining this expression with equations 3.6, we find

$$\Delta Q = \frac{1+2Fr_u^2}{1+2Fr_d^2}\left(\frac{Fr_d}{Fr_u}\right)^{4/3} - 1. \quad (3.8)$$

Figure 3.2*a* illustrates how the dimensionless flux of entrained fluid varies as a function of the downstream Froude number. The special case in which there is no entrainment, at $Fr_d = Fr_u$, corresponds to the case in which the flow undergoes no transition between upstream and downstream and hence remains unmodified. The other solution in which there is no entrainment has downstream Froude number $Fr_d = Fr_d^*$, and corresponds to the case in which the flow has undergone a hydraulic jump to a subcritical flow with no entrainment. This solution is given by

$$Fr_d^* = \frac{\sqrt{1+\sqrt{1+8Fr_u^2}+2Fr_u^2\left(3+\sqrt{1+8Fr_u^2}\right)}}{4Fr_u^2}. \quad (3.9)$$

For downstream Froude numbers satisfying $Fr_d^* < Fr_d < Fr_u$ we have $\Delta Q > 0$ and $\hat{g}' < 1$, implying dilution of buoyancy via entrainment. Outside of this range the model is unphysical owing to the implication of detrainment and a concentration of buoyancy.

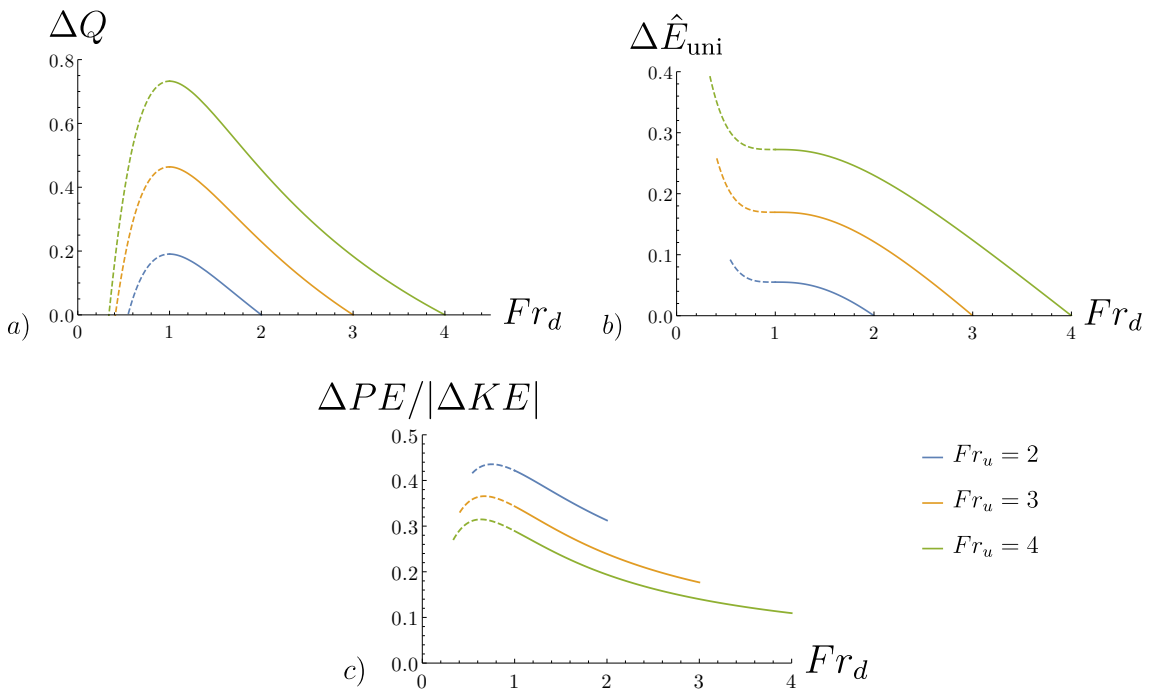

Fig. 3.2 These figures refer to the case of vertically uniform buoyancy and horizontal velocity. (a) Mixing as a function of the downstream Froude number attained by the flow. The two roots occur at $Fr_u = Fr_d$ where no transition has occurred, and $Fr_u = Fr_d^*$ the conjugate hydraulic jump solution with no entrainment. Maximal mixing occurs at downstream Froude $Fr_d = 1$. The supercritical solution branch is denoted with solid lines, and the subcritical with dashed. (b) The energy dissipation $\Delta \hat{E}_{\text{uni}}$ as a function of the downstream Froude number Fr_d for fixed upstream Froude numbers Fr_u. Note the zero dissipation solution at $Fr_u = Fr_d$ where no transition has occurred, and the maximal dissipation solution at Fr_d^*. (c) The mixing efficiency $\Delta PE/|\Delta KE|$ for a range of fixed upstream Froude numbers Fr_u.

The solution with maximal entrainment flux occurs with $Fr_d = 1$. This maximal entrainment solution has an explicit expression

$$\Delta Q_{\max} = \frac{1 + 2Fr_u^2}{3Fr_u^{4/3}} - 1. \tag{3.10}$$

In figure 3.2*a* there are a range of solutions with $Fr_d < 1$, and one may envisage that these are accessed by entrainment along the supercritical branch and then the occurrence of a hydraulic jump, which transforms the flow from the supercritical branch ($Fr > 1$) to the subcritical branch ($Fr < 1$), where Fr denotes the local Froude number of the flow.

The non-dimensional energy dissipation across the transition in the flow $\Delta\hat{E}_{\text{uni}}$ may be written as

$$\Delta\hat{E}_{\text{uni}} = \frac{Fr_u^3}{2} + Fr_u - \hat{h}\left(\hat{g}'\hat{h}\right)^{3/2}\left(\frac{Fr_d^3}{2} + Fr_d\right), \tag{3.11}$$

which is the difference in energy flux between the uniform source and downstream structured flow. Figure 3.2*b* illustrates how this quantity varies as a function of the downstream Froude number Fr_d for a fixed upstream Froude number Fr_u. The special case in which $Fr_d = Fr_u$ has zero dissipation, as the flow has undergone no modification. Furthermore, the solution with maximal dissipation corresponds to the case with $Fr_d = Fr_d^*$; in this case the flow has the maximum downstream height h_d with zero entrainment.

We can rearrange equation 3.11 such that the kinetic, potential, and internal energy flux terms before and after the transition are more easily recognised:

$$\frac{Fr_u^3}{2} + \frac{Fr_u}{2} + \frac{Fr_u}{2} = \hat{h}\left(\hat{g}'\hat{h}\right)^{3/2}\left(\frac{Fr_d^3}{2} + \frac{Fr_d}{2} + \frac{Fr_d}{2}\right) + \Delta\hat{E}_{\text{uni}}. \tag{3.12}$$

The first three terms represent the upstream kinetic energy flux, potential energy flux, and internal energy flux respectively. Similarly, the term inside the bracket on the

right-hand side represents these quantities downstream. Finally, the energy dissipated through the transition is given by the last term on the right-hand side. We can write the change in kinetic energy flux and potential energy flux through the transition as

$$\Delta KE = \hat{h}\left(\hat{g}'\hat{h}\right)^{3/2}\frac{Fr_d^3}{2} - \frac{Fr_u^3}{2}, \quad \Delta PE = \hat{h}\left(\hat{g}'\hat{h}\right)^{3/2}\frac{Fr_d}{2} - \frac{Fr_u}{2}. \qquad (3.12a, b)$$

We then define the mixing efficiency as $\Delta PE/|\Delta KE|$. Figure 3.2*c* illustrates how the efficiency varies as a function of downstream Froude number for a fixed upstream Froude number.

The downstream bulk Richardson number is given by $1/Fr_d^2$, and for the class of solutions described herein, the mixing reaches a maximum when the bulk Richardson number is 1. At this point, the Richardson number cannot evolve further, since either an increase or a decrease would require the flux to decrease, which would involve detrainment. With upstream Froude numbers smaller than 2, this implies a maximum entrainment flux $\Delta Q_{\max} \sim 0.2$. Although such solutions are appealing for their simplicity, the underlying velocity structure is unstable, owing to the discrete jump in flow properties at the interface (Turner, 1979). In practice we expect an intermediate interfacial mixing layer to develop and deepen until the gradient Richardson number of this intermediate zone increases beyond 1/4.

In §3.5 and §3.6 we present two cases. First, for an upstream flow with moderate Froude number we expect a linearly stratified intermediate mixing layer to grow to a depth $(1-\phi)h_d$, below which the uniform layer of depth ϕh_d has the same buoyancy as the original inflow g'_u. Secondly, for high Froude numbers we expect that the whole layer will become modified, such that the downstream flow is linearly stratified in velocity and buoyancy, and the buoyancy at the base of the current now falls to values smaller than the original upstream value $g'_d \leq g'_u$.

3.5 Interfacial mixing layer $Fr \leq 2.921$

3.5.1 Stratified flow solutions

The general result (equation 3.3) illustrates that the total mixing depends on the shape factors S_1 through S_4 and also the downstream gradient Richardson number. Experimental data from Ellison and Turner (1959), and more recently from Monti et al. (2007), Cenedese et al. (2016), and Sher and Woods (2017) suggest that for moderate source Froude numbers, the mixing acts to form an intermediate stratified layer, with a more uniform lower region of the flow in which the buoyancy remains close to the original buoyancy (see Sher and Woods, 2017, figure 6). This vertical structure is also in accord with numerical experiments of mixing across a shear layer (Smyth and Moum, 2012) and in steady gravity currents (Hogg et al., 2016; Kneller et al., 2016), as discussed further in §3.7.

As illustrated in figure 3.1, for the downstream flow we explore the behaviour of currents with the idealised velocity and buoyancy profiles

$$u(x_d, y) = \begin{cases} u_d \quad \text{if} \quad 0 \leq y \leq \phi h_d, \\ u_d \left(\dfrac{h_d - y}{h_d(1-\phi)} \right) \quad \text{if} \quad \phi h_d \leq y \leq h_d, \end{cases} \tag{3.13}$$

$$g'(x_d, y) = \begin{cases} g'_d \quad \text{if} \quad 0 \leq y \leq \phi h_d, \\ g'_d \left(\dfrac{h_d - y}{h_d(1-\phi)} \right) \quad \text{if} \quad \phi h_d \leq y \leq h_d, \end{cases} \tag{3.14}$$

noting now that the downstream shape factors are functions of ϕ, the fractional depth of the uniform part of the downstream flow. We also note that $g'_d = g'_u$, since the downstream uniform lower region is unmodified by mixing and so has the same buoyancy as the upstream flow. Figure 3.1 illustrates how we envisage the upstream uniform flow might evolve to a downstream flow, with a uniform lower region overlain by a linearly

stratified interfacial mixing zone, as a result of either entrainment or a hydraulic jump. Substitution of this downstream flow profile into equations 3.1 leads to the following constraints on u_d, h_d as functions of ϕ and the upstream flow u_u, g'_u and h_u

$$u_u g'_u h_u = \frac{1}{3} u_d g'_u h_d (1+2\phi), \tag{3.15a}$$

$$u_u^2 h_u + \frac{1}{2} g'_u h_u^2 = \frac{1}{3} u_d^2 h_d (1+2\phi) + \frac{1}{6} g'_u h_d^2 \left(1+\phi+\phi^2\right). \tag{3.15b}$$

Since the downstream velocity and buoyancy profiles have a hybrid uniform-linear nature, a downstream Froude number is not well defined. Instead we choose to define a downstream gradient Richardson number based on the upper linearly stratified portion of the flow

$$Ri_d = \frac{g'_d h_d (1-\phi)}{u_d^2}. \tag{3.16}$$

Rewriting equations 3.15 in terms of the dimensionless parameters $Fr_u, Ri_d, \hat{h} = h_d/h_u, \hat{u} = u_d/u_u$ gives

$$Fr_u = \frac{1}{3} \hat{h}^{3/2} \left(\frac{1-\phi}{Ri_d}\right)^{1/2} (1+2\phi), \tag{3.17a}$$

$$Fr_u^2 + \frac{1}{2} = \hat{h}^2 \left(\frac{(1-\phi)(1+2\phi)}{3Ri_d} + \frac{1+\phi+\phi^2}{6}\right). \tag{3.17b}$$

These expressions can be used to evaluate $\hat{h}(Fr_u, \phi)$, $\hat{u}(Fr_u, \phi)$ and $Ri_d(Fr_u, \phi)$.

Consideration of the dimensionless conservation laws, equations 3.17, leads to an understanding that there exists a minimal ϕ for each upstream Froude number Fr_u, and this minimum decreases as Fr_u increases. If the upstream Froude number is too small, the momentum of the flow may not be sufficient to mix the current with large volumes of the ambient fluid, and this limits the possible range of ϕ values downstream. From equations 3.17 we can determine a cubic expression for $\hat{h}$. By considering extrema

of $\hat{h}$ in ϕ space and determining when they satisfy physical bounds (eg. $\phi \in [0, 1]$) we can determine that the smallest ϕ which may be accessed by an upstream Froude number, which we denote as $\phi_{\min}$, can be expressed as

$$\phi_{\min} = \frac{1}{2}\left(\frac{9\sqrt{3}Fr_u^2}{\sqrt{4 + 24Fr_u^2 - 33Fr_u^4 + 32Fr_u^6}} - 1\right). \tag{3.18}$$

For $0 \leq \phi \leq \phi_{\min}$ solutions are not possible as they violate mass and momentum conservation. The region $\phi \leq \phi_{\min}$ is illustrated by the shaded blue region of the regime diagram in figure 3.3*a*. The roots of equation 3.18 require that $0.417 \leq Fr_u \leq 2.921$, otherwise the model predicts $\phi < 0$, which is unphysical. Outside of this range, the flow has sufficient momentum (or equivalently small enough buoyancy) that all the fluid in the current can become modified through mixing, and in §3.6 we present a further series of solutions for that case.

Furthermore, we note that the equations for the conservation of buoyancy and momentum lead to an equation which is cubic in nature with three real roots. One of these roots is unphysical since it requires $h_d < 0$. However, the two remaining roots may be interpreted physically. One root, which we will denote supercritical by analogy with §3.4, can be thought of as evolving continuously away from the upstream uniform flow by turbulent entrainment. The entrainment gradually erodes the interface, creating a deepening interfacial mixing layer. The other root, which we will denote subcritical, can be interpreted as the case in which the fluid undergoes a discontinuous hydraulic jump to a conjugate flow state where the local Froude number < 1. This could possibly occur after a period of supercritical interfacial entrainment.

We can also determine which of the family of solutions that are consistent with momentum and buoyancy conservation are stable. This is done by determining those solutions for which the gradient Richardson number $Ri_d \geq 0.25$ for both supercritical and subcritical branches. The case for which both supercritical and subcritical branches

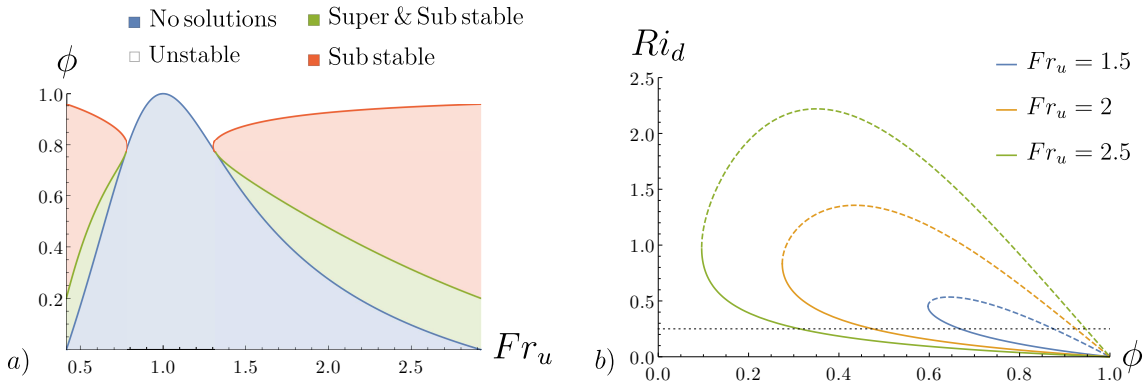

Fig. 3.3 These figures refer to the case with a lower uniform region overlain by an interfacial linearly stratified mixing region. (a) A regime diagram illustrating the nature of solutions for an upstream Froude number Fr_u and downstream uniform flow fraction ϕ. Blue shaded areas are regions of no solution due to violation of conservation laws. Green shaded areas are where $Ri_d \geq 1/4$ and the downstream flow is stable for both supercritical and subcritical solutions. Red shaded areas are stable for subcritical solutions and unstable for supercritical solutions. White areas are where $Ri_d < 1/4$ and the downstream flow is unstable for all solutions. (b) The variation of downstream gradient Richardson number with uniform flow fraction ϕ. Supercritical solutions are shown in solid line and subcritical in a dashed line. The two solution branches converge when $\phi = \phi_{\min}$ at $Ri_d(\phi_{\min})$. The turning point of the subcritical branch gives a maximal downstream gradient Richardson number $Ri_{d_{\max}}$ for each upstream Froude number Fr_u. Portions of both branches below the black dotted line $Ri_d = 1/4$ are unstable.

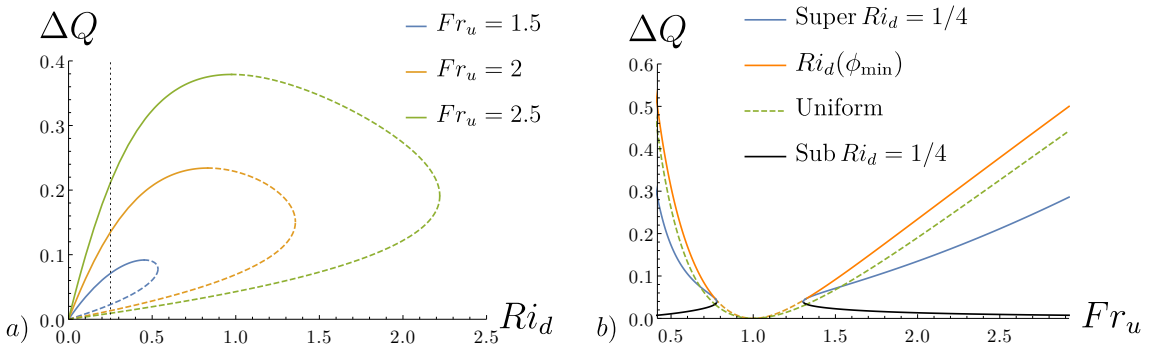

Fig. 3.4 These figures refer to the case with a lower uniform region overlain by an interfacial linearly stratified mixing region. (a) Dimensionless entrainment flux as a function of the downstream gradient Richardson number for a fixed upstream Froude number Fr_u. Supercritical branch solutions are shown with solid lines and subcritical in dashed. Maximal entrainment occurs at the convergence of the two branches $\phi_{\min}$. Points of the curve left of the line $Ri_d = 1/4$ are unstable. (b) The downstream dimensionless entrainment flux ΔQ as a function of upstream inflow Froude number Fr_u for $Ri_d(\phi_{\min})$ in orange, the supercritical solution branch with gradient Richardson number $Ri_d = 1/4$ in blue, the subcritical solution branch with gradient Richardson number $Ri_d = 1/4$ in black, and the uniform downstream calculation of §3.4 in green. The dashed portion of the curves illustrate where the downstream flow is unstable.

are stable is shaded green in figure 3.3a. The red shaded area indicates where only the subcritical solution branch is stable and the supercritical unstable. We note that transition to a uniform flow downstream ($\phi = 1$) is always unstable in that the gradient Richardson number tends to zero as the mixed layer thickness tends to zero, with a non-zero jump in density and velocity across the layer.

In figure 3.3b we illustrate the variation of the downstream gradient Richardson number Ri_d as a function of the fractional depth of the well-mixed lower region of the flow ϕ for a series of upstream Froude numbers Fr_u. The supercritical branch, denoted with solid lines, converges to the subcritical solution branch, denoted with dashed lines, at the value $Ri_d(Fr_u, \phi_{\min})$. The dotted black line indicates $Ri_d = 1/4$ below which all downstream flows are unstable.

3.5.2 Entrainment

We can express the dimensionless flux of entrained ambient fluid associated with the transition from the upstream uniform flow to the downstream structured flow in terms of the expression

$$\Delta Q = \frac{\hat{u}\hat{h}(1+\phi)}{2} - 1 = \frac{1-\phi}{2(1+2\phi)}. \tag{3.19}$$

In figure 3.4*a* we plot the variation of the dimensionless entrainment flux ΔQ as a function of the downstream gradient Richardson number, for three fixed values of the upstream Froude number Fr_u. We note that flows with downstream gradient Richardson number $Ri_d \geq 1/4$ are stable to downstream disturbances of any wavenumber (Turner, 1979); and for portions of the curve with $Ri_d < 1/4$ the solutions are unstable. Solutions from the supercritical branch are denoted with solid lines, and solutions from the subcritical branch are denoted with dashed lines. The maximal mixing solution occurs at the convergence of the two branches, with the gradient Richardson number associated with $\phi_{\min}$.

In figure 3.4*b* we compare the flux of entrained fluid predicted for the reference solutions in which we assume the flow downstream is uniform (dashed green line; see §3.4 equation 3.10) and that predicted by the solutions which have a linearly stratified mixed layer downstream. Curves are shown for the solutions in which: (i) the supercritical branch's gradient Richardson number is $Ri_d = 0.25$ (blue line), (ii) the subcritical branch has $Ri_d = 1/4$ (black line), and (iii) for the solutions which have the maximal mixing and $Ri_d(\phi_{\min})$ (orange line). The dashed portions of the orange line illustrate where the gradient Richardson number of the downstream flow with maximal mixing is unstable (ie. $Ri_d(\phi_{\min}) < 0.25$). It is seen that the model in which we assume the flow is uniform downstream (§3.4) leads to less mixing than the stratified flow solutions with largest possible downstream gradient Richardson number. However, we can also see that stratified flows with $Ri_d = 1/4$ have smaller total flux of

entrained fluid than these reference uniform flow solutions. Furthermore, the amount of fluid entrained by the subcritical branch with $Ri_d = 1/4$ is less than the supercritical branch. The model also shows that there is a region $0.770 \leq Fr_u \leq 1.319$ where no downstream flows are stable.

3.5.3 Energetics - supercritical and subcritical branches

A clear way to illustrate the difference between the two solution branches is to consider the energy dissipation $\Delta E(Fr_u, \phi)$ across the transition. The steady energy flux lost per unit distance through the transition is given by

$$\frac{\partial}{\partial x}\left(\int_0^h u\left(\frac{u^2}{2} + g'y\right)\,\mathrm{d}y + \int_0^h u\left(\int_y^h g'\,\mathrm{d}y^*\right)\mathrm{d}y\right) = \frac{\partial(\Delta E)}{\partial x}, \tag{3.20}$$

where the first term inside the differential corresponds to the flux of specific energy (kinetic and potential) and second term corresponds to the flux of the vertical integral of hydrostatic pressure (internal energy). Substituting the model solution allows us to write the dissipation as

$$\Delta\hat{E} = \frac{Fr_u^3}{2} + Fr_u - \frac{\hat{h}^{5/2}}{24}\left(\frac{1-\phi}{Ri_d}\right)^{1/2}\left(\frac{3(1-\phi)(1+3\phi)}{Ri_d} + 5 + 10\phi + 9\phi^2\right), \tag{3.21}$$

where $\Delta\hat{E} = \Delta E / g_u'^{3/2} h_u^{5/2}$. As was noted in §3.4, for a uniform flow, there are two conjugate solutions with no mixing, by analogy with classical hydraulics. We expect a similar result in the present case. The first solution with zero entrainment corresponds to the solution where no transition occurs, and has $\Delta E = 0$. Whilst the conjugate zero-entrainment solution, involving a hydraulic jump, has a finite dissipation when $\phi = 1$ (in equivalence with figure 3.2*b*). For a fixed source Froude number $Fr_u = 2$, figure 3.5*a* illustrates the energy dissipation as ϕ varies. On the supercritical branch the dissipation is 0 at $\phi = 1$. As ϕ is then decreased, which corresponds to an increase

in the thickness of the stratified zone, a finite amount of energy is dissipated. However, even when $\phi = 1$, the energy dissipation on the subcritical branch is finite. As ϕ then decreases, corresponding to progressively more mixing, the energy dissipation increases to a maximum value of 0.096 when $\phi = 0.484$, which corresponds to a gradient Richardson number $Ri_d = 1.337$. The energy dissipation then falls as the solution converges towards the supercritical branch with $\phi_{\min} = 0.275$. It is unphysical for the dissipation to fall via the process of entrainment, so solutions along the subcritical branch are restricted to values of $\phi > 0.484$. Solutions in the range $\phi_{\min} < \phi < 0.484$ may be accessed through a discontinuous hydraulic jump from the supercritical branch.

In figure 3.5*b* we show how the non-dimensional downstream height $\hat{h}$ varies as a function of the downstream gradient Richardson number Ri_d for both supercritical and subcritical solution branches. In this figure we can see that the supercritical branch moves continuously away from 1 by the process of interfacial entrainment, which deepens the interfacial mixing zone and increases the gradient Richardson number to the value at $Ri_d(\phi_{\min})$. However for subcritical solutions the discontinuous nature of the change in height can be seen, with the special zero-entrainment case jumping to a height $\hat{h} = 2.375$. Entrainment can then continuously occur along the subcritical solution branch until $Ri_d = 1.337$ is reached and the maximal energy has been dissipated. Other heights could be reached beyond this value but via a discontinuous process after which evolution would be restricted in order that the energy continues to dissipate through mixing.

3.6 Fully modified layer $Fr > 2.921$

For flows where the upstream Froude number $Fr_u = 2.921$, the entire flow can become linearly stratified with $\phi = 0$, and the buoyancy at the base just equal to the initial buoyancy upstream. For upstream Froude numbers larger than this critical value,

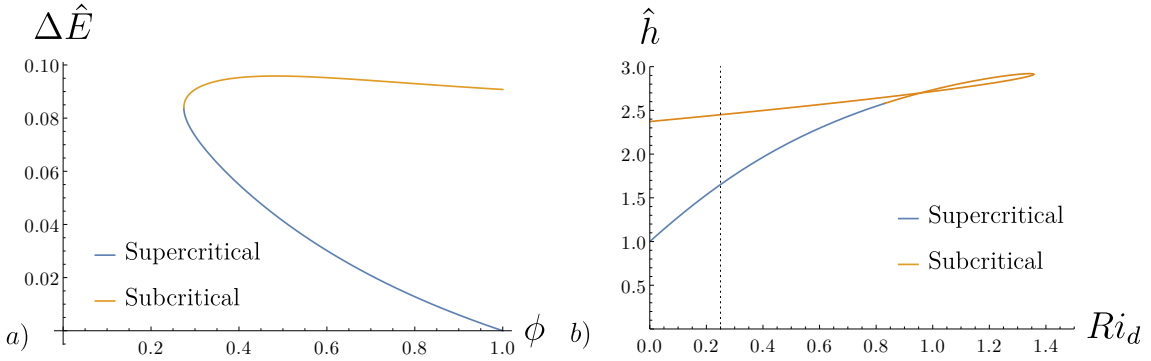

Fig. 3.5 These figures refer to the case with a lower uniform region overlain by an interfacial linearly stratified mixing region. (a) The variation of dimensionless energy dissipation $\Delta\hat{E}$ with the downstream uniform flow fraction ϕ for a fixed upstream Froude number $Fr_u = 2$. The blue line corresponds to the supercritical branch, which continuously moves away from the $\phi = 1$ solution where no transition occurs. The orange line corresponds to the subcritical branch, which has finite dissipation at $\phi = 1$ corresponding to a hydraulic jump with no entrainment. This discontinuous transition can then dissipate more energy as a shear layer is created by the entrainment of fluid up to a maximum value $\Delta\hat{E} = 0.096$. (b) The variation of dimensionless downstream height $\hat{h}$ with downstream gradient Richardson number Ri_d for a fixed upstream Froude number $Fr_u = 2$. Solutions to the left of the black dotted line $Ri_d = 1/4$ are unstable.

further mixing may arise, and this can lead to further dilution of the flow, with the buoyancy at the base of the current g'_d falling below the original value of the upstream flow g'_u. Now, in this case, the downstream velocity and buoyancy profiles have the form

$$u(x_d, y) = \frac{u_d(h_d - y)}{h_d}, \quad g'(x_d, y) = \frac{g'_d(h_d - y)}{h_d}. \tag{3.22a, b}$$

By substituting into equations 3.2 we find the shape factors $S_1 = 1/2$, $S_3 = 1/6$, $S_2 = S_4 = 1/3$ and the following (dimensional) relation with the uniform flow at the source $x = 0$

$$u_u g'_u h_u = \frac{1}{3} u_d g'_d h_d, \tag{3.23a}$$

$$u_u^2 h_u + \frac{1}{2} g'_u h_u^2 = \frac{1}{3} u_d^2 h_d + \frac{1}{6} g'_d h_d^2. \tag{3.23b}$$

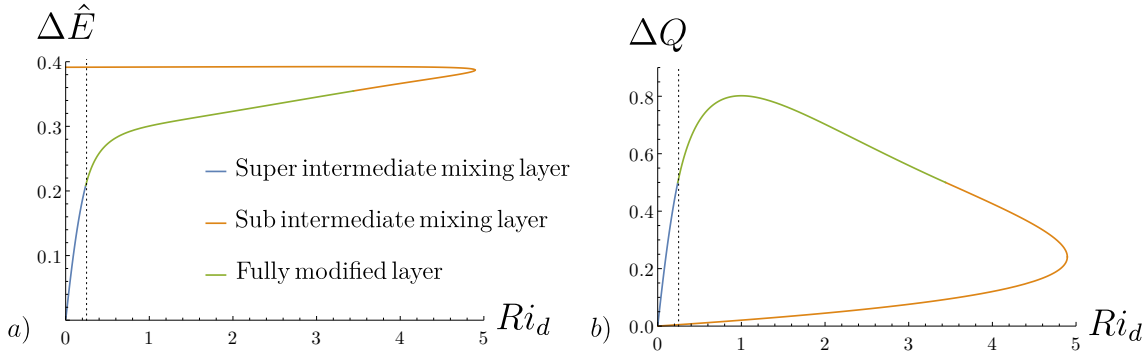

Fig. 3.6 These figures refer to the case when the flow is fully modified and is linearly stratified throughout. (a) A diagram illustrating the variation of dimensionless energy dissipation $\Delta\hat{E}$ with downstream gradient Richardson number Ri_d for a fixed upstream Froude number $Fr_u = 4$. The orange curve represents solutions from the subcritical interfacial mixing layer model, the blue curve solutions from the supercritical interfacial mixing layer model, and the green curve represents solutions from the fully modified layer model. Solutions to the left of the black dotted line $Ri_d = 1/4$ are unstable. (b) The downstream entrainment flux ΔQ as a function of downstream gradient Richardson number Ri_d for a fixed upstream inflow Froude number $Fr_u = 4$. The orange curve illustrates solutions from the subcritical interfacial mixing layer model, the blue curve solutions from the super critical interfacial mixing layer model, and the green curve solutions from the fully modified layer model. Note, solutions to the left of the line $Ri_d = 1/4$ are unstable.

We can rewrite equation 3.23 in terms of the dimensionless parameters $Ri_d = g'_d h_d/u_d^2$, Fr_u, $\hat{u} = u_d/u_u$, $\hat{g}' = g'_d/g'_u$ and $\hat{h} = h_d/h_u$ as

$$Fr_u = \frac{\left(\hat{g}'\hat{h}\right)^{3/2}}{3Ri_d^{1/2}}, \tag{3.24a}$$

$$Fr_u^2 + \frac{1}{2} = \frac{\hat{g}'\hat{h}^2}{3}\left(\frac{1}{Ri_d} + \frac{1}{2}\right), \tag{3.24b}$$

which we can solve to determine

$$\hat{u} = \frac{3^{1/3}}{Fr_u^{2/3}Ri_d^{1/3}}, \quad \hat{g}' = \frac{3^{1/3}Fr_u^{4/3}(Ri_d+2)}{(2Fr_u^2+1)Ri_d^{1/3}}, \quad \hat{h} = \frac{3^{1/3}(2Fr_u^2+1)Ri_d^{2/3}}{Fr_u^{2/3}(Ri_d+2)}. \tag{3.25a, b, c}$$

The dimensionless entrainment flux in this case is given by

$$\Delta Q = \frac{3^{2/3}(1+2Fr_u^2)Ri_d^{1/3}}{2Fr_u^{4/3}(Ri_d+2)} - 1. \tag{3.26}$$

In figure 3.6*b* we have plotted the mixing associated with downstream gradient Richardson number Ri_d. The maximal mixing in this case occurs at $Ri_d = 1$, which is given by

$$\Delta Q_{\max} = \frac{1+2Fr_u^2}{24^{1/3}Fr_u^{4/3}} - 1. \tag{3.27}$$

Similarly, the energy dissipation due to a transition to an entirely linearly stratified state is given by substituting the model equation 3.22 into equation 3.20, then expressing the result in dimensionless form we obtain

$$\Delta\hat{E} = \frac{Fr_u^3}{2} + Fr_u - \frac{\hat{g}^{3/2}\hat{h}^{5/2}}{24}\left(\frac{3}{Ri_d^{3/2}} + \frac{5}{Ri_d^{1/2}}\right). \tag{3.28}$$

The smallest value of g'_d that the flow can attain is given by

$$g'_{d_{\min}} = \frac{81^{1/3} Fr_u^{4/3}}{1 + 2Fr_u^2}. \tag{3.29}$$

Any buoyancy g'_d at the base of the downstream flow smaller than this value violates conservation of momentum and buoyancy. The range of validity for solutions with the entire layer fully modified $Fr_u > 2.921$ is complementary to the range of validity for the solutions with an interfacial mixing layer overlying a uniform layer as given in §3.5. Theoretically, in the case $0.471 \leq Fr_u \leq 2.921$, one can find a solution with $\phi = 0$ for which $g'_d > g'_u$; however, this is unphysical since the fluid cannot become more concentrated as it migrates downstream.

To illustrate the complementary nature of the two regimes $0.471 \leq Fr_u \leq 2.921$ (interfacial mixing layer) and $Fr_u > 2.921$ (fully modified), we fix an upstream Froude number $Fr_u = 4$. From the intermediate interfacial mixing layer model we have that $0 \leq \phi \leq 1$ for $0 \leq Ri_d \leq 0.240$ on the supercritical branch. Similarly, for the subcritical branch we have two values of ϕ for gradient Richardson number in the range $3.439 \leq Ri_d \leq Ri_{d_{\max}}$ and a single value of ϕ for the range $0 \leq Ri_d \leq 3.439$. For the fully modified layer model, the range $0.240 \leq Ri_d \leq 3.493$ gives $\hat{g}' \leq 1$, and outside of this range the solution requires the unphysical case $\hat{g}' > 1$. Hence, we can see in figure 3.6a, b how the energy dissipation $\hat{E}$ and entrainment flux ΔQ vary as a function of the downstream gradient Richardson number. Since the Froude number is larger than the critical value 2.921, the convergence of the two solution branches is broken and the subcritical and supercritical branches are separated in gradient Richardson number space. However, by allowing the buoyancy at base of the flow to decrease from its initial value, the model solutions in which the current is fully stratified continuously join these distinct branches.

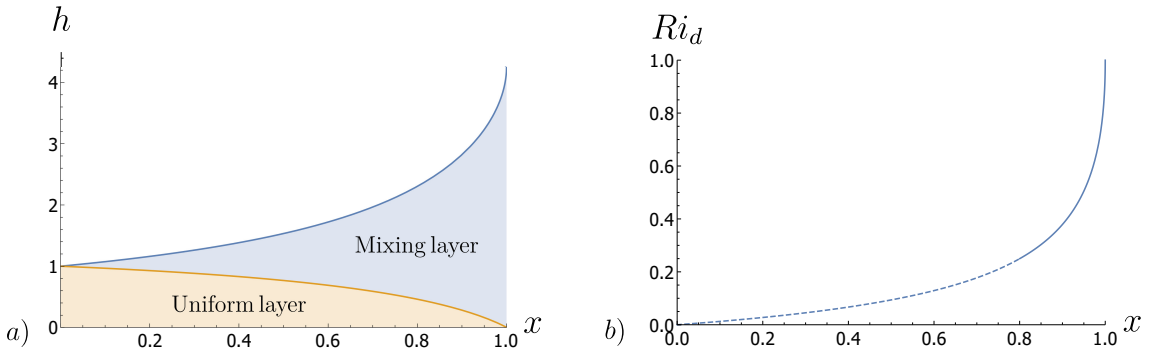

Fig. 3.7 (a) The space-like evolution of the supercritical solution branch's interfacial mixing layer in blue, and the uniform layer in orange, for the critical upstream Froude number $Fr = 2.921$. (b) The evolution of the downstream gradient Richardson number in space. The dashed line illustrates where the curve is unstable, and a solid line where the curve is stable. For convenience, in both figures the length scale is chosen such that the spacelike co-ordinate x varies between 0 and 1. This corresponds to a theoretical constant entrainment coefficient $\varepsilon_0 \approx 0.52$ from equation 3.3a.

3.7 Discussion

In this chapter we have explored the mixing which occurs when an initially uniform and dense fluid flows along a horizontal boundary beneath a second fluid of smaller density. We use an ansatz for the structure of the downstream flow which includes a region of uniform shear with a linear density gradient above a region of uniform flow and density, and constrain the properties of this flow using the conservation of momentum and buoyancy. When the stratified zone has a gradient Richardson number in excess of 1/4, the flow is stable, and we show that the volume of entrained ambient fluid in this flow increases with the upstream Froude number. We also calculate the solution which has the maximum entrainment of ambient fluid, which again has an increasing entrainment flux with upstream Froude number. For upstream Froude numbers in excess of 2.921 the stratified zone may extend to the lower boundary of the domain, so that there is no uniform region of flow.

In figure 3.7a, we illustrate the variation of the depth of the supercritical solution and of the stratified zone for a flow which has an upstream Froude number of 2.921.

In figure 3.7b, we illustrate the gradient Richardson number corresponding to each of these downstream solutions. Those solutions for which $Ri_d > 1/4$ are stable and shown with a solid line. Using equation 3.3a we can calculate an adjustment length scale as a function of ε. Figure 3.7a, b illustrate the shape of the transition zone with x, which for convenience has been scaled to vary from 0 to 1. This corresponds to a theoretical constant entrainment coefficient $\varepsilon_0 \approx 0.52$. If the actual entrainment coefficient is ε the adjustment length is given by $L \sim \varepsilon_0/\varepsilon$.

We now compare the predictions of our model with the numerical simulations of gravity currents as reported by Kneller et al. (2016). For example, in figure 3.8 we present density and velocity data taken from figure 2a of Kneller et al. (2016). This data corresponds to a gravity current travelling along a horizontal bottom boundary. Note, in their calculation the buoyancy is associated with dense particles, which are assumed to have zero settling velocity, and hence their simulation is equivalent to a saline gravity current as explored in this chapter. However, in their simulation the effect of momentum loss due bottom friction is included. To make our results directly comparable to that of Kneller et al. (2016) we need to account for the momentum loss not captured by our inviscid approximation. To do this we use the momentum flux, as calculated from the transect of velocity and density profiles in the numerical data figure 3.8, to define an equivalent inlet condition for our model. In this case our model current, which conserves momentum, has value $Fr_u = 0.67$. This is smaller than the source Froude number quoted by Kneller et al. (2016) of $Fr = 0.78$. In figure 3.8 we overlay the predictions of our model with the numerical data setting $Fr_u = 0.67$ for momentum conservation and choosing $\phi = 0.75$ as a best fit. This implies a stable gradient Richardson number $Ri_d = 0.59$ in the interfacial mixing layer. We do note that the small discrepancies at the two ends of the linearly stratified upper portion arise from the action of diffusion in the TURBINS code used by Kneller et al. (2016).

We have also analysed some further numerical simulations presented in figure $7d, e, f$ of Hogg et al. (2016). We find that the vertical density profiles at a distance 10 units behind the head in each of their figures can also be accurately represented by a linearly stratified layer overlying a more uniform layer, which is consistent with our ansatz.

It is also of interest to note that our model predicts that the flow entrains a volume flux between 0.1 - 0.5 of the source flux with upstream Froude numbers in the range 1.5 - 3 (figure 3.4*b*). The exact entrainment rate depends on the downstream gradient Richardson number of the flow. These predictions are similar in magnitude to the recent experimental data reported by Sher and Woods (2017), who found the entrainment flux into a horizontal dense jet entering a channel of less dense fluid was in the range 0.34 - 0.63 for a comparable range of upstream Froude numbers; although we note that the velocity and buoyancy profiles they report were somewhat more complex than the idealised model presented herein. The present calculations illustrate how important the inflow mixing zone may be in the development of stratification and establishment of a flow with a gradient Richardson number greater than 1/4 as a turbulent gravity current develops. This can have very significant implications for the subsequent entrainment of ambient into such a current.

As well as the continuous erosion of the interface of a supercritical flow, a hydraulic jump may lead to a subcritical flow downstream, beyond which the evolution may continue through gradual erosion and mixing across the interface. A hydraulic jump may involve a discontinuous jump to any of the possible downstream gradient Richardson numbers; however, the subsequent erosion of the interface after a jump is restricted to the maximum dissipation solution in order that the overall energy of the flow does not increase downstream, which would be unphysical.

A key feature of the model solutions is that the gradient Richardson number is restricted to values in excess of 1/4, so that the downstream flows are stable. This

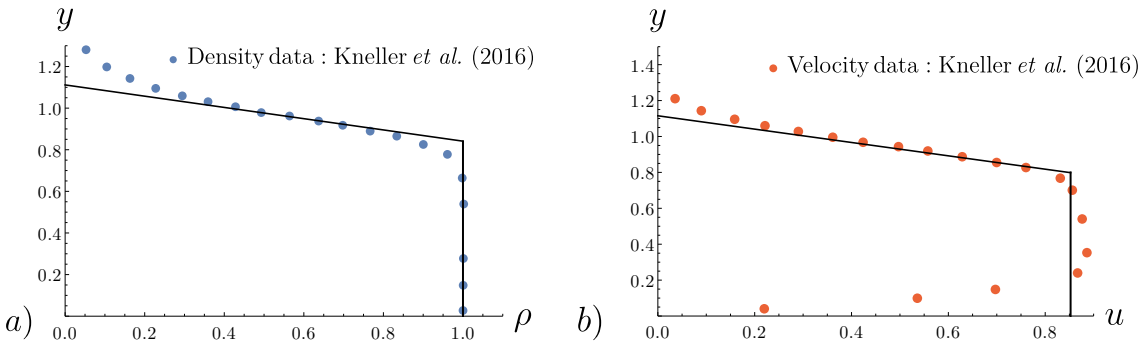

Fig. 3.8 (a) Density profile data from the numerical simulation of a gravity current on a horizontal boundary presented by Kneller et al. (2016). The black line overlain shows the profile as calculated by the model in §3.5 for an upstream Froude number $Fr_u = 0.67$. (b) Velocity profile data, again taken from Kneller et al. (2016). We note that this Froude number, $Fr_u = 0.67$, corresponds to the flow which conserves momentum flux, and has a momentum flux equal to the downstream momentum flux as calculated from the data presented by Kneller et al. (2016) and shown in panels a) and b) above. The numerical solutions of Kneller et al. (2016) include some bottom drag, and therefore lose some momentum, so that source Froude number in their calculations is in fact $Fr = 0.78$.

restriction, coupled with the ansatz of a linear stratification, leads to the prediction of less mixing than is possible if the downstream flow has vertically uniform velocity and buoyancy. This suggests that the structure of the flow is key in constraining the mixing. In depth-averaged models, this structure is expressed in terms of shape factors: the present solutions correspond to the family of such solutions in which the vertical structure of the flow involves an interfacial mixing zone with linear stratification and a lower uniform region, in which the buoyancy corresponds to the original buoyancy of the upstream flow.

The present analysis, although simplified, identifies the importance of constraining the structure and mixing in such flows, with either new laboratory experiments and direct numerical solutions. Nonetheless, even with the idealised structure of the flow, the present study provides insight and some constraints on the process of mixing as a steady gravity current becomes established downstream of a source of dense fluid.

Chapter 4

Entrainment in two-dimensional inclined gravity currents

4.1 Abstract

Dense turbulent gravity currents flowing down a slope of fixed angle θ entrain and mix ambient fluid. The continual release of potential energy as the current flows downslope powers the mixing and dilution of the dense current. We present a series of new numerical experiments modelling constant flux two-dimensional gravity currents for a range of slope angles $5^\circ < \theta < 30^\circ$. In each case, we find that after an adjustment phase the currents reach an approximately self-similar state. For each of these self-similar currents, the entrainment coefficient E is proportional to the slope angle and increases from approximately 0.01 to 0.1 as the slope angle increases from 5° to 30°. By expressing the local buoyancy and momentum fluxes as the sum of a time-averaged and fluctuating component, we find that the time-dependent turbulent fluctuations transport around 10% of the buoyancy flux per unit width and 15% of the momentum flux per unit width. The gradient Richardson number of the self-similar flow, based on the time-averaged and depth averaged properties, has value ≈ 0.25 for all slopes

considered. We consider a simplified time-averaged model, based on linear velocity and buoyancy profiles, and find an explicit formula for E that depends on integrated buoyancy profile constants and gradient Richardson number. The model is compared to the simulation data with reasonable agreement.

4.2 Introduction

Turbulent gravity currents, driven by buoyancy forces and generated by density differences between fluids, are a pervasive natural and man-made phenomenon (Simpson, 1997). Examples include the intrusion of salt water into fresh within estuaries, the motion of an avalanche down a mountainside, or the leak of dense fluid in an industrial accident. Since these flows are driven by buoyancy forces, mixing of ambient fluid into the current can play a major role in the dynamics and transport properties.

Early experimental work by Ellison and Turner (1959) estimated the amount of entrainment and mixing that occurs in gravity driven flows along an inclined boundary. They measured the cross-slope density and velocity profiles at several points along-slope by using a conductivity probe and tracing streaks of dye. Hallworth et al. (1993) introduced a novel visualisation technique for the mixing by exploiting variations in pH between the ambient and dense current. More recent experimental work by Sher and Woods (2015, 2017) and Samasiri and Woods (2015) has demonstrated that most entrainment in gravity currents running along a horizontal boundary occurs through the head of the current or, in a steady flow, near the source. In a steady horizontal current, measurements suggest there is little mixing through the upper surface of the continuing flow (Sher and Woods, 2017). Taking an analytical approach Johnson and Hogg (2013) developed similarity solutions describing the flow, assuming that there is a slow entrainment process across the upper surface of the current. This process

was based on a parametrised model in which the local Froude number of the flow is assumed to control the mixing.

Outside the laboratory, advances have been made by making use of numerical simulations. Using Large Eddy Simulation models Ottolenghi et al. (2016) studied the effect of domain aspect ratio and the magnitude of density differences on the mixing. Kneller et al. (2016) simulated turbidity currents, where the buoyancy forces arise from suspended particulates, highlighting the importance of stratification on entrainment, and van Reeuwijk et al. (2017) present several numerical experiments of a wall jet and gravity current flowing down an incline.

Of particular interest is the case when the slope is inclined. This is particularly applicable to the study of atmospheric flows where terrain is not flat, for example avalanches (Britter and Linden, 1980) and turbidity currents. Ellison and Turner (1959) first studied the relationship between slope angle and entrainment, noting that the entrainment is proportional to the slope angle. Turner (1979) also noted that as the current flows down a fixed slope after some time it reaches a so-called 'equilibrium' or 'normal' state.

Since the pioneering effort of Ellison and Turner (1959), many subsequent works have sought to explore and parametrise the mixing and entrainment in such flows. Turner (1986) gave an empirical formula for E based on his earlier experimental work. More recently, Cenedese and Adduce (2010) refined this empirical parametrisation through comparison with a wide series of field and experimental data.

In this chapter we present a series of new numerical simulations of two dimensional gravity currents on an inclined horizontal boundary. In §4.3 we outline the details of the simulation process, including the definitions of the domain of interest and simulation parameters. In §4.4 we take a closer look at two particular experiments, and describe our qualitative and quantitative observations. We extend the quantitative analysis

to the whole experimental data set in §4.5, presenting new data on the entrainment coefficient of such flows and discussing the partitioning of flow between the mean and time-dependent fluctuations. In §4.6 we present an estimate for the drag on the lower boundary.

4.3 Simulation details

The aim of the numerical experiments is to observe the evolution of steady-state two-dimensional gravity currents migrating down a long inclined boundary as a result of a continuous supply of buoyant fluid. A schematic of the geometry of the flow is shown in figure 4.1*a*. The numerical model used to solve the system of interest is a direct numerical simulation code TURBINS, as described in Nasr-Azadani and Meiburg (2011), which solves the Navier-Stokes equations, under a Boussinesq approximation, with an immersed boundary method for dealing with complex topography.

The numerical domain is set to have height $H = 100h_0$ and length $L = 100h_0$, where h_0 is the unit of length and corresponds to the depth of the input source nozzle. The source fluid is injected horizontally into the domain directly above the lower boundary at $x = 0$, $y = 0$ with a height h_0. The lower inclined boundary is solid, with a no-slip condition for the velocity field and a no-flux condition for the buoyancy field. The upper rigid lid has a no-flux condition for both the velocity and buoyancy fields. Similarly, the left-hand region above the inflow nozzle at $x = 0$ has a no-flux condition for buoyancy and velocity. As described in Nasr-Azadani and Meiburg (2011) a convective boundary condition is imposed at the far end of the domain $L = 100h_0$. This convective boundary condition allows for the inflow of ambient fluid from outside the domain to match the ambient fluid entrained by the current as it moves along the lower boundary. This ambient flow corresponds to a slow nearly uniform inflow across the far end of the domain in the region above the current. The boundary condition

also allows for the outflow of the dense current from the domain. To illustrate this, a diagram of the typical time-averaged streamlines can be seen in figure 4.1*b*. The source fluid is assigned a concentration $c_0 = 1$ and the ambient fluid has concentration $c_0 = 0$.

The dense fluid is injected into the domain with source buoyancy flux per unit width B_0 and source momentum flux M_0 per unit width. In the remainder of this chapter, for brevity, we drop 'per unit width' when making reference to momentum and buoyancy fluxes. The source velocity has a maximal value $u_0 = \sqrt{g'h_0}$, where g' is the buoyancy associated with the source fluid concentration $c_0 = 1$. The unit of time in the simulation, $t = h_0/u_0$, corresponds to the time taken for the current to advance a distance equal to the depth of the source nozzle. In each experiment the Reynolds number is set to be $Re = 10000$, so that the flow is highly turbulent and viscous effects are small. Similarly, the Peclet number is set at $Pe = 2000$ such that the advective transport dominates molecular diffusion. The numerical grid has a resolution of 1000×1000 pixels, and the model predictions were tested for numerical convergence by performing a small number of simulations at lower resolutions. The domain is chosen to be sufficiently large such that the evolution of the current is not influenced by far boundary effects.

In each simulation, we are interested in the steady state current, once the nose has passed. For convenience, we assume that at time $t = -300$ the dense fluid begins to be injected into the domain. We then begin recording data at $t = 0$, after which the transient head of the gravity current has left the domain and the flow within the domain becomes the quasi-steady body of the gravity current. We record data until $t = 1000$ so that we can capture time-averaged statistics.

We conduct a series of five experiments, varying the angle which the lower boundary is inclined to the horizontal. The angles are given by $\theta = 5.71°, 11.31°, 16.70°, 21.80°, 26.57°$ and $30.96°$. Owing to the inclined nature of the flow, we work with downslope and

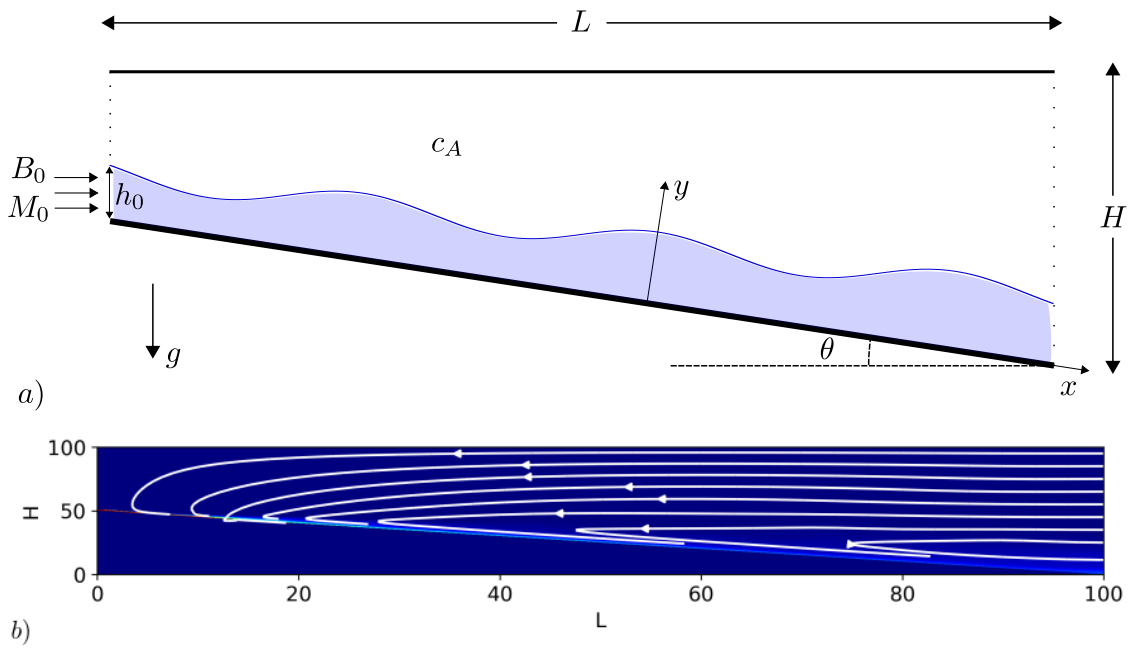

Fig. 4.1 (a) A schematic of the simulation set up. Dense fluid of height $h_0 = 1$ is injected into the domain with buoyancy flux B_0 and momentum flux M_0. The dense fluid flows downslope, until the head has left the domain, and the body of the current remains. The height of the domain is $H = 100$ and $L = 100$. The angle inclined to the horizontal is varied with $\theta = 5.71°, 11.31°, 16.70°, 21.80°, 26.57°$ and $30.96°$.(b) Streamlines for the time-averaged velocity field with $\theta = 26.57°$ overlain with the time-averaged concentration field.

cross-slope co-ordinates x, y inside the domain. TURBINS outputs data in a rectilinear geometry, so a simple trigonometrical conversion is performed to convert the data.

4.4 Experimental observations

In this section we discuss the results of two experiments, a low angle case $\theta = 5.71°$ and a high angle case $\theta = 26.57°$. We wait for the head to leave the domain so that our data is restricted to the quasi-steady body of the gravity current, which is the main interest in this study. After 300 units of time, the head has left the domain and we begin analysing data. The mixing associated with the transient head of gravity current has been studied by Britter and Linden (1980). Two snapshots in time, at $t = 0$ and

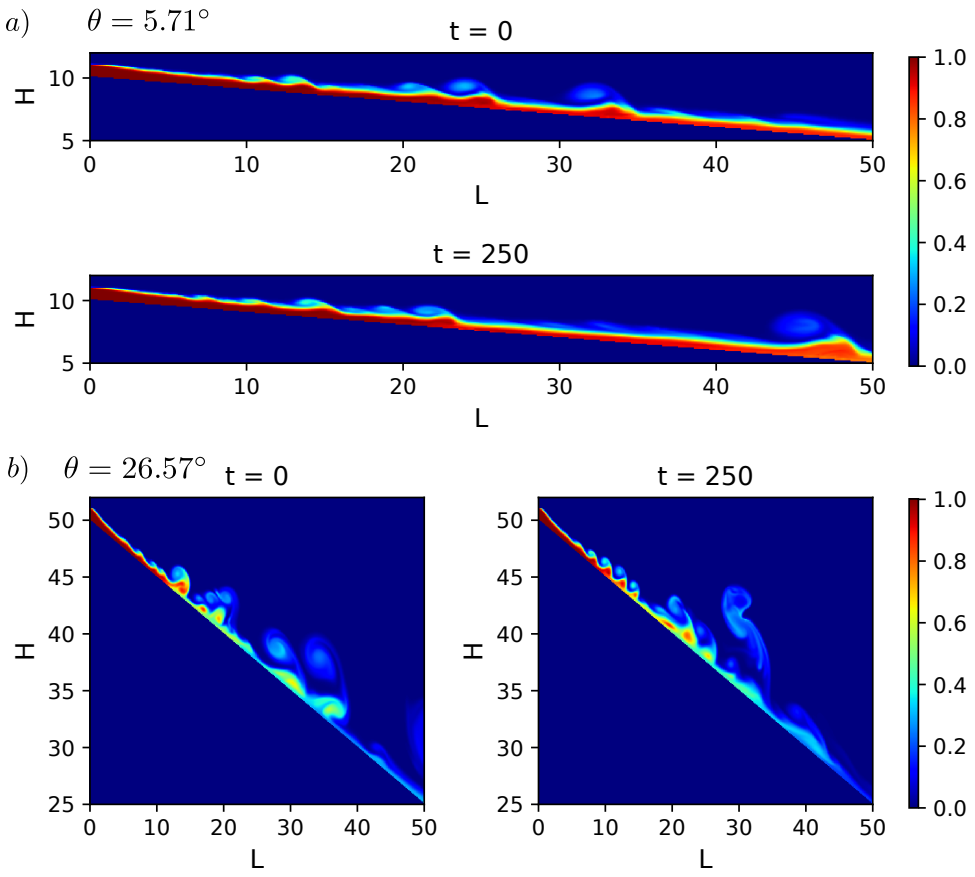

Fig. 4.2 (a) Two snapshots of the concentration field at $t = 0$ and $t = 250$ when $\theta = 5.71°$. (b) Two snapshots of the concentration field at $t = 0$ and $t = 250$ when $\theta = 26.57°$

$t = 250$ can be seen for both experiments in figure 4.2a, b. Comparing the two time snapshots we can see qualitatively that the current has reached a quasi-steady state.

For the low angle case (figure 4.2a) we can see the growth of shear instabilities, with billows which grow in size as the fluid moves downslope. These billows entrain ambient fluid into the current, diluting the buoyancy as they move downstream. However, the billows are relatively small and the density at the base of the current remains relatively close to that of the source fluid, even after the current has travelled 50 times the inflow height. The billows remain coherent, moving as localised non-linear wave-packets downstream, with a small eddy behind the peak of structure, as can be seen at $t = 0$, $L = 12, 25$ and 33. These wave-packets frequently merge, coalesce and

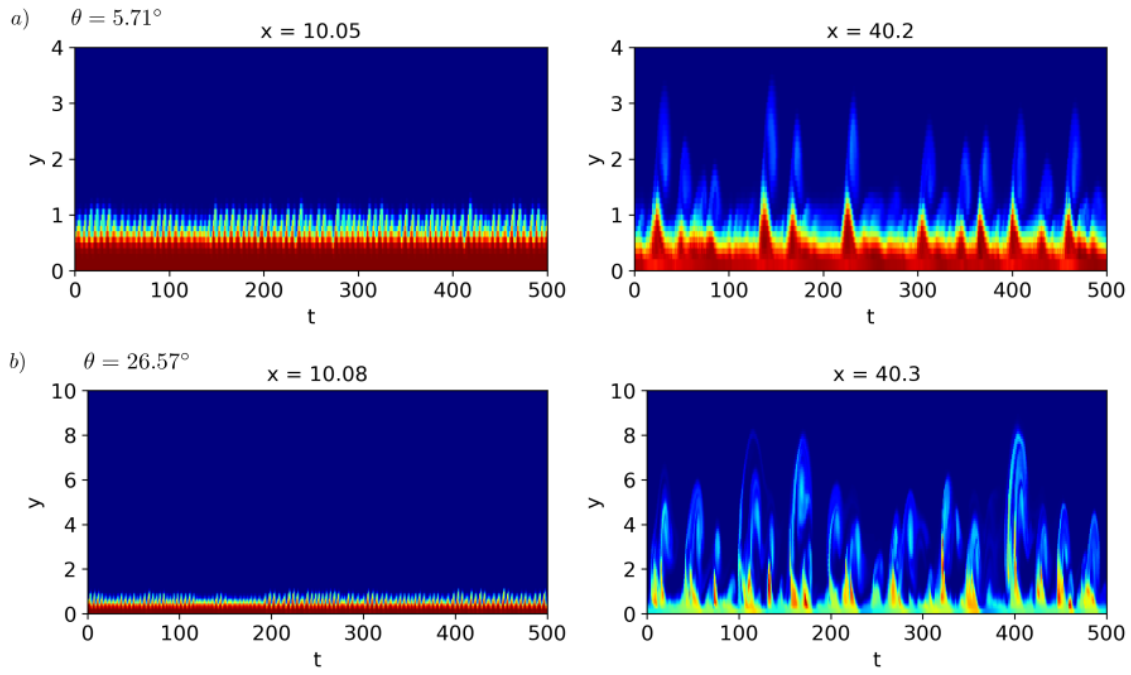

Fig. 4.3 (a) Time series of cross-slope variation in concentration field at $x = 10.05$ and $x = 40.2$ with $\theta = 5.71°$. (b) Time series of cross-slope variation in concentration field at $x = 10.08$ and $x = 40.3$ with $\theta = 26.57°$

interact in a non-linear fashion; however, their coalescence is relatively smooth and parcels of fluid do not appear to detach from the current and mix into the ambient.

That can be contrasted with the high angle case shown in figure 4.2b. Initially the flow is similar to the low angle case, with small shear instabilities appearing in a regular fashion; however, due to the larger component of downslope gravity, these billows quickly evolve into eddies that fill and dilute the entire depth of the current. These eddies interact at a much more frequent rate than the low angle case and with much more intensity. Dense fluid parcels are periodically shed from the current as can be seen at $t = 250$, $L = 31$. Beyond the region downslope a distance $L \approx 15$ from the source the current is no longer coherent but actually forms a series of eddies passing downstream.

We have examined these downslope moving structures by plotting time-series of the concentration field as a function of the cross-slope variation y for a selection of

fixed downslope positions x (figures 4.3a, b). For the low angle case at $x = 10.05$ we can see frequent and regular small eddies pass by in time. Further downslope at $x = 40.2$ we can see that the frequency of these eddies has decreased, but that their size has increased as they coalesce. The regularity of the eddies also decreases as we move downslope. The Fourier transform of the cross-slope average concentration at $x = 10.05$ gives a dominant eddy frequency, in dimensionless units, of $f = 0.30$. Further downstream at $x = 40.2$ the Fourier transform gives a dominant dimensionless frequency $f = 0.065$. The signal at $x = 40.2$ is still clear, although not as striking as for the upslope location.

For the higher angle case of 26.57° eddies pass the point $x = 10.08$ with a frequency $f = 0.40$. Over roughly the same downslope distance from this point, $\Delta x \approx 30$, the eddies have grown about six times in height. At $x = 40.3$ the frequency is dominated by three signals in the range $0.032 \leq f \leq 0.060$, and there is a decrease in frequency as the eddies merge.

For the higher angle calculation, at the downslope location $x \approx 40$, the current has become composed of a series of eddies. In between the eddies the depth of the current is very small when compared with the injection height of 1. In the low angle case, the upper portion of the flow (above $y = 0.5$) is made up of eddies, however the lower half of the current remains as the eddies pass.

An alternative way to view the data is to examine a time-series of the downslope variation along a line of fixed height above the bed. In figure 4.4a, b, we plot these time-series for the low and high angle cases along two different lines at different fixed heights above the slope. At the near-boundary position $y \approx 0.6$ for both angles we can see the intense and frequent production of eddies, denoted by the thin and highly regular lines. We can also see how dense fluid persists for a much larger downslope distance for the low angle case.

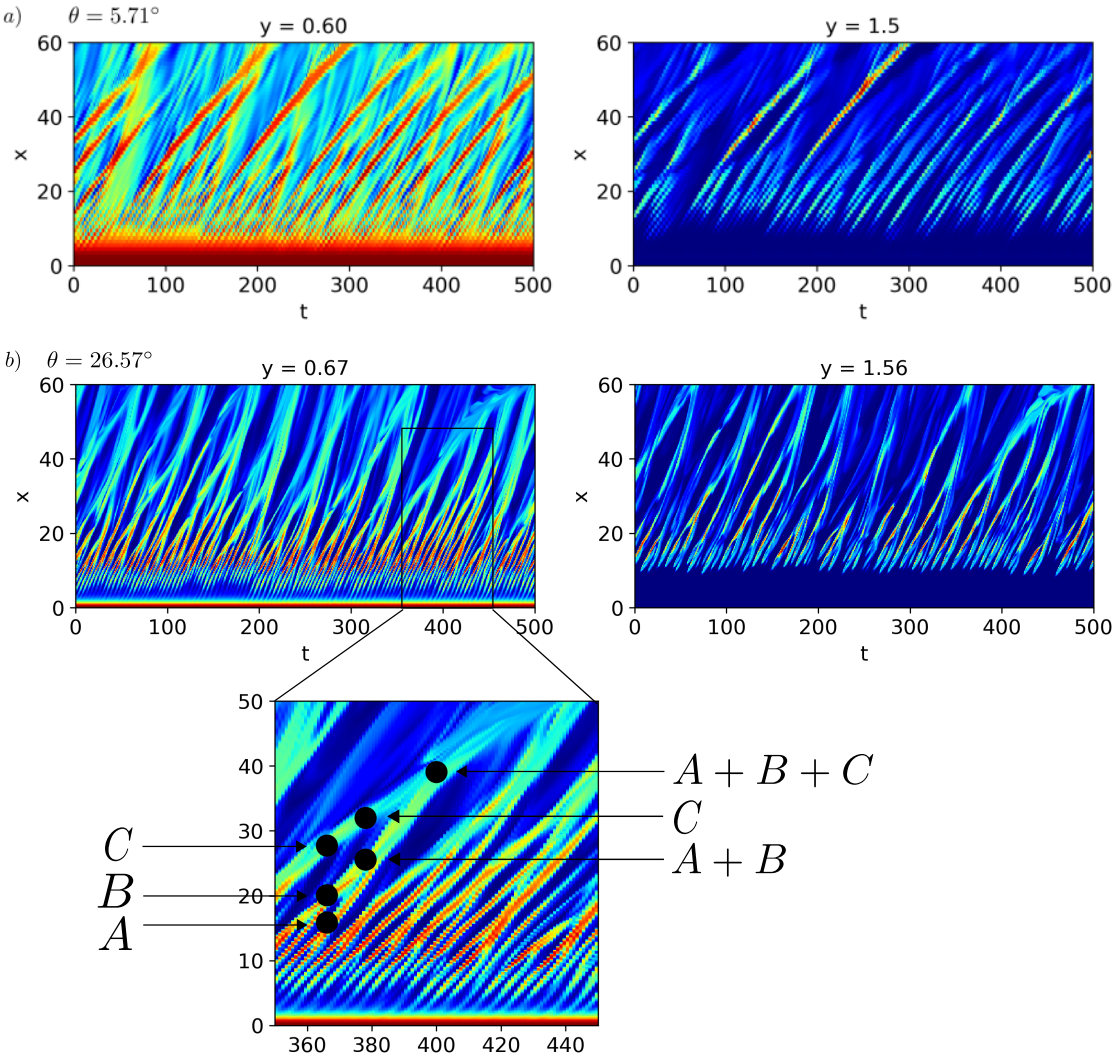

Fig. 4.4 (a) Time series of cross-slope variation in concentration field at $x = 10.05$ and $x = 40.2$ with $\theta = 5.71°$. (b) Time series of cross-slope variation in concentration field at $x = 10.08$ and $x = 40.3$ with $\theta = 26.57°$. The zoomed in portion between $t = 350$ and $t = 450$ on the $\theta = 26.57°$ $y = 0.67$ plot shows the eddies A,B,C at downslope and time locations where the structures tracked in figure 4.5 (panels a, b, c).

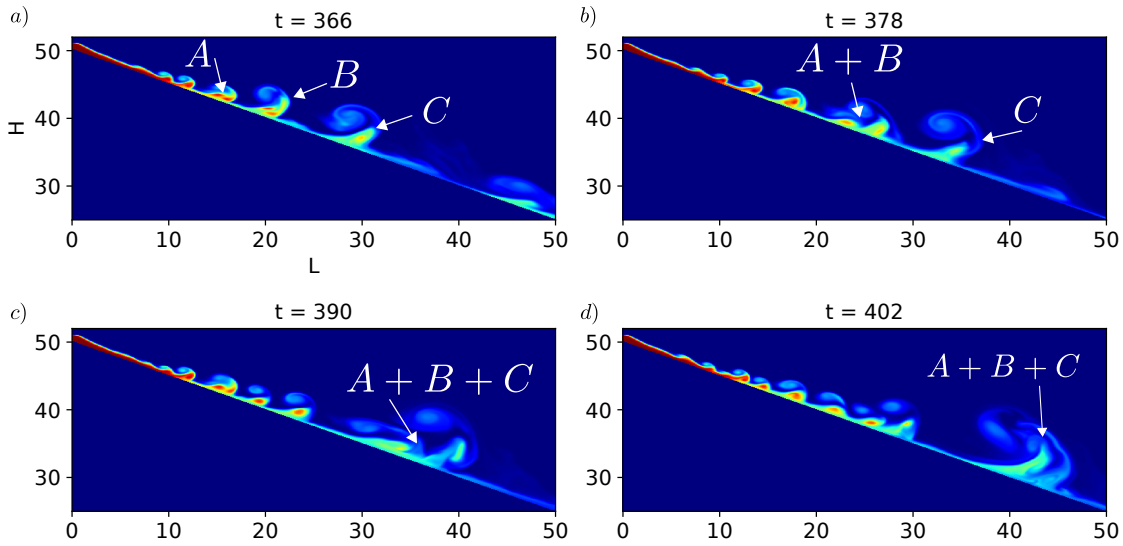

Fig. 4.5 (a) $\theta = 26.57°$ Three eddies A,B and C shown at $t = 366$. (b) The eddies A and B have merged into on on eddy $A + B$ whilst eddy C continues to move downslope at $t = 378$. (c) At $t = 390$ the eddies have merged into one structure $A + B + C$. (d) The eddy $A + B + C$ continues downstream at $t = 402$.

In all plots we see the eddies move downstream. We also see the merging of eddies as two branches collide. To illustrate this merging process and to emphasise how the currents at high angle are composed of a series of coalescing eddies we show this merging process in figure 4.5. In the expanded panel of figure 4.4 we show the three eddies A,B, and C at $t = 366$ and their real space locations are shown in 4.5a. We see that two branches merge at $t = 378$ and we have included two markers to show the merged eddy $A + B$ and the eddy C. This is again seen in real space in 4.5b. Finally we have just one marker left where all the branches have merged at $t = 400$, leaving one eddy structure $A + B + C$. We have shown this in figure 4.5c, d.

In the high angle case the lines which can be seen, and which correspond to the position of individual eddies as a function of time, appear to be approximately linear. This suggests that the eddies are moving downslope at a constant speed. We can take a linear fit to some of these lines to find the velocity of the eddies is approximately 0.51. In the low angle case the lines appear to be curved initially suggesting that

the eddies are decelerating. They appear to have reached a constant speed further downslope in the region between $x = 40$ and 60. By applying the same method of linear interpolation we can find a velocity of approximately 0.28 for low angle case eddies. This illustrates that the angle of inclination has an effect on the eddy speed, as expected.

In the next section we expand on this qualitative description of two experiments and begin quantitative analysis of the data set.

4.5 Experimental Analysis

To make progress when analysing experimental and numerical models of gravity currents it is common to employ a depth-averaged description to simplify the data set and attempt to extract leading order inferences about the underlying physics. In their classic work, Ellison and Turner (1959) outline a method utilising volume flux and momentum flux to obtain depth-averaged quantities describing the velocity and current-height. This method of averaging the volume and momentum flux allows for the definition of an entrainment coefficient E. Ellison and Turner (1959) define the depth-averaged velocity and length scales $\bar{u}$ and $\bar{h}$ respectively as

$$\bar{u}\bar{h} = \int_0^\infty u \, \mathrm{d}y, \quad \bar{u}^2\bar{h} = \int_0^\infty u^2 \, \mathrm{d}y. \tag{4.0a, b}$$

Under the assumption that entrainment is proportional to the depth-averaged velocity, the relation

$$\frac{d(\bar{u}\bar{h})}{dx} = E\bar{u}, \tag{4.1}$$

can be derived. In their paper Ellison and Turner (1959) outline how the integration of the downslope velocity profile u is performed to obtain their measure of $\bar{u}$. The height of the current, i.e. the depth over which they integrate, is taken to be the distance from

the boundary at which the velocity falls to 0. That part of the velocity profile,further from the boundary, which has a negative velocity and arises from the entrainment process (figure 4.1*b*) is not included in their calculation. Similarly, in their paper van Reeuwijk et al. (2017) use an identical depth-averaged definition; however, it is noted that due to the periodic boundary conditions employed in their simulation they have no lateral pressure gradient in the domain, and hence there is only a temporal deepening of the current. This means that they do not have negative values of downslope velocity at any point along the profile.

The data output from the present simulations are a function of downslope and cross-slope positions x, y and time t. The downslope velocity is given by $u_{\text{data}}(x, y, t)$, buoyancy $g'_{\text{data}}(x, y, t)$, local buoyancy flux $B_{\text{data}}(x, y, t) = u_{\text{data}} g'_{\text{data}}$ and local momentum flux $M_{\text{data}}(x, y, t) = u^2_{\text{data}}$. In this section we define the time-averaged downslope quantities

$$u(x, y) = \frac{1}{T} \int_0^T u_{\text{data}}(x, y, t) \, \mathrm{d}t \tag{4.2a}$$

$$g'(x, y) = \frac{1}{T} \int_0^T g'_{\text{data}}(x, y, t) \, \mathrm{d}t, \tag{4.2b}$$

$$B(x, y) = \frac{1}{T} \int_0^T B_{\text{data}}(x, y, t) \, \mathrm{d}t, \tag{4.2c}$$

$$M(x, y) = \frac{1}{T} \int_0^T M_{\text{data}}(x, y, t) \, \mathrm{d}t, \tag{4.2d}$$

where $T = 1000$ is the length of the experiment. The time-averaged currents presented in this chapter deepen as a function of distance downslope. Upon inspection of the time-averaged velocity profiles we observe a negative downslope velocity far above the current due to the entrainment of far-field ambient fluid. As can be seen in figure 4.1*b*, this entrainment occurs due to upper surface of the time-averaged current acting as a pressure sink and drawing in ambient fluid from outside the domain.

Since there are regions in which the time-averaged velocity profile has negative velocity, and in which the buoyancy is different from the ambient, we chose to define the top of the current h^* as the location where the local buoyancy $g'(x,y)$ has fallen below 1% of the buoyancy at the base of the current $g'(x,0)$. So that in our definition, the current represents the region in which the buoyancy is being transported. We have checked the sensitivity of the results to this buoyancy threshold value of 1% and find very similar results with a threshold smaller than 2%. We therefore can define depth-averaged quantities

$$\bar{u}\bar{h} = \int_0^{h^*} u(x,y)\ \mathrm{d}y, \tag{4.3a}$$

$$\bar{u}^2\bar{h} = \int_0^{h^*} M(x,y)\ \mathrm{d}y, \tag{4.3b}$$

$$\bar{u}\bar{g}'\bar{h} = \int_0^{h^*} B(x,y)\ \ \mathrm{d}y \tag{4.3c}$$

Britter and Linden (1980) found that the mean velocity is constant and independent of slope angle. Furthermore, dimensional analysis suggests that the flow depends primarily on the buoyancy flux B and this implies that, in steady state, the speed of the current is a constant and proportional to $B^{1/3}$. It then follows from equation 4.1 that the entrainment coefficient is given by

$$E = \frac{d\bar{h}}{dx}. \tag{4.4}$$

Using the definitions in equations 4.3 and integrating the time-averaged data set u, g' and B, we can calculate $\bar{u}(x)$ and $\bar{h}(x)$. In figure 4.6 we show the calculated values for $\bar{u}$ and $\bar{h}$ as a function of downslope distance x for both the low angle and high angle

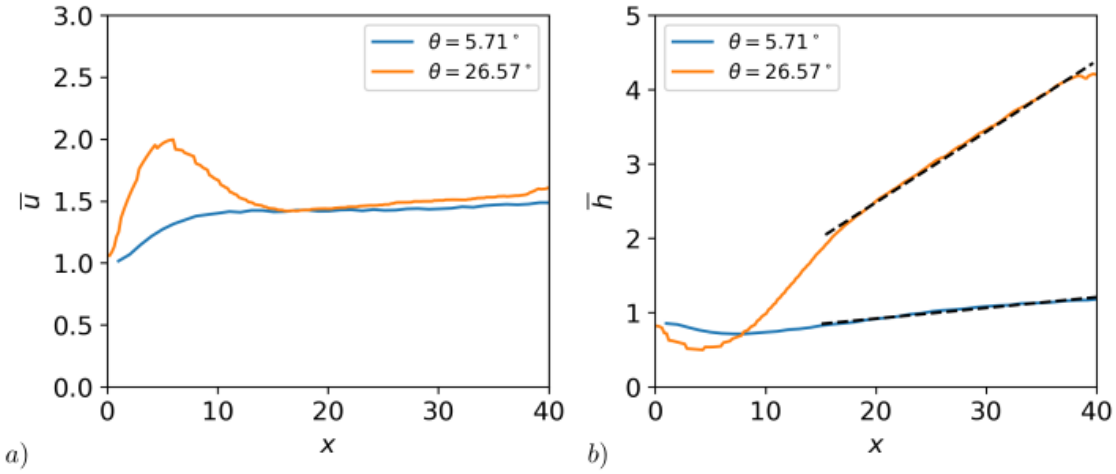

Fig. 4.6 (a) Variation of $\bar{u}$ with downslope distance x for $\theta = 5.71°$ shown in blue and $\theta = 26.57°$ shown in orange. An adjustment period occurs over length $x \approx 15$ after which the values of $\bar{u}$ are approximately constant. (b) Variation of $\bar{h}$ with downslope distance x for $\theta = 5.71°$ shown in blue and $\theta = 26.57°$ shown in orange. After an adjustment length $x \approx 15$ the mean height $\bar{h}$ is shown to grow approximately linearly, with a black dashed lines giving an example of a linear regression on $\bar{h}$, which is used to estimate E.

case. We can see from figure 4.6a that the current adjusts from the inflow over a length $x \approx 15$, after which $\bar{u}$ becomes approximately independent of distance downstream. For $\theta = 5.71°$, in the region where the flow has adjusted ($x \in [15, 40]$), the average $\bar{u} = 1.442 \pm 0.022$, where the error corresponds to the standard deviation, as in the case for all error assessment in this chapter. Similarly for $\theta = 26.57°$, $\bar{u} = 1.490 \pm 0.047$. The variation of $\bar{u}$ across all experimental angles can be found in figure 4.9 with a discussion in §4.5.3.

Moving our attention to figure 4.6b again we can see that after an adjustment period the current depth $\bar{h}$ grows approximately linearly with distance. There are some small non-linear effects, which may be associated with the weak variation of $\bar{u}$; however, with $\theta = 5.71°$, we find that $E = h_x = 0.0147 \pm 0.0024$. When $\theta = 26.57°$ we find $E = h_x = 0.0903 \pm 0.0065$. Figure 4.6$b$ has a dashed black line to illustrate the

fit of the linear regression, from which E is estimated. In figure 4.9*b* we present the dependence of E on the experimental angle.

4.5.1 Self similarity

From figure 4.6 we can see that there is an adjustment period after which the assumptions of $\bar{u}$ constant and $\bar{h}_x$ linear hold to a good approximation. We can illustrate this adjustment period by looking at the buoyancy and downslope velocity profiles. We rescale the cross-slope co-ordinate with the depth-average current height $\bar{h}$ and scale the buoyancy with the averaged value $\bar{g}'$, this leads to an apparent collapse of the profiles to a universal curve (figure 4.7). The grey profiles correspond to the points in the region $x \in [15, 40]$ and each profile is displayed with a reduced opacity, such that when they overlap a darker shade of grey is produced. Two coloured profiles are shown from two further upstream locations, where the current is still transitioning to self-similar state, to illustrate how the adjustment from uniform inflow occurs. It can be seen that in the region $x \in [15, 40]$ the profiles overlap suggesting the profiles are self-similar to a good approximation. In both cases the velocity profiles have two distinct regions. A boundary layer exists near the wall, in which the velocity increases from zero to a clear maximum. An upper region also exists, in which the velocity falls from the maximum value, with near-linear drop off, to the small ambient background value. The buoyancy profiles also have two distinct regions - both approximately linear. A more concentrated region close to the wall and a more dilute upper region. Both regions are roughly separated at the point of the velocity maximum.

4.5.2 Turbulent fluctuations

In equation 4.2 we calculated time-averages of the both the total local buoyancy flux $B_{\text{data}}(x, y, t)$ and total local momentum flux $M_{\text{data}}(x, y, t)$. However, we can decompose

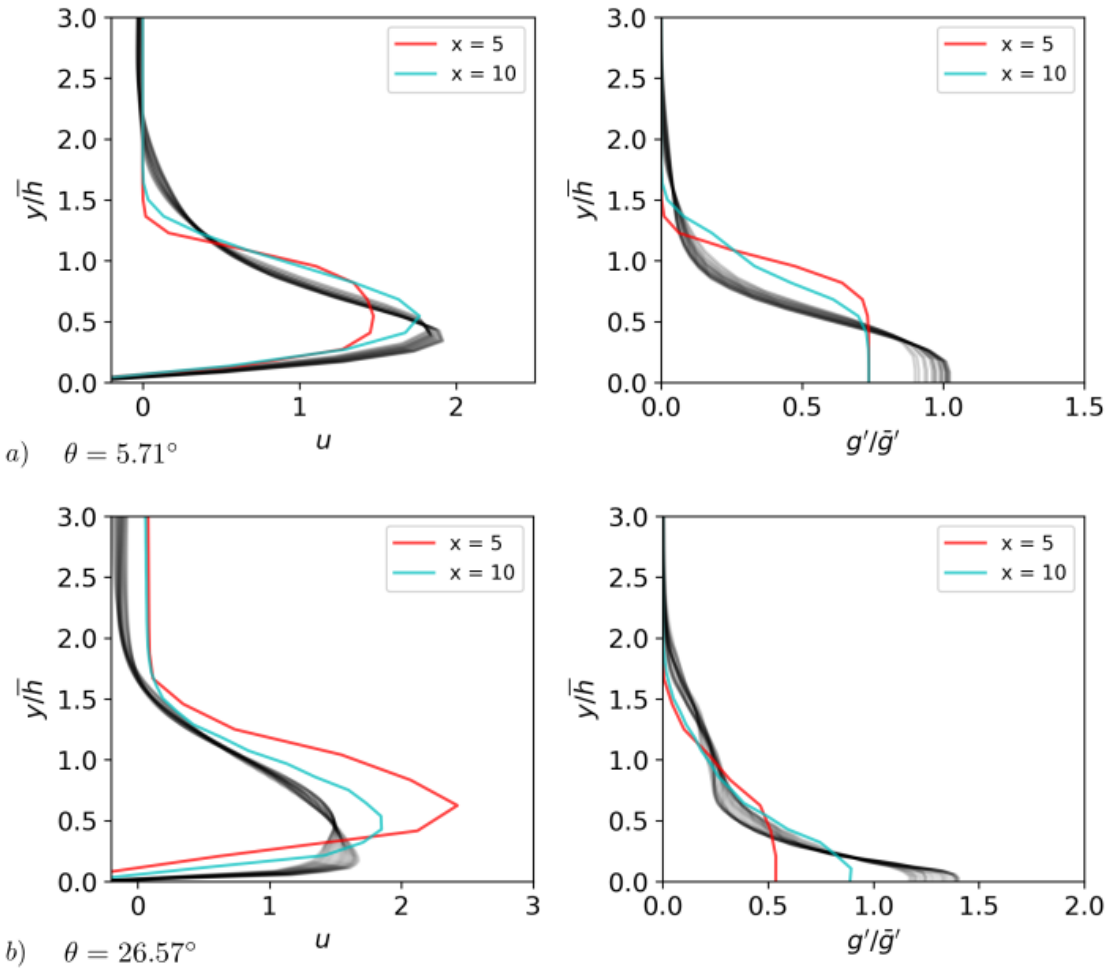

Fig. 4.7 (a) Self-similarity for downslope velocity and buoyancy profiles with $\theta = 5.71°$. The profiles are taken from $x \in [15, 40]$. (b) Variation of $\bar{h}$ with downslope disitance x for $\theta = 5.71°$ shown in blue and $\theta = 26.57°$ shown in orange.

the downslope velocity u_{data} and buoyancy g'_{data} into time-averaged and fluctuating components to gain insight into the nature of the partitioning between the mean and turbulent components of the flow. We can define

$$u_{\text{data}}(x,y,t) = \langle u(x,y)\rangle + \hat{u}(x,y,t) \quad g'_{\text{data}}(x,y,t) = \langle g'(x,y)\rangle + \hat{g}'(x,y,t). \quad (4.4a, b)$$

The time-averaged local buoyancy flux $B(x,y)$ and momentum flux $M(x,y)$ are then given by

$$B = \frac{1}{T}\int_0^T (\langle u\rangle + \hat{u})(\langle g'\rangle + \hat{g}')\ \mathrm{d}t = \langle B\rangle + \hat{B}, \quad (4.5a)$$

$$M = \frac{1}{T}\int_0^T (\langle u\rangle + \hat{u})^2\ \mathrm{d}t = \langle M\rangle + \hat{M}, \quad (4.5b)$$

where $\langle B\rangle, \langle M\rangle$ are the contribution from the mean and $\hat{B}, \hat{M}$ are the time-averaged contribution from the turbulent fluctuations. We can now find the depth-average of B and M to find the partitioning of depth-averaged buoyancy and momentum flux between the mean and time-dependent contributions. We define these depth-averages as

$$\overline{B} = \int_0^\infty \langle B\rangle + \hat{B}\ \mathrm{d}y = \overline{\langle B\rangle} + \overline{\hat{B}}, \quad (4.6a)$$

$$\overline{M} = \int_0^\infty \langle M\rangle + \hat{M}\ \mathrm{d}y = \overline{\langle M\rangle} + \overline{\hat{M}}. \quad (4.6b)$$

In figure 4.8 we plot the partitioning of the time-averaged and depth-averaged buoyancy and momentum fluxes for both the low and high angle cases. The total time-averaged buoyancy flux $\overline{B}$ is conserved in both cases, with $\overline{B} = 0.817\pm0.004$ and $\overline{B} = 0.773\pm0.012$ for the low and high angle cases respectively. The small deviation during the early upstream adjustment is due to a small buoyancy flux in the cross-slope direction not

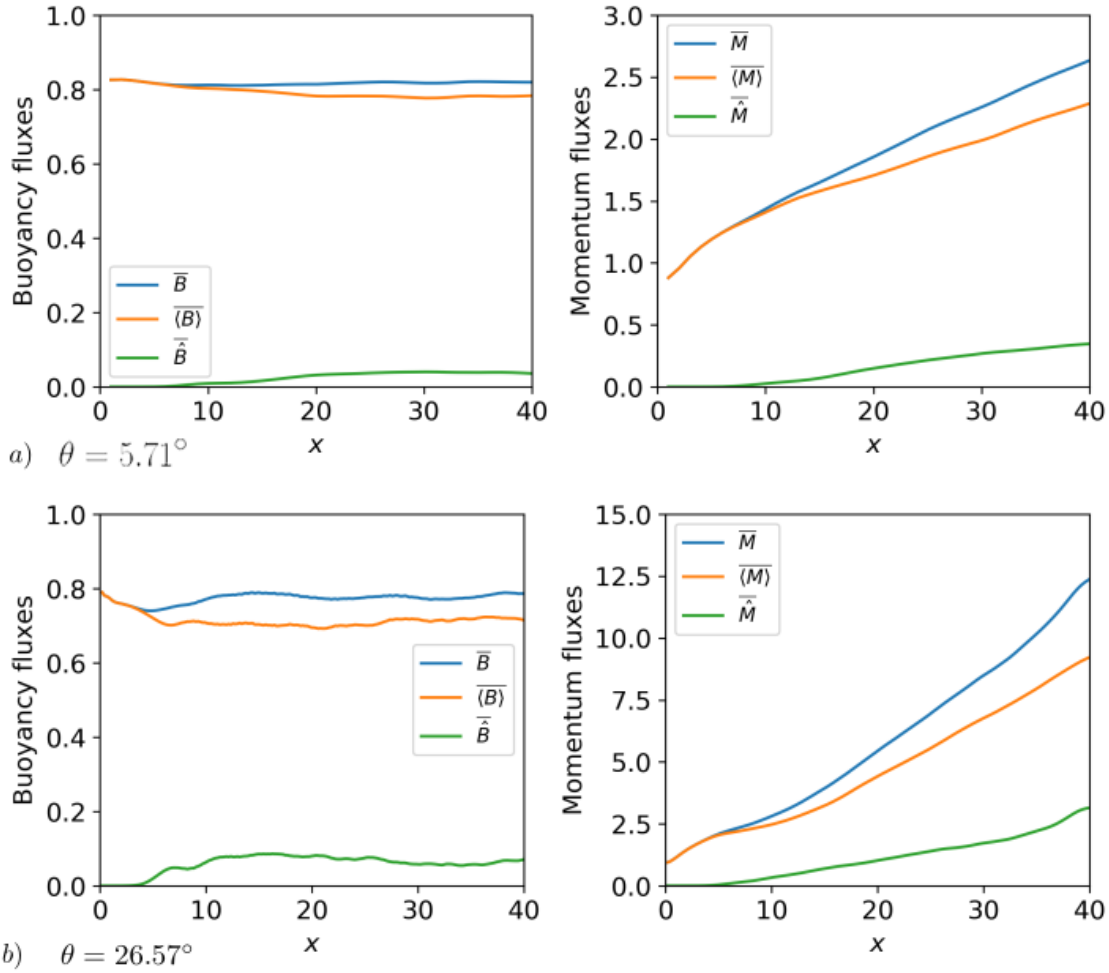

Fig. 4.8 (a) The variation of time-averaged buoyancy $\overline{B}$ and momentum $\overline{M}$ flux in blue for $\theta = 5.71°$. The orange line shows the proportion that comes from the mean flow and the green line shows the proportion that comes from the time-dependent fluctuations.(b) With $\theta = 26.57°$.

captured by the downslope velocity used here. Initially the partition of buoyancy flux carried by the mean and turbulent contributions is equivalent; however, as the current adjusts towards a self-similar state, the turbulent contributions grow until they reach a constant proportion of total time-averaged flux. It is interesting to note that the adjustment takes a larger downslope distance $x \approx 20$ before the turbulent flucatuations become constant in the low angle case; however, in the higher angle case they adjust within a distance of about $x \approx 12$. The average proportion of the buoyancy flux associated with the time-dependent turbulent fluctuations is $\overline{\hat{B}}/\overline{B} = 0.0427 \pm 0.0027$ and $\overline{\hat{B}}/\overline{B} = 0.0889 \pm 0.0071$ in the low and high angle cases respectively.

The partitioning of the momentum flux follows a similar process. Initially the momentum flux associated with the mean equals the total flux; however, as the current adjusts to steady state, the turbulent contributions grow in size. Once the current has adjusted to its self-similar state, both the mean and turbulent contributions grow approximately linearly, owing to the constant release of potential energy as the current flows downslope. The proportion of the momentum flux carried by the turbulent fluctuations given by $\overline{\hat{M}}/\overline{M}$ is roughly constant in the adjusted region. For the low angle case we find that $\overline{\hat{M}}/\overline{M} = 0.114 \pm 0.015$ and for the high angle case $\overline{\hat{M}}/\overline{M} = 0.20 \pm 0.018$. The dependency of the partitioning on the inclination angle is given in figure 4.9c, d in §4.5.3.

4.5.3 Summary statistics

The analysis presented so far has concerned two cases: a low angle at $\theta = 5.71°$ and high angle $\theta = 26.57°$. Experiments were performed at a range of angles to analyse the dependence of depth-averaged quantities on the angle of the inclined boundary. Each quantity presented in this section is derived from the self-similar region for a particular angle. We note that the adjustment length was around $x \approx 15$ for each experiment

and that this is a function of the source buoyancy B_0 and momentum M_0 fluxes (ie. an effective inflow Froude number).

Plotting the calculated values of $\bar{u}$ with θ in figure 4.9*a*, we can see that the mean velocity is approximately constant and independent of angle. This is consistent with the findings of Britter and Linden (1980). We overlay the data with a black dashed line at the average value $\bar{u} = 1.452 \pm 0.038$. Figure 4.9*b* plots the entrainment coefficient E as a function of the associated angle. This shows an approximately linear increase of entrainment with angle. The black dashed line is a linear regression of the data equal to $E = 0.0036\theta - 0.006$ with root mean squared error 0.0044. A linear relationship is consistent with Ellison and Turner (1959). We note that our entrainment values are larger than the data presented by Ellison and Turner (1959) by roughly a factor of two. We believe this variation is due to the two-dimensional nature of the simulations presented here, and also the method by which Ellison and Turner (1959) define the depth-averaged quantities, and especially the region with negative downslope velocity. It would be of interest to run full 3D simulations in the future.

Figures 4.9*c, d* present the proportional of the buoyancy and momentum flux associated with the time-dependent turbulent fluctuations. We see an increase in the proportion associated with the turbulent fluctuations as the angle increases, which is consistent with our observations that the turbulence increases with the inclination angle. It is is interesting to note that as the angle increases the proportion seems to saturate. We have also calculated the gradient Richardson number, which provides a comparison of the stabilising effect of density gradient relative to the destabilising effect of the shear. We define the gradient Richardson number with our depth-averaged quantities as

$$Ri = \frac{\bar{g}\bar{h}}{\bar{u}^2}, \tag{4.7}$$

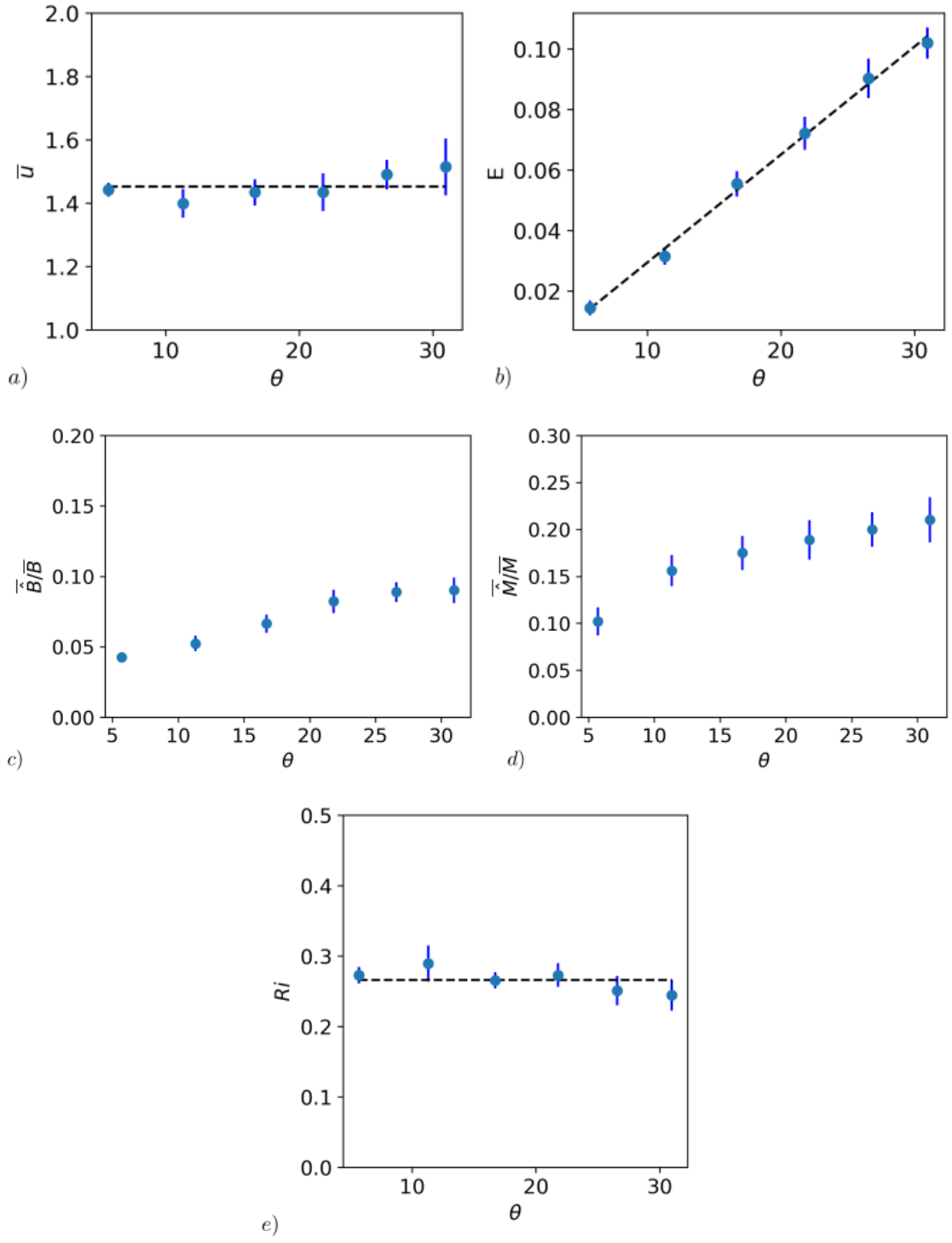

Fig. 4.9 (a) The blue dots show the values of $\bar{u}$ with angle θ.The error bars are the standard deviation. The black dashed line is the average of the data $\bar{u} = 1.452 \pm 0.038$. ($b$) The dots show the entrainment coefficient E data with angle. The black dashed line is a linear regression to the data $E = 0.0035\theta - 0.006$. (c) The proportion of time-dependent contributions to the buoyancy flux transport with angle. (d) The proportion of time-dependent contributions to the momentum flux transport with angle. (e) The variation of gradient Richardson number with angle. The black dashed line illustrates the mean value of the data $Ri = 0.266$.

which is similar to the definition used by Turner (1979) in the limit of small θ. Classical linear stability theory suggests that the critical gradient Richardson number at which currents are linearly stable to all perturbations is 1/4 (Turner, 1979). Once the currents have adjusted such that $\bar{u}$ is constant, $\bar{h} \sim x$ and $\bar{g} \sim 1/x$, we find that Ri is approximately constant with distance and has value which a very close to 1/4. Figure 4.9 shows the calculated value of Ri with angle, which have a mean value $Ri = 0.266 \pm 0.015$. This value for Ri is consistent with the view that once adjusted inclined gravity currents become marginally stable (Turner, 1979).

4.6 Boundary drag

Analytical progress can be made in the description of the flow evolution by making use of a force balance. If we consider a steady two-dimensional current flowing down an inclined slope θ, and assume the pressure normal to the slope is hydrostatic, then the conservation of downslope momentum flux is given by

$$\frac{\partial}{\partial x}\left(\int_0^{h^*} u(x,y)^2 + \left(\int_y^{h^*} g(x,y^*)' \cos\theta \, \mathrm{d}y^*\right) \, \mathrm{d}y\right) = \int_0^{h^*} g'(x,y)\sin\theta - D, \qquad (4.8)$$

where D is the frictional drag force due to the boundary. The cross-slope integrals of buoyancy require shape factors S_1 and S_2 defined as

$$S_1\bar{g}'\bar{h} = \int_0^{h^*} g'(x,y) \, \mathrm{d}y, \quad S_2\bar{g}'\bar{h}^2 = \int_0^{h^*}\int_y^{h^*} g'(x,y^*) \, \mathrm{d}y^* \, \mathrm{d}y. \qquad (4.8a, b)$$

Substituting these definitions into equation 4.8 along with equations 4.3.2 leads to the expression

$$\frac{d}{dx}\left(\bar{u}^2\bar{h} + S_2\bar{g}'\bar{h}^2\cos\theta + T\right) = S_1\bar{g}'\bar{h}\sin\theta - D, \qquad (4.9)$$

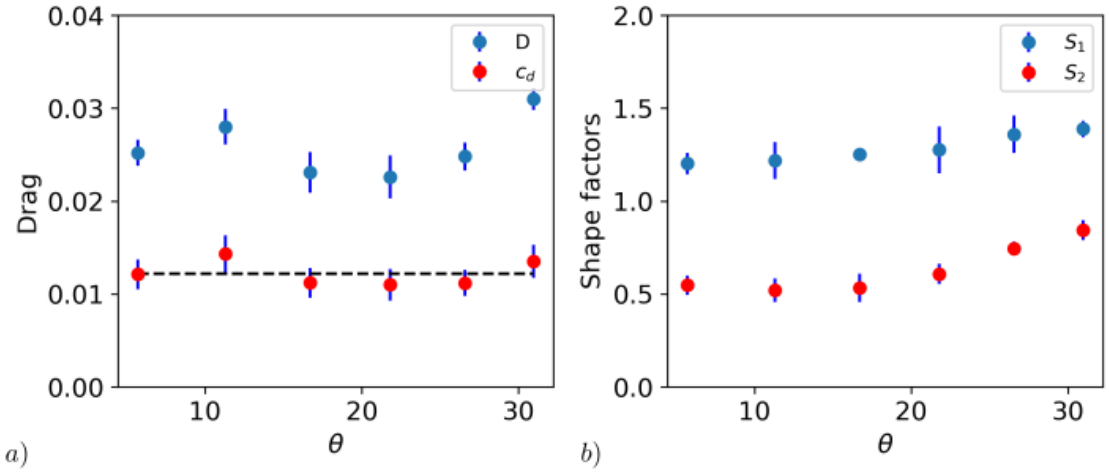

Fig. 4.10 (a) The variation of the drag D and the drag coefficient $c_d = D/\rho\bar{u}^2$ with angle. The black dashed line shows the mean value $c_d = 0.0112$ (b) The variation of shape factors S_1 and S_2 with angle.

where T accounts for the momentum flux transport through the turbulent fluctuations, which have been shown to be around 15% of the total momentum flux. Since all terms inside the differential on the left hand side and the buoyancy production term on the right hand side are known, we can use this equation to find the drag term D. In our calculations we find that the drag force D is a constant as a function of the distance along the slope and that it is primarily dependent on the flow speed u.

In figure 4.10a we show the variation of the drag force with θ. We also show the effective drag coefficient c_d as parametrised by $D/\rho = c_d\bar{u}^2$, with the density $\rho = 1$. We find the drag coefficient is approximately independent of angle. The black dashed line illustrates the mean drag coefficient $c_d = 0.0112 \pm 0.0013$, which applies for all angles. Figure 4.10b illustrates the variation of the shape factors S_1 and S_2 with angle. It is interesting to note that in equation 4.9 the first two terms on the LHS and the first term on the RHS are approximately in balance, with the turbulent transport and the drag being much smaller. Assuming that the three largest terms are in balance, and that Ri is a constant, we can combine equation 4.9 with equation 4.1 to determine

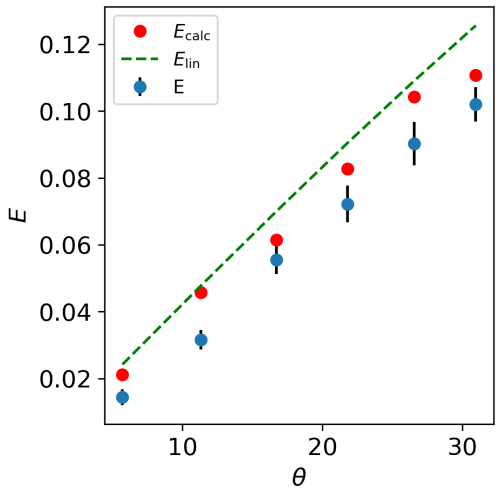

Fig. 4.11 A comparison between E as derived from the numerical data in blue, E_{calc} derived from the time-averaged model with shape factors and E_{lin} derived from the model with idealised linear profiles.

an approximate relation for the entrainment coefficient

$$E = \frac{S_1 Ri \sin\theta}{1 + S_2 Ri \cos\theta}. \tag{4.10}$$

By calculating shape factors S_1, S_2, and the gradient Richardson number Ri associated with the currents at each angle θ, equation 4.10 provides an approximation for the entrainment coefficient $E = E_{\text{calc}}$. In figure 4.11 we compare this calculated value for the entrainment coefficient $E = E_{\text{calc}}$ (red) with the exact value E (blue). Although this approximate model neglects the drag and the turbulent fluctuations in the flow, it is within an error of 5-10% of the directly calculated value of E.

It is also of interest to assess the importance of the detailed variation of velocity and buoyancy with distance across the slope. In particular, we compare the depth average of the numerical profiles with a simplified model in which we assume the velocity and buoyancy vary linearly with position across the slope, motivated by the profiles shown in figure 7 (cf. Horsley and Woods, 2018). If we assume the profiles have idealised form

defined as

$$u(x,y) = \frac{u_0(h-y)}{h}, \quad g'(x,y) = \frac{g'_0(h-y)}{h} \qquad (4.10a, b)$$

then the free parameters u_0, g'_0 and h can be substituted into the governing equations and rewritten in terms of the depth-averaged quantities

$$u_0 = \frac{3\bar{u}}{2}, \quad g'_0 = \frac{3\bar{g}'}{2}, \quad h = \frac{4\bar{h}}{3}. \qquad (4.10a, b, c)$$

In this case, shape factors for these idealised linear profiles are $S_1 = 1$ and $S_2 = 4/9$. If we assume that the idealised linear profile has a critical gradient Richardson number $Ri = 0.25$ we can use equation 4.10 to give a simplified expression for the entrainment coefficient

$$E_{\text{lin}} = \frac{9\sin\theta}{4(9+\cos\theta)}. \qquad (4.11)$$

This is shown as the green dashed line in figure 4.11. This very simple approximate value is within 10-20 % of the actual entrainment coefficient and provides a useful idealised picture for interpreting the evolution of gravity currents along a slope.

4.7 Discussion

In this chapter we have presented new numerical simulations of two-dimensional continuous flux gravity currents moving along an inclined horizontal boundary. Using the data generated by these experiments we have found that after an adjustment period the flow reaches an approximately self-similar state. Time-averaged statistics of this self-similar state suggest that to a good approximation the mean velocity $\bar{u}$ is constant and independent of slope angle consistent with the results of Britter and Linden (1980). Furthermore, the rate of growth of the mean current height $\bar{h}$ is approximately linear. From this we have presented new estimates for the entrainment parameter E

for a two-dimensional gravity current. We have found that the entrainment E is an increasing function of the slope angle and varies between 0.01 - 0.1 for the range of angles presented herein. In these adjusted currents, the Ri has value of about 0.25 suggesting the entrainment acts so that the flow is marginally stable in accord with Turner's original hypothesis.

In the calculations presented herein the Peclet number was set at $Pe = 2000$ and the Reynolds number was fixed at $Re = 10000$, such that we believe the flows are highly turbulent and that the entrainment is not rate limited by molecular processes. Indeed, the flows appear to follow a self-similar evolution along the slope, with a constant entrainment coefficient as the flow moves downstream, which is consistent with the flow being highly turbulent. We therefore believe the results are useful for helping interpret the evolution of such flows. It may be of interest however to explore the behaviour of such flows at much larger and much smaller Peclet number.

We note that there is a considerable literature in which the entrainment coefficient for turbulent gravity currents has been presented as a function of the bulk Richardson number of the flow (Alavian, 1986; Cenedese and Adduce, 2008, 2010). In their figure 2, Cenedese and Adduce (2010) present a collection of data from a wide range of experiments plotting entrainment coefficient as a function of bulk Froude number. However, we have found in our experiments that the gradient Richardson number evolves to a constant value close to 1/4. In each of the experimental studies, one of the key questions concerns the state of the flow, in terms of whether the flow is adjusting to the self-similar state, or is already adjusted at the point where measurements are taken. In order to understand the controls on the adjustment of the current to the normal state from arbitrary inflow conditions, it would be very useful to have further well-constrained experimental or numerical results.

Chapter 5

Discussion

This chapter is split into two sections. §5.1 outlines the conclusions of the work presented in this thesis. In particular, we summarise our main contributions to the body of research at large. In §5.1 we discuss some interesting possible extensions of the work presented herein.

5.1 Conclusions

In this thesis, we have presented three problems relating to buoyancy-driven flow at low and high Reynolds numbers. §2 introduces the novel problem of a finite-release exchange flow in a two-dimensional annular geometry. With the use of a lubrication approximation we make analytical progress from the governing equations of motion to derive a nonlinear PDE, which describes the spatio-temporal evolution of the density interface between the two exchanging fluids. A simple geometrical argument leads to the recognition that there are two distinct regimes: a small volume case where - at equilibrium - the interface between the two fluids does not intersect the inner cylinder; and a large volume case where the interface intersects the inner cylinder and leads to two spatially distinct interfaces (§2.4). We systematically analyse a series of initial

distributions, which are parametrised by i) the initial angle subtended by the arc of the distribution and the centre of the annulus φ_{init} and ii) the initial cement depth h_0. This analysis demonstrates that there exists exchange-flow-like, gravity-current-like and draining regimes, which have analogy with classical works in a rectilinear geometry. A key difference that is found between the classical work and the results presented herein is the finite distance travelled by the current to reach equilibrium. This equilibrium state exists due to the curved lower boundary introducing a varying component of gravitational acceleration in the azimuthal direction. Additional results show that the time to reach this equilibrium state can vary by two orders of magnitude depending on the initial distribution (§2.7). The work is relevant for the problem of cement placement in a well bore. If cement is pumped into the gap between the well and the rock, and preferentially spreads along one part of the annulus, perhaps owing to asymmetry in the location of the well within the hole, then the cement will subsequently spread out relative to that part of the annulus. As a simplified model, the symmetric spreading problem illustrates some of the key controls on the process, and allows us to determine whether the cement will spread out prior to setting. The analysis demonstrates the importance of the initial distribution in such flows when compared to the cement curing time scale. If the flow has not reached an equilibrium state before the cement has begun to cure, it could impact the integrity of the well.

In §3 we introduce a simplified analytical framework for constraining the downstream structure of gravity currents propagating along a rigid horizontal boundary from a uniform source. We constrain the downstream structure by imposing conservation of momentum flux and buoyancy flux throughout the flow. Experimental and numerical data suggests, to a good approximation, that the downstream velocity and buoyancy profiles of such propagating currents may be: i) entirely linearly stratified or ii) have a uniform lower region overlain by a region of constant gradient. With this in mind, we

substitute an idealised ansatz into the governing equations to find analytical solutions for the downstream structure as a function of the source Froude number and a shape factor ϕ. These solutions also lead to the recognition of subcritical and supercritical downstream currents (§3.5.3). We relate these solutions to the downstream gradient Richardson number (to indicate their stability), change in downstream transport (to indicate entrainment), and energy dissipation, to give global constraints on each. We find that there exists a critical source Froude number $Fr_u = 2.921$, after which the current has sufficient momentum flux to entrain the ambient such that it can be wholly modified through mixing and become entirely linearly stratified even if the source conditions are uniform (§3.5). By comparison with experimental data from Kneller et al. (2016) we find our model provides a useful framework for interpreting the adjustment of numerical simulations of gravity currents as they issue from a uniform source.

In §4 we present new numerical data on two-dimensional gravity currents flowing down a rigid inclined boundary from a uniform source of buoyancy and momentum flux. By making use of the TURBINS direct numerical simulation code (Nasr-Azadani and Meiburg, 2011) we present a series of new experiments at high-Reynolds-number $Re = 10000$ and differing angle to the horizontal θ. We find that when the boundary is inclined at a large angle to the horizontal, the current breaks up into a series of eddies, which coalesce and merge as they migrate downstream (§4.4). Furthermore, we find that that after an adjustment length approximately equal to 15 times the initial depth of the flow the downstream velocity and buoyancy profiles become self-similar (§4.5.1). Depth-averaging in an appropriate way allows us to show that the mean downstream velocity $\bar{u}$ is approximately constant and the mean downstream height of the current $\bar{h}$ grows approximately linearly with downslope distance (§4.5). From this linear growth rate we can estimate the entrainment coefficient E. In figure 4.9*b* we present the variation of the entrainment coefficient E with angle, showing

that it varies from between 0.01 and 0.1 for angles θ between 5° and 30°. We find that the Richardson number $Ri = \bar{g}\bar{h}/\bar{u}^2$ of all currents in the self-similar regime is approximately constant at $Ri \approx 0.25$ and independent of slope angle (§4.5.3). This corroborates the explanation by Turner (1979) that currents mix to be marginally stable as they propagate downstream. Furthermore, by appropriate time-averaging of the simulation data we estimate the buoyancy and momentum flux carried by the time-dependent turbulent fluctuations to be around 10% and 15% respectively (§4.5.2). Making use of the conservation of momentum we estimate that the coefficient of drag experienced by such gravity currents is constant and independent of slope angle with $c_d \approx 0.01$ (§4.6).

5.2 Further work

This section is split into two subsections. §5.2.1 discusses possible extensions of the low-Reynolds-number work presented in §2. §5.2.2 discusses possible extensions of the high-Reynolds-number work presented in §§3-4.

5.2.1 Low-Reynolds-number

The work presented on low-Reynolds-number flow in §2 explores the evolution of a density interface between two miscible fluids in an annular geometry. The work is presented in two dimensions, which leads to interesting results for the particular class of flows discussed; however, it would be of interest to extend this model into the third dimension. The application of this work was modelling the displacement of one fluid by another in a horizontal well-bore. Allowing for flow in the axial direction would enhance our understanding of the role cement injection rates play, in addition to that of their initial distribution. Since the well may be hundreds to thousands of metres in

length, variations in the axial distribution of the fluid may be important in regulating the exchange flow, and it may be that density-driven fingering instabilities develop in the exchange flow owing to the azimuthal component of the buoyancy force.

Also, for the work presented in §2 the inner and outer cylinders of the annulus were assumed to be concentric, and symmetry was assumed throughout. In practice it is known that as the bore is drilled eccentricity develops between the casing and the rock. Eccentricity introduces an asymmetry into the problem which would have an important effect on the flow dynamics. This would be of interest to explore.

It was also assumed that the surface tension between the fluids and any viscosity differences were small. In recent work Grenfell-Shaw and Woods (2017) have demonstrated the importance of both Saffman-Taylor (viscosity-driven) and Rayleigh-Taylor (buoyancy-driven) instabilities on the displacement of fluids in a sloping narrow channel. Related work by Beeson-Jones and Woods (2017) discusses the importance of injection rate on controlling the development of Saffman-Taylor instabilities. It would be of interest to extend the analysis presented in §2 and relax the assumptions made on stratification, surface tension, and viscosity differences, to understand the role of density, capillary, and viscous instabilities on the general class of flows presented.

5.2.2 High-Reynolds-number

The work presented on high-Reynolds-number flows in §§3-4 focused on the entrainment and mixing of horizontal and inclined currents. Again the work for both chapters is presented in two-dimensions. In particular, it would be interesting to extend the numerical simulations presented in §4 to full three-dimensional simulations. Whilst two-dimensional simulations are important for informing the understanding of quasi-two-dimensional flows (eg. an avalanche down a narrow mountain couloir), many flows in the environment and industry are fully three-dimensional. It is well known that the

energy cascade in two-dimensional turbulent flow is the inverse of three-dimensional flow (Kraichnan, 1967). This inverse energy cascade causes kinetic energy to move from smaller to larger length scales, which will have an effect on the growth of eddies. Since we have demonstrated currents flowing down an inclined boundary evolve into a series of coalescing eddies, it would be of interest to see how extension into the third dimension will affect this. In particular, quantifying the effect on the estimated entrainment rate E.

It would also be of interest to extend §4 by solving for a secondary passive concentration field. This tracer would then given insight into the role of shear dispersion inside such gravity currents. Data would help inform the modelling of passive tracers, such as the evolution and spread of radioactive matter after an industrial accident.

One of the key findings in §4 was the existence of an adjustment period from the uniform inflow conditions to self-similarity. Running a series of experiments with varying initial momentum and buoyancy flux conditions would help constrain the dependence of this adjustment length on the source conditions. Knowledge of this length scale dependence could then be compared with the simplified analysis of §3 to estimate an entrainment coefficient for adjusting horizontal currents.

Finally it would be of interest to include topography in both the theoretical analysis of §3 and the simulations in §4. In particular, a smoothly varying lower boundary could be used to determine the role of hydraulic control on the entrainment and mixing formulations of §3.

References

Acheson, D. J. (1990). *Elementary fluid dynamics*. Oxford University Press.

Acton, J. M., Huppert, H. E., and Worster, M. G. (2001). Two-dimensional viscous gravity currents flowing over a deep porous medium. *Journal of fluid mechanics*, 440:359–380.

Alavian, V. (1986). Behavior of density currents on an incline. *Journal of hydraulic engineering*, 112(1):27–42.

Balmforth, N., Burbidge, A., and Craster, R. (2001). Shallow lava theory. In *Geomorphological fluid mechanics*, pages 164–187. Springer.

Beeson-Jones, T. H. and Woods, A. W. (2017). Control of viscous instability by variation of injection rate in a fluid with time-dependent rheology. *Journal of Fluid Mechanics*, 829:214–235.

Benjamin, T. B. (1968). Gravity currents and related phenomena. *Journal of Fluid Mechanics*, 31(2):209–248.

Bonnecaze, R. T., Huppert, H. E., and Lister, J. R. (1993). Particle-driven gravity currents. *Journal of Fluid Mechanics*, 250:339–369.

Britter, R. and Linden, P. (1980). The motion of the front of a gravity current travelling down an incline. *Journal of Fluid Mechanics*, 99(3):531–543.

Britter, R. and Simpson, J. (1978). Experiments on the dynamics of a gravity current head. *Journal of Fluid Mechanics*, 88(2):223–240.

Bursik, M. I. and Woods, A. W. (1996). The dynamics and thermodynamics of large ash flows. *Bulletin of Volcanology*, 58(2):175–193.

Cenedese, C. and Adduce, C. (2008). Mixing in a density-driven current flowing down a slope in a rotating fluid. *Journal of Fluid Mechanics*, 604:369–388.

Cenedese, C. and Adduce, C. (2010). A new parameterization for entrainment in overflows. *Journal of Physical Oceanography*, 40(8):1835–1850.

Cenedese, C., Nokes, R., and Hyatt, J. (2016). Mixing in a density-driven current flowing over a rough bottom.

Clarke, R. (1961). Mesostructure of dry cold fronts over featureless terrain. *Journal of Meteorology*, 18(6):715–735.

References

Clarke, R. (1972). The morning glory: an atmospheric hydraulic jump. *Journal of Applied Meteorology*, 11(2):304–311.

Curtiss, C. and Hirschfelder, J. O. (1952). Integration of stiff equations. *Proceedings of the National Academy of Sciences of the United States of America*, 38(3):235.

Eduardo, S., Dutra, S., and Monica, F. (2004). Liquid displacement during oil well cementing operations. *Annual Transactions of the Nordic Rheology Society*, 1:93–100.

Ellison, T. and Turner, J. (1959). Turbulent entrainment in stratified flows. *Journal of Fluid Mechanics*, 6(03):423–448.

Fay, J. (1980). Gravitational spread and dilution of heavy vapor clouds. In *Second International Symposium on Stratified Flows, the Norwegian Institute of Technology, Trondheim, Norway*, pages 24–27.

Gardner, G. and Crow, I. (1970). The motion of large bubbles in horizontal channels. *Journal of Fluid Mechanics*, 43(2):247–255.

Garvine, R. W. and Monk, J. D. (1974). Frontal structure of a river plume. *Journal of Geophysical Research*, 79(15):2251–2259.

Gratton, J. and Vigo, C. (1994). Self-similar gravity currents with variable inflow revisited: plane currents. *Journal of Fluid Mechanics*, 258:77–104.

Grenfell-Shaw, J. C. and Woods, A. W. (2017). The instability of a moving interface in a narrow tapering channel of finite length. *Journal of Fluid Mechanics*, 831:252–270.

Hacker, J., Linden, P., and Dalziel, S. (1996). Mixing in lock-release gravity currents. *Dynamics of Atmospheres and Oceans*, 24(1-4):183–195.

Hallworth, M. A., Phillips, J. C., Huppert, H. E., and Sparks, R. S. J. (1993). Entrainment in turbulent gravity currents. *Nature*, 362(6423):829–831.

Hogg, A. and Matson, G. (2009). Slumps of viscoplastic fluids on slopes. *Journal of Non-Newtonian Fluid Mechanics*, 158(1-3):101–112.

Hogg, A. J., Nasr-Azadani, M. M., Ungarish, M., and Meiburg, E. (2016). Sustained gravity currents in a channel. *Journal of Fluid Mechanics*, 798:853–888.

Holland, D. M., Rosales, R. R., Stefanica, D., and Tabak, E. G. (2002). Internal hydraulic jumps and mixing in two-layer flows. *Journal of Fluid Mechanics*, 470:63–83.

Horsley, M. C. and Woods, A. W. (2018). A note on analytic solutions for entraining stratified gravity currents. *Journal of Fluid Mechanics*, 836:260–276.

Hoult, D. P. (1972). Oil spreading on the sea. *Annual Review of Fluid Mechanics*, 4(1):341–368.

Howard, L. N. (1961). Note on a paper of John W. Miles. *Journal of Fluid Mechanics*, 10(04):509–512.

Huppert, H. E. (1982a). Flow and instability of a viscous current down a slope. *Nature*, 300(5891):427.

Huppert, H. E. (1982b). The propagation of two-dimensional and axisymmetric viscous gravity currents over a rigid horizontal surface. *Journal of Fluid Mechanics*, 121:43–58.

Huppert, H. E. and Simpson, J. E. (1980). The slumping of gravity currents. *Journal of Fluid Mechanics*, 99(4):785–799.

Huppert, H. E. and Woods, A. W. (1995). Gravity-driven flows in porous layers. *Journal of Fluid Mechanics*, 292:55–69.

Ivey, G., Winters, K., and Koseff, J. (2008). Density stratification, turbulence, but how much mixing? *Annu. Rev. Fluid Mech.*, 40:169–184.

Johnson, C. G. and Hogg, A. J. (2013). Entraining gravity currents. *Journal of Fluid Mechanics*, 731:477–508.

Kneller, B. M., Nasr-Azadani, M. M., Radhakrishnan, S., and Meiburg, E. (2016). Long-range sediment transport in the world's oceans by stably stratified turbidity currents. *Journal of Geophysical Research: Oceans*, 121:8608–8620.

Kraichnan, R. H. (1967). Inertial ranges in two-dimensional turbulence. *The Physics of Fluids*, 10(7):1417–1423.

Kudaikulova, G. (2015). Rheology of drilling muds. In *Journal of Physics: Conference Series*, volume 602, page 012008. IOP Publishing.

Kuenen, P. H. (1950). Turbidity currents of high density. In *18th International Geological Congress (1948), London, Reports, pt*, volume 8, pages 44–52.

Liapidevskii, V. Y. (1994). Mixing and blocking effects in two-layer flow over an obstacle. In *Proc. 4th Int. Symp. on Stratified Flows*, volume 4, pages 183–189.

Lister, J. R. (1992). Viscous flows down an inclined plane from point and line sources. *Journal of Fluid Mechanics*, 242:631–653.

Longo, S., Chiapponi, L., and Di Federico, V. (2016). On the propagation of viscous gravity currents of non-newtonian fluids in channels with varying cross section and inclination. *Journal of Non-Newtonian Fluid Mechanics*, 235:95–108.

Lyle, S., Huppert, H. E., Hallworth, M., Bickle, M., and Chadwick, A. (2005). Axisymmetric gravity currents in a porous medium. *Journal of Fluid Mechanics*, 543:293–302.

Matson, G. P. and Hogg, A. J. (2012). Viscous exchange flows. *Physics of Fluids*, 24(2):023102.

Miles, J. W. (1961). On the stability of heterogeneous shear flows. *Journal of Fluid Mechanics*, 10(04):496–508.

Monti, P., Querzoli, G., Cenedese, A., and Piccinini, S. (2007). Mixing properties of a stably stratified parallel shear layer. *Physics of Fluids*, 19(8):085104.

Morton, B., Taylor, G., and Turner, J. (1956). Turbulent gravitational convection from maintained and instantaneous sources. *Proc. R. Soc. Lond. A*, 234(1196):1–23.

Myers, T. G. (1998). Thin films with high surface tension. *Siam Review*, 40(3):441–462.

Nasr-Azadani, M. M. and Meiburg, E. (2011). Turbins: an immersed boundary, navier–stokes code for the simulation of gravity and turbidity currents interacting with complex topographies. *Computers & Fluids*, 45(1):14–28.

Odier, P., Chen, J., and Ecke, R. E. (2014). Entrainment and mixing in a laboratory model of oceanic overflow. *Journal of Fluid Mechanics*, 746:498–535.

Ottolenghi, L., Adduce, C., Inghilesi, R., Armenio, V., and Roman, F. (2016). Entrainment and mixing in unsteady gravity currents. *Journal of Hydraulic Research*, 54(5):541–557.

Prandtl, L. (1953). Essentials of fluid dynamics: with applications to hydraulics, aeronautics, meteorology and other subjets.

Princevac, M., Fernando, H., and Whiteman, C. D. (2005). Turbulent entrainment into natural gravity-driven flows. *Journal of Fluid Mechanics*, 533:259–268.

Pritchard, D., Woods, A. W., and Hogg, A. J. (2001). On the slow draining of a gravity current moving through a layered permeable medium. *Journal of Fluid Mechanics*, 444:23–47.

Samasiri, P. and Woods, A. W. (2015). Mixing in axisymmetric gravity currents. *Journal of Fluid Mechanics*, 782:R1.

Sauer, C. et al. (1987). Mud displacement during cementing: "a state of the art". *Journal of Petroleum Technology*, 39(09):1–091.

Schiesser, W. E. (2012). *The numerical method of lines: integration of partial differential equations*. Elsevier.

Shahriar, A. (2011). *Investigation on rheology of oil well cement slurries*. PhD thesis, The University of Western Ontario.

Sher, D. and Woods, A. W. (2015). Gravity currents: entrainment, stratification and self-similarity. *Journal of Fluid Mechanics*, 784:130–162.

Sher, D. and Woods, A. W. (2017). Mixing in continuous gravity currents. *Journal of Fluid Mechanics*, 818.

Siddiqi, Z. A. (2012). *Concrete Structures Part-II*, volume 2. Zahid Ahmad Siddiqi.

Simpson, J. E. (1982). Gravity currents in the laboratory, atmosphere, and ocean. *Annual Review of Fluid Mechanics*, 14(1):213–234.

Simpson, J. E. (1997). *Gravity currents: In the environment and the laboratory*. Cambridge university press.

Smyth, W. D. and Moum, J. N. (2012). Ocean mixing by kelvin-helmholtz instability.

Spannuth, M. J., Neufeld, J. A., Wettlaufer, J., and Worster, M. G. (2009). Axisymmetric viscous gravity currents flowing over a porous medium. *Journal of Fluid Mechanics*, 622:135–144.

Strang, E. and Fernando, H. (2001). Entrainment and mixing in stratified shear flows. *Journal of Fluid Mechanics*, 428:349–386.

Takagi, D. and Huppert, H. E. (2007). The effect of confining boundaries on viscous gravity currents. *Journal of Fluid Mechanics*, 577:495–505.

Turner, J. (1986). Turbulent entrainment: the development of the entrainment assumption, and its application to geophysical flows. *Journal of Fluid Mechanics*, 173:431–471.

Turner, J. S. (1979). *Buoyancy effects in fluids*. Cambridge University Press.

van Reeuwijk, M., Krug, D., and Holzner, M. (2017). Small-scale entrainment in inclined gravity currents. *Environmental Fluid Mechanics*, pages 1–15.

van Reeuwijk, M., Krug, D., and Holzner, M. (2018). Small-scale entrainment in inclined gravity currents. *Environmental Fluid Mechanics*, 18(1):225–239.

Vella, D. and Huppert, H. E. (2006). Gravity currents in a porous medium at an inclined plane. *Journal of Fluid Mechanics*, 555:353–362.

von Kármán, T. (1940). The engineer grapples with nonlinear problems. *Bulletin of the American Mathematical Society*, 46(8):615–683.

Xu, X., Chang, Y. S., Peters, H., Özgökmen, T. M., and Chassignet, E. P. (2006). Parameterization of gravity current entrainment for ocean circulation models using a high-order 3d nonhydrostatic spectral element model. *Ocean Modelling*, 14(1):19–44.

Zheng, Z., Rongy, L., and Stone, H. A. (2015). Viscous fluid injection into a confined channel. *Physics of fluids*, 27(6):062105.